AN ABSTRACT OF THE THESIS OF

Robert P. Dziak for the degree of Doctor of Philosophy in Geology presented on June 2, 1997. Title: Acoustic Monitoring of Earthquakes Along the Blanco Transform Fault Zone and Gorda Plate and Their Tectonic Implications.

Abstract approved: _____

Robert S. Yeats

Hydroacoustic tertiary (T-) waves are seismically generated acoustic waves that propagate over great distances in the ocean sound channel with little loss in signal strength. Hydrophone recorded T-waves can provide a lower earthquake detection threshold and an improved epicenter location accuracy for oceanic earthquakes than land-based seismic networks. Thus detection and location of NE Pacific ocean earthquakes along the Blanco Transform Fault (BTFZ) and Gorda plate using the U.S. Navy's SOSUS (SOund SUrveillance System) hydrophone arrays afford greater insight into the current state of stress and crustal deformation mechanics than previously available. Acoustic earthquake information combined with bathymetry, submersible observations, earthquake source-parameter estimates, petrologic samples, and water-column chemistry renders a new tectonic view of the southern Juan de Fuca plate boundaries.

Chapter 2 discusses development of seismo-acoustic analysis techniques using the well-documented April 1992 Cape Mendocino earthquake sequence. Findings include a hydrophone detection threshold estimate (M ~ 2.4), and T-wave propagation path modeling to approximate earthquake acoustic source energy. Empirical analyses indicate that acoustic energy provides a reasonable magnitude and seismic moment estimate of oceanic earthquakes not detected by seismic networks. Chapters 3 documents a probable

volcanogenic T-wave event swarm along a pull-apart basin within the western BTFZ during January 1994. Response efforts yielded evidence of anomalous water-column $^{3}He$ concentrations, pillow-lava volcanism, and the first discovery of active hydrothermal vents along an oceanic fracture zone. Chapter 4 discusses the detection of a NE-SW trending microearthquake band along the mid-Gorda plate which was active from initiation of SOSUS recording in August 1991 through July 1992, then abruptly ceased. It is proposed that eventual termination of the Gorda plate seismicity band is due to strain reduction associated with the Cape Mendocino earthquake sequence. Chapter 5 combines bathymetric, hydro-acoustic, seismic, submersible, and gravity data to investigate the active tectonics of the transform parallel Blanco Ridge (BR), along the eastern BTFZ. The BR formation mechanism preferred here is uplift through strike-slip motion (with a normal component) followed by formation and intrusion of mantle-derived serpentinized-peridotite into the shallow ocean crust. The conclusion considers a potential link between the deformation patterns observed along the BTFZ and Gorda plate regions.

# Acoustic Monitoring of Earthquakes Along the Blanco Transform Fault Zone and Gorda Plate and Their Tectonic Implications

by

Robert P. Dziak

A THESIS

submitted to

Oregon State University

in partial fulfillment of
the requirements for the
degree of

Doctor of Philosophy

Completed June 2, 1997
Commencement June 1998

Doctor of Philosophy thesis of Robert P. Dziak presented on June 2, 1997

APPROVED:

Major Professor, Representing Geology

Chair of Department of Geosciences

Dean of Graduate School

I understand that my thesis will become part of the permanent collection of Oregon State University libraries. My signature below authorizes release of my thesis to any reader upon request.

Redacted for privacy

Robert P. Dziak

ACKNOWLEDGMENTS

I owe a great debt of gratitude to my supervisors Chris Fox and Steve Hammond, of the NOAA/PMEL Ocean Environment Research Division for their support and sponsorship of this research. Also, I am very grateful to my major professor Bob Yeats for his guidance through the OSU graduate school jungle and his constant reminder to adhere to the highest scientific standards. And I want to thank my committee members Bob Embley, Chris Goldfinger, Dawn Wright, John Nabelek, and John Tappeiner for their support and efforts to improve my thesis. I promise all of you that you will not have to sit through another discussion of how T-waves are formed! Also I want to thank my colleagues and friends at the Marine Science Center in Newport for their support and for putting up with me and my grumpy ways during my graduate school experience.

My dissertation is dedicated to a few special people in my life who have always supported me and my desire to obtain a Ph.D. (and specialize myself out of a lot of job opportunities!). To my parents, Paul and Mary Jane Dziak, who gave me the desire to work hard and always give my best effort. To my sister, Paula Dziak-Steinker, who bought me my first science fiction novel when I was 12 years old and got me hooked on the wonders of science. Paula has been an inspiration throughout my life to keep a strong desire to learn more. To Chris Fox who gave me my first research job, supported my work while being fair-minded critic, and presented me with an opportunity to pursue a Ph.D. as part of my work responsibilities. Thank you Chris, and I promise to uphold our arrangement to someday give an employee of mine the same opportunity that you gave me. Last and most importantly, to my wife Julie whose selfless love and support has always given me the strength to finish what I start in both my professional and personal

life. Julie, you worked so hard to help me finish this thesis that you deserve to be called Dr. and not me!

"Science isn't perfect, but its the best we've got" from *Demon Haunted World* by Carl Sagan

"Ages are not dark because the light doesn't shine, but because people refuse to see it" from *2010* by Arthur C. Clarke

[By the year 1976 we'll have] "Just Machines to make big decisions, programmed by fellas with compassion and vision" from *IGY - Night Fly* by Donald Fagan

Scientific inquiry can provide a safer, more fulfilling world for all of us, but it is up to the scientists to address societal concerns with a more humanitarian than de-humanizing approach. Perhaps then we can eliminate society's mistrust of science and technology.

# CONTRIBUTION OF AUTHORS

## Chapter 2

Robert Dziak selected, located, and estimated source level of Cape Mendocino earthquakes, performed acoustic propagation modeling, regression analyses, data reduction, and wrote paper. Dr. Christopher Fox provided access to hydrophone earthquake data and assisted in acoustic data interpretation. Dr. Haru Matsumoto assisted with acoustic propagation modeling. Dr. Anthony Schreiner assisted with seismic wave velocity modeling and seafloor displacement estimates.

## Chapter 3

Robert Dziak located and interpreted earthquakes and volcanic tremor, performed seafloor geologic mapping and interpretation, and wrote paper. Dr. Christopher Fox provided access to earthquake data, and assisted in interpretation of volcanic activity. Dr. Robert Embley provided access to seafloor mapping technology, discovered hydrothermal vents, established volcanic nature of basin, and helped interpret seafloor geology. Dr. John Lupton and Dr. Greg Johnson provided water column data and interpretation. Dr. William Chadwick provided seafloor morphology information and counted some tremor events. Dr. Randolf Koski also helped provide access to seafloor mapping technology and time on the research vessel.

## Chapter 4

Dr. Christopher Fox identified T-wave seismicity band and edited paper. Robert Dziak selected earthquakes, performed data analysis and structure interpretation of seismicity band, and wrote paper. Dr. Chris Goldfinger provided seismic reflection and Gloria sidescan data, and assisted with structural interpretation of seismicity.

## Chapter 5

Robert Dziak provided T-wave locations of earthquakes, geologic interpretation from submersible video and bathymetry, seismic reflection data and interpretation, gravity and magnetics data and interpretation, calculation and interpretation of slip vector and stress axis information, integrated data to produce tectonic model, and wrote paper. Dr. Christopher Fox provided access to earthquake data, while Dr. Robert Embley provided access to seafloor mapping technology, and helped interpret seafloor geology. Dr. John Nabelek and Jochen Braunmiller provided earthquake source parameter information which was the basis for the stress and slip vector analysis. Dr. Randolf Koski provided thin section descriptions of rock samples.

TABLE OF CONTENTS

TABLE OF CONTENTS (Continued)

TABLE OF CONTENTS (Continued)

LIST OF FIGURES

LIST OF FIGURES (Continued)

LIST OF FIGURES (Continued)

LIST OF FIGURES (Continued)

LIST OF TABLES

# Acoustic Monitoring of Earthquakes Along the Blanco Transform Fault Zone and Gorda Plate and Their Tectonic Implications

## Chapter 1

## Introduction

### 1.1 Introduction

Over the past decade, the National Oceanic and Atmospheric Administration's VENTS Program has focused on quantitatively measuring the distribution and volume of emissions from northeast Pacific spreading centers (Hammond et al., 1991). Several lines of evidence gathered from *in situ* monitors indicated that the Juan de Fuca Ridge (JdFR) had been volcanically active in the last decade. However it was found that to monitor tectonic and volcanic activity in progress along the JdFR requires continuous long-range surveillance. The JdFR has long been viewed as aseismic, although in practice this lack of seismicity implies nothing more than a paucity of earthquakes exceeding the detection threshold of regional and teleseismic land-based networks, generally of bodywave magnitude > 4. Seismicity associated with volcanic systems like mid-ocean ridges tend to occur at magnitudes below this threshold (Klein et al., 1987; Einarsson, 1991).

Because of the need to monitor JdFR seismicity in real-time, access to an existing network of NE Pacific deep-ocean SOFAR (SOund Fixing And Ranging) channel SOSUS (SOund SUrveillance System) hydrophones operated by the U.S Navy was requested and became available to the VENTS Program in December of 1990. The goal of this effort was to enable detection of small magnitude earthquakes using their Tertiary (T-) waves. T-waves are seismically generated acoustic waves that propagate over great distances in the oceanic sound channel with little loss in signal strength (Tolstoy and Ewing, 1950), even at

relatively high (> 1 Hz) seismic frequencies (Northrop et al., 1960). As is discussed in this study, utilization of the oceanic sound channel allows for detection of small ($m_b$ < 4) earthquakes over regional distances, with an estimated detection threshold of the SOSUS system in the NE Pacific of $m_b \approx 2.4$. Locating earthquakes using their T-waves allows for highly accurate (±3 km error in latitude and longitude) event locations because 1) the ocean sound speed can be directly measured and adjusted for seasonal variation and 2) the hydrophone array configuration is much improved over that of land-based seismic networks. Earthquakes are located using an iterative non-linear regression algorithm that minimizes the error between the travel time observed on the hydrophones and the predicted travel time estimated by incrementing a given event's latitude, longitude, and origin time.

On August 29, 1991 the laboratory in Newport began receiving continuously recorded digital hydrophone data from throughout the NE Pacific (Fox et al., 1994). On June 22, 1993 NOAA installed a prototype system at the U.S. Naval Facility, Whidbey Island to allow real-time acoustic monitoring of the NE Pacific (Fig. 1). This effort was rewarded with the first-ever detection of a deep-ocean volcanic eruption (Fox et al, 1995). Nearly 700 T-wave earthquakes and volcanic tremor associated with a magmatic-dike injection along the CoAxial Segment (Juan de Fuca Ridge) were located using this system (Dziak et al., 1995; Schreiner et al., 1995). The high-precision earthquake locations were used to direct rapid response efforts to the seafloor eruption site where fresh lava flows and thermo-chemical water column anomalies were found (Embley et al. 1995; Baker et al., 1995). Thus this system can be used to monitor seismicity of other active faults offshore of Washington, Oregon, and northern California that would normally be below the detection threshold of land-based seismic networks, and also to provide more accurate locations of large events whose fault plane orientation is known.

## 1.2 Statement of Purpose

The purpose of this study is to use the recently available data from U.S. Navy's SOSUS hydrophone arrays to detect and locate earthquakes along the Blanco Transform Fault Zone (BTFZ) and Gorda plate for insight into the current state of stress, and mechanics of crustal deformation in these regions. Hydrophones monitoring the ocean's sound channel provide a lower detection threshold and improved location capabilities for offshore earthquakes, thus previously unknown patterns of seismic strain release within and along the southern Juan de Fuca and Gorda plates may be identified. This study discusses the development of these acoustic earthquake detection and location techniques, and is the first thorough use of these techniques to understand the recent tectonics of submarine plate boundaries. The advantages of using the SOSUS hydrophone arrays to do regional monitoring and tectonic studies of oceanic earthquakes exist in the system's continuous recording capability, the ability to derive highly accurate locations for oceanic earthquakes compared to west coast regional seismic networks, and the relative cost efficiency of the hydrophone data relative to Ocean Bottom Seismometer data.

Acoustic earthquake information combined with high-resolution bathymetry, camera-tow and submersible observations, earthquake source-parameter estimates, petrologic samples, and water-column chemistry should provide an improved view of the recent tectonics along the southern Juan de Fuca and Gorda plates. Chapter 2 discusses the development of many of these seismo-acoustic analysis techniques using the well documented April 1992 Cape Mendocino earthquake sequence. Chapters 3,4, and 5 discuss the volcano-tectonic processes along the BTFZ and Gorda plate observed by integrating the various acoustic, seismic, geologic, and water column data sets. A final goal of this thesis, reviewed in the conclusion, is to consider a potential link between the volcano-tectonic deformational patterns observed along the BTFZ and those on the Gorda plate regions.

# Chapter 2

## The April 1992 Cape Mendocino Earthquake Sequence: Seismo-acoustic Analysis Utilizing Fixed Hydrophone Arrays

Robert P. Dziak

*Department of Geosciences*
*Oregon State University*
*Corvallis, OR*

Christopher G. Fox*

Haruoshi Matsumoto

Anthony E. Schreiner

*Cooperative Institute for Marine Resources Studies*
**National Oceanic and Atmospheric Administration*
*Pacific Marine Environmental Laboratories*
*Oregon State University Hatfield Marine Science Center*
*Newport, OR 97365, U.S.A.*

*Marine Geophysical Researches*
Kluwer Academic Publishers, Dordrecht, The Netherlands
May 1997, 25 pages, in press

## 2.1 Abstract

The oceanic T-waves of earthquakes associated with the 1992 Cape Mendocino earthquake sequence were recorded and analyzed using fixed hydrophone arrays located throughout the northeast Pacific ocean. The T-waves of these events were well recorded with high S/N ratios and strong acoustic energy present over a 0-64 Hz bandwidth. The smallest event recorded by the hydrophone arrays from the sequence had a local magnitude of 2.4. The hydrophone records of the three largest shocks in the sequence ($M_L$ 6.9,6.2,6.5) exhibited both T-waves and lithospheric phases from these events. Low-pass filtering (2 Hz) of the lithospheric phases yielded a clear P-wave arrival for epicentral distances of < 10°, but no apparent S-wave. A seafloor cable-break was detected immediately after the second M > 6 aftershock, possibly the result of a submarine slide. The direct P-wave hydrophone records from the second large aftershock showed a relatively high-amplitude, high-frequency arrival, consistent with seismic analyses which used this information to infer rupture direction. The rupture direction was toward the location of the cable break, thus rupture directivity possibly played a role in initiating the slide. Modelling of the T-wave propagation path, using the Parabolic Equation model, produced estimates of the acoustic transmission loss from epicenter to receiver. The transmission loss to the most distant phones is typically 10-20 dB, and can be as large as 50-70 dB for acoustic propagation paths that cross the continental margin. The amount of acoustic energy each earthquake released into the ocean at the seafloor-water interface was estimated applying the transmission loss and instrument response to the recorded T-wave signals. This acoustic source power level was calculated for 41 events with magnitudes over a recorded range of $2.4 < M_L < 6.9$, with 17 of these events having their seismic moment estimates available through the NEIC. Ground displacement spectra were estimated from the acoustic power spectra and showed no indication of a corner frequency. Thus empirical analyses relating

source level to magnitude and seismic moment were necessary to derive quantitatively an earthquake's size from hydrophone records. The results of indicator variable regression analyses suggest that T-wave source level increases linearly with the event's local magnitude and seismic moment. Furthermore, the source power level versus magnitude relationships for oceanic and continental earthquakes are significantly different, probably illustrating differences in the seismic and acoustic propagation paths from hypocenter to the hydrophone receivers. The results indicate that acoustic measurements provide a reasonable estimate of magnitude and seismic moment of an oceanic earthquake that was not detected by land-based seismic networks.

## 2.2 Introduction

Tertiary (T-) waves are seismically generated acoustic waves that propagate over great distances in the oceanic sound channel with little loss in signal strength (Tolstoy and Ewing, 1950), even at relatively high (> 1 Hz) seismic frequencies (Northrop et al., 1960). Several mechanisms have been presented for the excitation of T-waves. The most widely accepted method for T-wave generation from continental-margin earthquakes involves multiple reflection between the sea surface and the sloping clastic wedge (Tolstoy and Ewing, 1950; Wadati and Inouye, 1953; Johnson et al., 1963). Prior studies have used the duration of the T-wave packet to infer the earthquake rupture duration (Ben-Menahem and Toksoz, 1963; Gupta, 1964; Johnson 1970), estimate a b-value for T-wave events (Brocher, 1983), and develop an empirical relation to seismic moment (Okal and Talandier, 1986). Other analyses have empirically related the peak amplitude of the T-wave to earthquake magnitude (Johnson and Northrop, 1966; Gibowicz et al., 1974), and the mean T-wave spectral amplitude (in dB) to seismic moment (Walker et al., 1992; Hiyoshi et al., 1992). In these previous studies, ocean-acoustic analyses were not used to estimate the strength of the

T-wave earthquake at the source. Deconvolution of the T-wave hydrophone record by instrument gain and transmission loss along the sound channel propagation path can be used to estimate the acoustic energy level of the earthquake at the seafloor-ocean interface.

Since August 1991, the National Oceanic and Atmospheric Administration (NOAA) VENTS Program has been continuously recording acoustic signals from the U.S. Navy's Sound Surveillance System (SOSUS) located in the NE Pacific Ocean. These efforts have resulted in the location of nearly two orders of magnitude more seismic events in the northeast Pacific than were detected by land-based seismic networks during the same time interval (Fox et al., 1994). The number of recorded T-wave events led to an indirect estimate of the detection threshold for the northeast Pacific of magnitude 2.4, a 1.5 magnitude improvement over the detection threshold of the global seismic network (E. Bergman, U.S.G.S., pers comm.), and regional seismic networks (S. Malone, U. of Washington, pers. comm.). Unfortunately, the precise array locations are not for public distribution, however earthquake locations, hydrophone time-series, spectra, and non-time stamped sonograms can be openly discussed. Locations estimated for NE Pacific ocean earthquakes using the SOSUS arrays have smaller error and locate closer to active plate boundaries than those available from land-based seismic networks due to good azimuthal control of the array geometry and directly measured ocean sound velocities (Fox et al, 1994).

The impetus for this research was to evaluate the detection/analysis capabilities of the SOSUS hydrophone arrays using a well-documented seismic sequence. Toward this goal, we analyzed the hydrophone records of 41 coastal northern California earthquakes that occurred during, before, and after the April 1992 Cape Mendocino Sequence (Table 2.1and Figure 2.1). These earthquakes provide an outstanding opportunity to evaluate the earthquake detection and analysis capability of the Navy hydrophone arrays because the

sequence was well recorded by land-based regional and teleseismic networks, and exhibited a wide range of magnitudes ($1.0 < M_L < 6.9$). Figures 2.2, 2.3, and 2.4 show the time series and corresponding sonograms (0 - 64 Hz) of the mainshock ($M_L$ = 6.9) and two large aftershocks ($M_L$ = 6.2 and 6.5) from each of the SOSUS hydrophone arrays that recorded the events. More complete descriptions of the hydrophone system and its capabilities are given in Fox et al. (1994) and Fox et al. (1995).The term T-wave used here describes seismically generated acoustic energy received at the hydrophone arrays via a propagation path that is almost entirely in the water. The original term T-phase coined by Linehan (1940) was used to describe the third (or tertiary) large seismic phase that followed the primary (P) and secondary (S) phases. Thus T-phase denotes the third seismic phase recorded by land-based instruments in which part of the propagation path from source to receiver is oceanic. T-wave describes the arriving wave's method of propagation rather than its arrival order on a hydrophone record. Furthermore, preference is given to the more general term "wave" to describe the arrival energy rather than "phase", since the latter implies that the received energy is limited to a particular frequency.

## 2.3 Cape Mendocino Sequence

### *2.3.1 Tectonic Setting*

The Cascadia subduction zone (CSZ), offshore northern California, Oregon, and Washington, accommodates approximately 3-4 cm/yr (Riddihough, 1984) of east-northeast oblique convergence between the North American and Juan de Fuca plates (Figure 2.1). The southern section of the Juan de Fuca plate, south of the Blanco Fracture Zone, is commonly referred to as the Gorda plate because during the past 2-3 Ma it has been

experiencing deformation independent of the rigid Juan de Fuca plate (Wilson, 1989). North-south compressive stresses are present within the Gorda plate west of the Cascadia subduction zone, probably due to either northward motion of the Pacific plate and the resistance to this motion by the locked megathrust, or by a mismatch between the spreading direction of the Gorda Ridge and orientation of the Mendocino transform (Silver, 1971; Stoddard, 1987). The young, easily deformed Gorda plate responds to this stress by failing along northeast-southwest trending left-lateral strike-slip faults (Wilson, 1989). This intraplate seismicity accounts for a major portion of the recent seismic activity in this region, although strong earthquakes have occurred recently within the subduction zone (1991 $M_L$=6.2 Honeydew Earthquake) and paleoseismic evidence suggests great (M > 8) earthquakes have been generated by the subduction zone in the recent prehistoric past (Dengler et al., 1992).

*2.3.2 Seismicity*

On April 25 and 26, 1992, three earthquakes with local magnitudes of 6.9, 6.2, and 6.5 occurred near Cape Mendocino, California. The sequence began with the relatively shallow (depth = 10 km) magnitude 6.9 earthquake on April 25 at 18:06Z. The two most powerful aftershocks ($M_L$ 6.2 and 6.5) occurred the next day at 07:41Z and 11:18Z, respectively, 20 km west of the mainshock and offshore within the continental margin. These two large aftershocks had hypocenters approximately 20 km deep. During the next month, roughly 300 well-located aftershocks ($M_L$ > 2) were recorded by the National Earthquake Information Center and the University of California, Berkeley Seismographic Station.

**TABLE 2.1**: 1992 Cape Mendocino Events used in this Analysis[1]

| Event | Date (MODYYR) | Origin Time (H:M:S) | Latitude (°N) | Longitude (°W) | h (km) | $M_L$ | $M_o$ (N-m) |
|---|---|---|---|---|---|---|---|
| 1 | 03/08/92 | 03:43:04.4 | 40.228 | 124.290 | 13 | 5.3 | $1.9 \times 10^{17}$ |
| 2 | 04/25/92 | 18:06:04.2 | 40.368 | 124.316 | 15 | 6.9 | $6.7 \times 10^{19}$ |
| 3 | 04/26/92 | 00:02:08.4 | 40.331 | 124.475 | 15 | 2.8 | |
| 4 | 04/26/92 | 00:28:28.8 | 40.422 | 124.395 | 05 | 3.1 | |
| 5 | 04/26/92 | 00:40:26.1 | 40.302 | 124.386 | 02 | 3.8 | |
| 6 | 04/26/92 | 00:49:17.5 | 40.357 | 124.437 | 01 | 3.6 | |
| 7 | 04/26/92 | 00:54:10.9 | 40.408 | 124.344 | 06 | 3.0 | |
| 8 | 04/26/92 | 01:00:57.9 | 40.362 | 124.508 | 05 | 4.2 | |
| 9 | 04/26/92 | 01:27:14.5 | 40.307 | 124.473 | 04 | 3.6 | |
| 10 | 04/26/92 | 02:08:09.4 | 40.299 | 124.403 | 15 | 3.5 | |
| 11 | 04/26/92 | 02:17:53.0 | 40.324 | 124.462 | 03 | 3.6 | |
| 12 | 04/26/92 | 04:19:58.1 | 40.538 | 124.689 | 12 | 3.2 | |
| 13 | 04/26/92 | 07:41:39.7 | 40.415 | 124.603 | 20 | 6.2 | $6.0 \times 10^{18}$ |
| 14 | 04/26/92 | 08:19:13.5 | 40.322 | 124.476 | 11 | 3.1 | |
| 15 | 04/26/92 | 08:21:09.4 | 40.383 | 124.561 | 07 | 3.8 | |
| 16 | 04/26/92 | 08:36:53.7 | 40.682 | 124.037 | 11 | 2.6 | |
| 17 | 04/26/92 | 08:45:47.4 | 40.365 | 124.547 | 08 | 3.3 | |
| 18 | 04/26/92 | 08:53:11.5 | 40.417 | 124.694 | 21 | 3.1 | |
| 19 | 04/26/92 | 08:58:45.8 | 40.364 | 124.421 | 11 | 2.4 | |
| 20 | 04/26/92 | 09:24:21.9 | 40.423 | 124.380 | 01 | 4.0 | |
| 21 | 04/26/92 | 10:06:07.5 | 40.305 | 124.315 | 09 | 3.3 | |
| 22 | 04/26/92 | 10:52:44.0 | 40.520 | 124.908 | 05 | 3.1 | |
| 23 | 04/26/92 | 11:18:25.7 | 40.378 | 124.575 | 22 | 6.5 | $1.0 \times 10^{19}$ |
| 24 | 04/26/92 | 12:36:20.9 | 40.310 | 124.424 | 14 | 3.3 | |
| 25 | 04/26/92 | 12:40:07.0 | 40.369 | 124.548 | 15 | 2.8 | |
| 26 | 04/26/92 | 12:41:02.8 | 40.386 | 124.529 | 20 | 3.0 | |
| 27 | 04/26/92 | 12:41:43.4 | 40.307 | 124.411 | 13 | 2.6 | |
| 28 | 04/26/92 | 12:45:19.0 | 40.415 | 124.376 | 19 | 2.4 | |
| 29 | 05/01/92 | 04:15:37.4 | 40.273 | 124.575 | 17 | 3.5 | $1.9 \times 10^{14}$ |
| 30 | 05/01/92 | 15:42:57.0 | 40.360 | 124.533 | 24 | 3.7 | $9.3 \times 10^{13}$ |
| 31 | 05/01/92 | 22:41:51.9 | 40.325 | 124.655 | 07 | 3.6 | $1.9 \times 10^{14}$ |
| 32 | 05/01/92 | 22:59:42.0 | 40.357 | 124.693 | 21 | 3.3 | $1.6 \times 10^{13}$ |
| 33 | 05/02/92 | 09:41:43.5 | 40.319 | 124.292 | 15 | 4.1 | $2.8 \times 10^{14}$ |
| 34 | 05/02/92 | 11:30:31.2 | 40.300 | 124.493 | 21 | 4.3 | $2.4 \times 10^{14}$ |
| 35 | 05/04/92 | 00:13:27.7 | 40.342 | 124.518 | 19 | 3.6 | $4.3 \times 10^{14}$ |
| 36 | 05/04/92 | 07:08:19.0 | 40.308 | 124.423 | 25 | 3.9 | $4.6 \times 10^{14}$ |
| 37 | 05/04/92 | 07:44:41.7 | 40.288 | 124.517 | 28 | 3.7 | $3.3 \times 10^{14}$ |
| 38 | 05/04/92 | 09:32:16.2 | 40.352 | 124.708 | 09 | 3.8 | $5.7 \times 10^{14}$ |
| 39 | 05/04/92 | 10:09:04.0 | 40.643 | 124.547 | 15 | 3.9 | $8.6 \times 10^{14}$ |
| 40 | 05/05/92 | 10:46:17.6 | 40.318 | 124.362 | 17 | 4.5 | $6.6 \times 10^{15}$ |
| 41 | 06/05/92 | 21:46:41.9 | 40.273 | 124.552 | 21 | 4.8 | $7.1 \times 10^{16}$ |

[1]Data for earthquakes obtained from the Preliminary Determination of Epicenters (NEIC, National Geophysical Data Center, Boulder Colorado), and from the University of California, Berkeley Seismographic Station Bulletin.
[2]Seismic Moment listed when available.

Figure 2.1. Tectonic and bathymetric (inset) map of the Cape Mendocino Region (100-m contours). Bathymetric and continental fault inset map is after Wilde et al. (1985). Open and numbered circles show the seismic epicenters and T-wave derived locations, respectively, of the mainshock (1) and two largest aftershocks (2,3). Arrows depict the relative motions and rates of the Pacific and Juan de Fuca plates for a time frame ending at 0.5 Ma (Riddihough, 1984). Also shown are the Harvard CMT solutions for each event. Each mechanism is a lower hemisphere projection, with the compressional quadrant shaded. CSZ is the Cascadia Subduction Zone, SAF is San Andreas Fault.

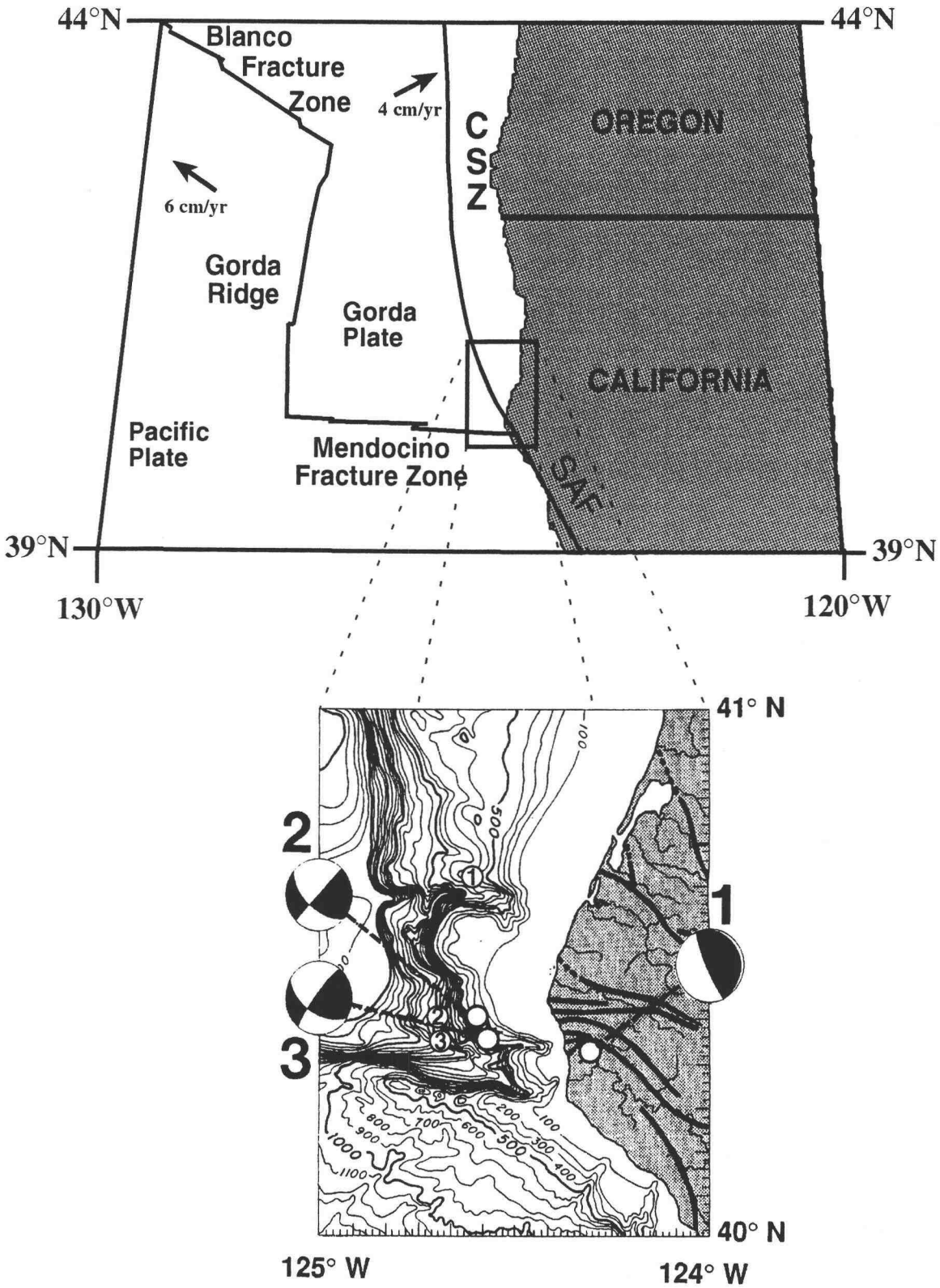
44°N
44°N
Blanco
Fracture
Zone
4 cm/yr
6 cm/yr
CSZ
OREGON
Gorda
Ridge
Gorda
Plate
CALIFORNIA
Pacific
Plate
Mendocino
Fracture Zone
SAF
39°N
39°N
130°W
120°W
41° N
2
1
3
40° N
125° W
124° W

Figure 2.1

Figure 2.2, 2.3, and 2.4. The hydrophone time series and corresponding sonogram of the mainshock (2.2: $M_L$=6.9 OT:18:06 UTC)) and the two largest aftershocks (2.3: $M_L$=6.2 OT:07:41; 2.4: $M_L$=6.5 OT:11:18) from each of the SOSUS hydrophone arrays that recorded the events. The arrays range in epicentral distance between ~ 400 km and ~5200 km. Time on the diagram is vertical (minute marks are labeled) with the data spanning ~76 minutes. The sonograms represent a series of amplitude spectra calculated from successive 1 second segments of hydrophone data. The hydrophone records are sampled at 128 Hz, yielding a 0 to 64 Hz spectrum (0.6-50 Hz after bandpass filtering). The P- and T-waves are denoted with arrows. P-waves are only detected by the hydrophones < $10^o$ in epicentral distance (i.e. phones 1,3, and 5).

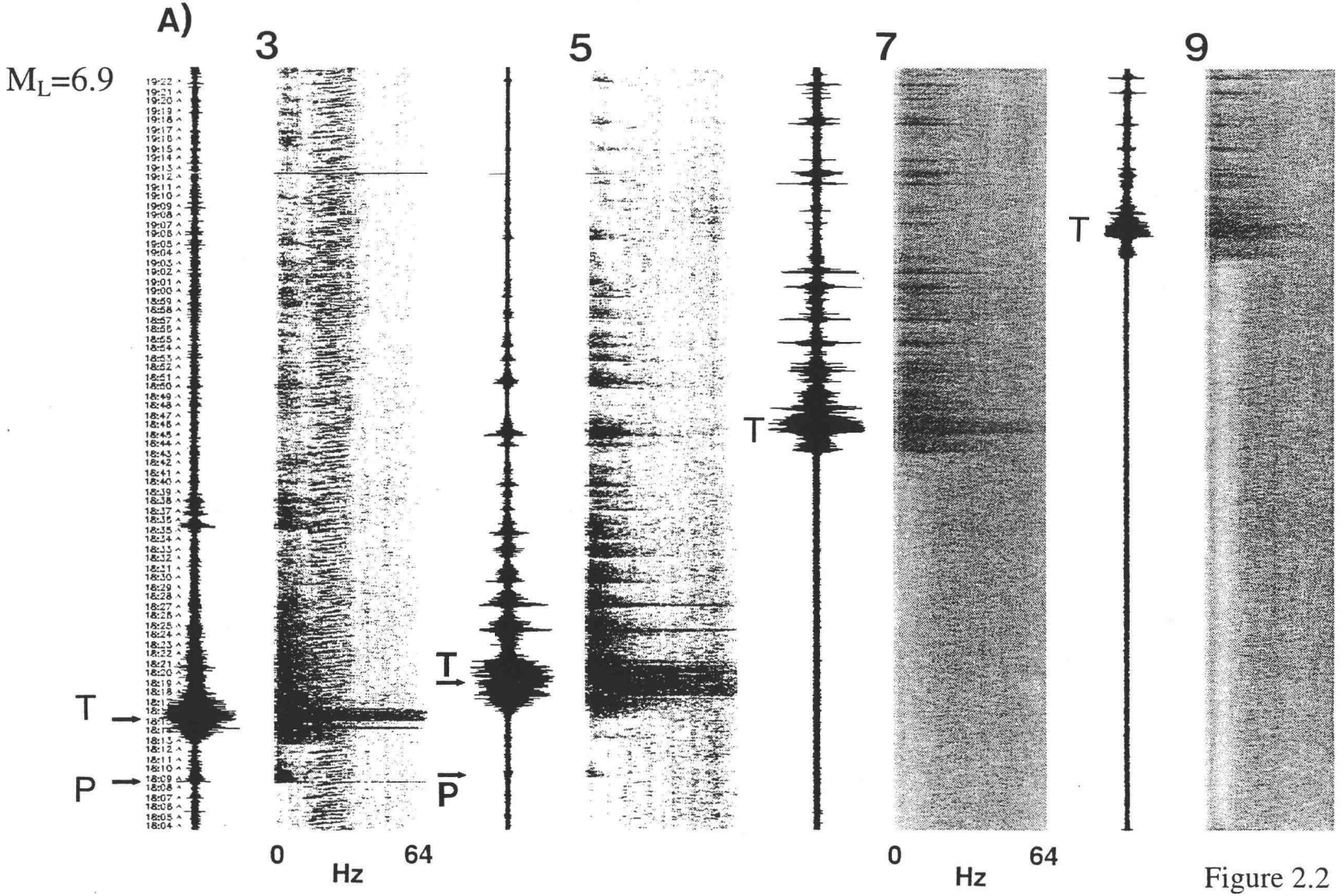


Figure 2.2

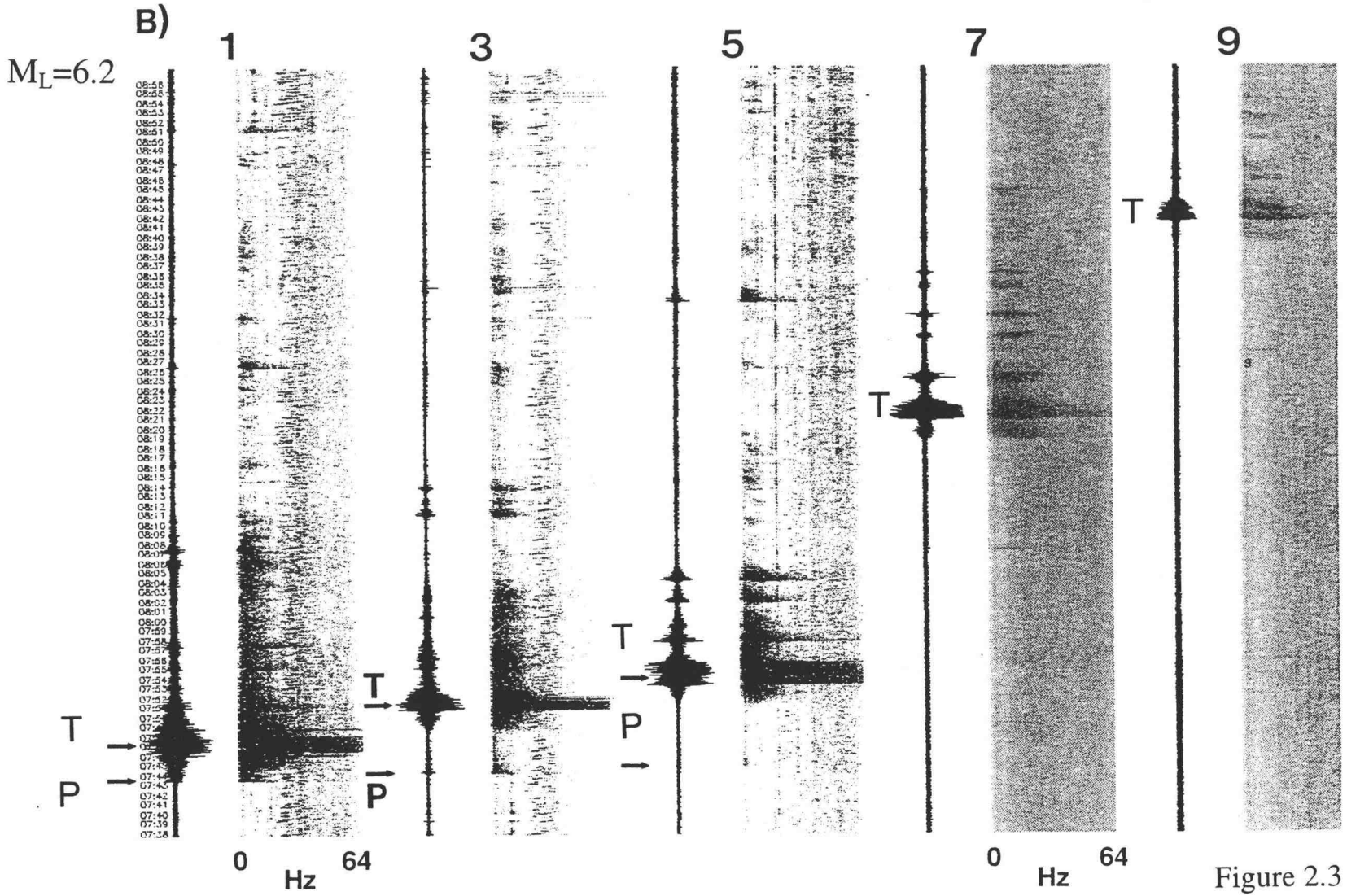


Figure 2.3

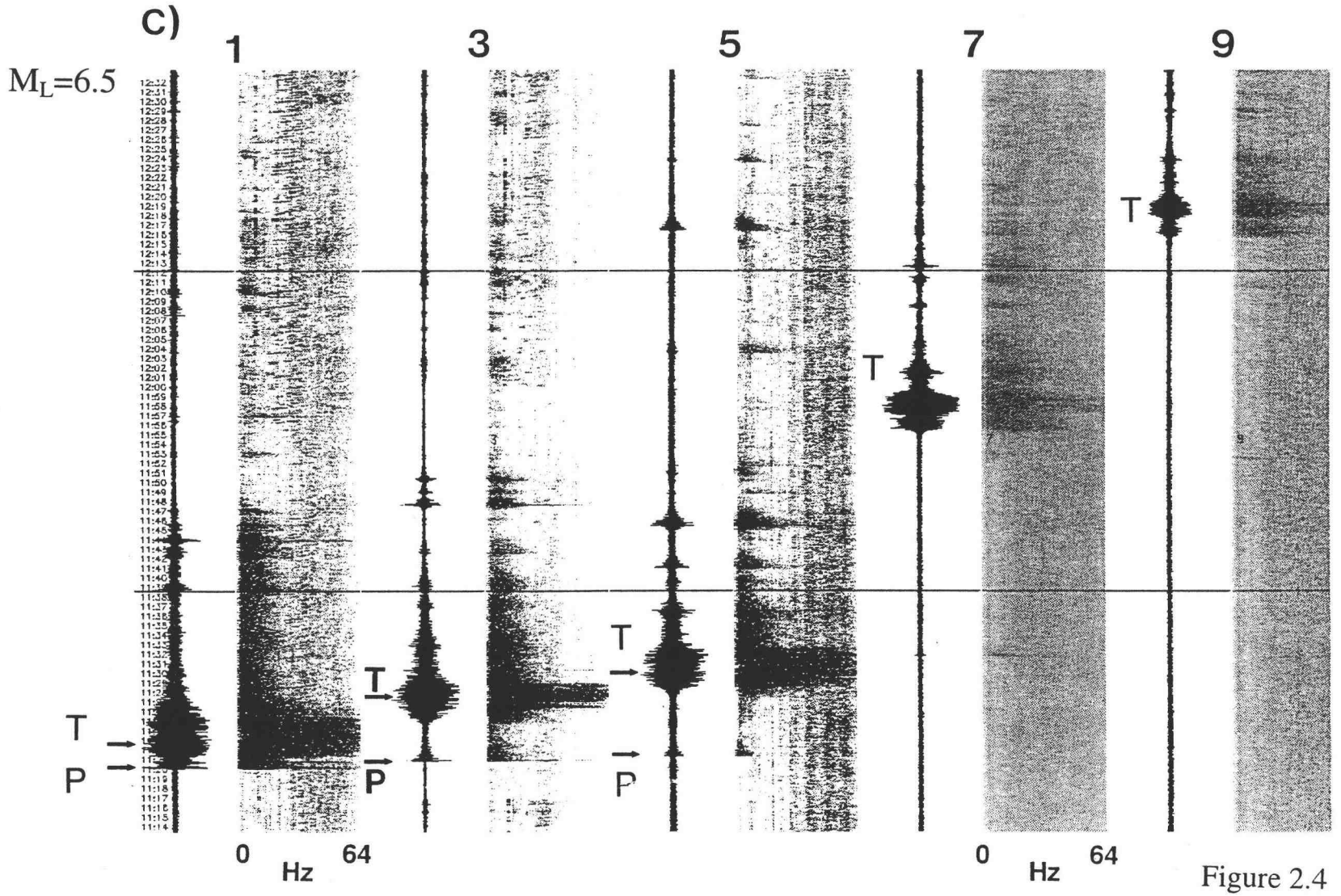


Figure 2.4

The mainshock on April 25 was exceptional for several reasons. The shock generated a tsunami (Oppenheimer et al., 1993), produced distinct uplift along a 25 km section of coastline, and is the largest historic earthquake in this region to have occurred as a result of thrust faulting within the Cascadia subduction zone (Dengler et al., 1992). The distribution of aftershocks, the observation of a broad zone of ground failure, the tsunami, the extent of coastal uplift, and the overall pattern of elevation change led Oppenheimer et al. (1993) to suggest that the mainshock was a thrust event on a shallow dipping fault plane. Furthermore, Velasco et al. (1994) showed that the rupture propagated updip and to the southwest (~262°), however, it is still unclear whether the mainshock was on the North American - Gorda plate megathrust or was solely a North American intraplate event. The SOSUS-derived location for the event, estimated from the arrival times of the peak amplitude of the T-wave packet (Fox et al., 1994), is 40.721°N 124.594°W, origin time of 18:06:15Z (see Figure 2.1). This location is about 46 km north and west of the epicentral location based on the seismograph network. Since the SOSUS-derived location for this earthquake should be the location where the T-wave enters the ocean sound channel, we interpret the hydrophone location to result from the propagation of the P-wave from the earthquake hypocenter, through the continental crust near Cape Mendocino, to the T-wave conversion location along the continental margin. This particular location for the T-wave epicenter may partly be an artifact of array geometry (all hydrophones are to the north and west of this location) and partly due to the bathymetric ridge (south of the T-wave location) enhancing down-slope conversion. The slant-range distance between the seismic hypocenter and the acoustic epicenter in the sound channel is ~48 km, and assuming a P-wave velocity in the shallow crust of roughly 5 km/sec, results in the acoustic/seismograph origin-time difference of 10 seconds.

The large ($M_L$ = 6.2 and 6.5) aftershocks, which occurred 13 and 17 hours after the mainshock, respectively, were within the Gorda plate (Oppenheimer, et al., 1993). First-motion and moment-tensor analysis (Dziewonski et al., 1993) of these events indicates strike-slip faulting resulting from north-south compression within the Gorda plate. Directivity analysis of the events (Velasco et al., 1994) suggests that the rupture for the first aftershock propagated to the northeast (~35° azimuth), while the second aftershock ruptured to the southeast (~132° azimuth). The SOSUS derived locations for these events are 40.477°N 124.659°W origin time of 07:41:44Z and 40.458°N 124.636°W origin time of 11:18:31Z (Figure 2.1 and 2.3). These locations place the earthquakes roughly 8 and 14 km to the northwest and further down the continental shelf, respectively from the epicentral locations based on the seismograph network. This northwestward difference between the seismic and acoustic locations may reflect the P- to T-wave conversion process. The slant-range distance from the aftershock hypocenters to the T-wave conversion location in the sound channel (epicenter) are about 22 and 26 km, the first large aftershock being slightly deeper than the second. Assuming a P-wave velocity of ~5 km/sec, this results in the observed 4 and 5 second differences between the seismic and acoustic origin times. The T-wave aftershock epicenters probably lie to the north and west of the seismic epicenters for the same reason as the mainshock does, partly due to array geometry and partly due to bathymetry in that direction enhancing down-slope conversion.

### *2.3.3 Tsunami and Marine Slide*

The main shock of the Cape Mendocino sequence generated a tsunami recorded by NOAA sea level gauges in California, Oregon, and Hawaii (Oppenheimer et al., 1993). The closest gauge to the epicenter (~40 km at Eureka, CA) recorded a clear compressional first-motion which is consistent with uplift in the source region (Oppenheimer et al., 1993).

No obvious tsunamis were observed from either of the two largest aftershocks (E. N. Bernard, NOAA/PMEL, pers. comm.). However, a submarine cable break occurred near the intersection of the Mendocino and Mattole Canyons a few minutes after the second large aftershock (Commander, Naval Ocean Prediction Facility, Pearl Harbor, Hawaii, pers. comm.). The break occurred at 40° 20' N; 124° 40' W, with an error radius of 1' (Figure 2.6). A probable explanation for the cable break was the occurrence of a submarine slide/debris-flow along the north side of the Gorda Escarpment, triggered by the second large offshore aftershock. Inspection of the bathymetry from this area shows it to be replete with slump features (Figures 2.5 and 2.6). The slump features were probably caused by a combination of shaking from past earthquake strong-ground motion, and erosional undercutting along the walls of the submarine canyon. Review of the hydrophone records of the second large aftershock (Figure 2.4 and Figure 2.8) shows the direct lithospheric phase arrival to have a significantly higher amplitude and frequency than the other two large events. There is no obvious characteristic T-wave signal attributable to a slump; however, phone 1 T-waves from the second large aftershock seem to exhibit a longer duration, higher energy coda. Oppenheimer et al. (1993) observed that the second large aftershock produced P-waves with amplitudes 2 to 4 times larger (and with higher frequencies between 0.3 and 3 Hz) at azimuths near 130° as compared to the other two M > 6 events. This difference was shown to be due to the southeast rupture directivity of the second aftershock (Velasco et al., 1994). The 130° - 132° azimuth puts the rupture direction of the second aftershock toward the source of the marine slide, which may mean the rupture directivity of the second aftershock played a role in initiating the slide event.

A study by Kanamori and Kikuchi (1992) suggests two mechanisms for tsunamigenesis. The first occurs in subduction zones with a large sediment accretionary prism (like the CSZ) where tsunamis are generated through slumping associated with large

Figure 2.5. Sea Beam bathymetry, offshore Cape Mendocino. Scale is 1:150000, contour interval is 100 m.

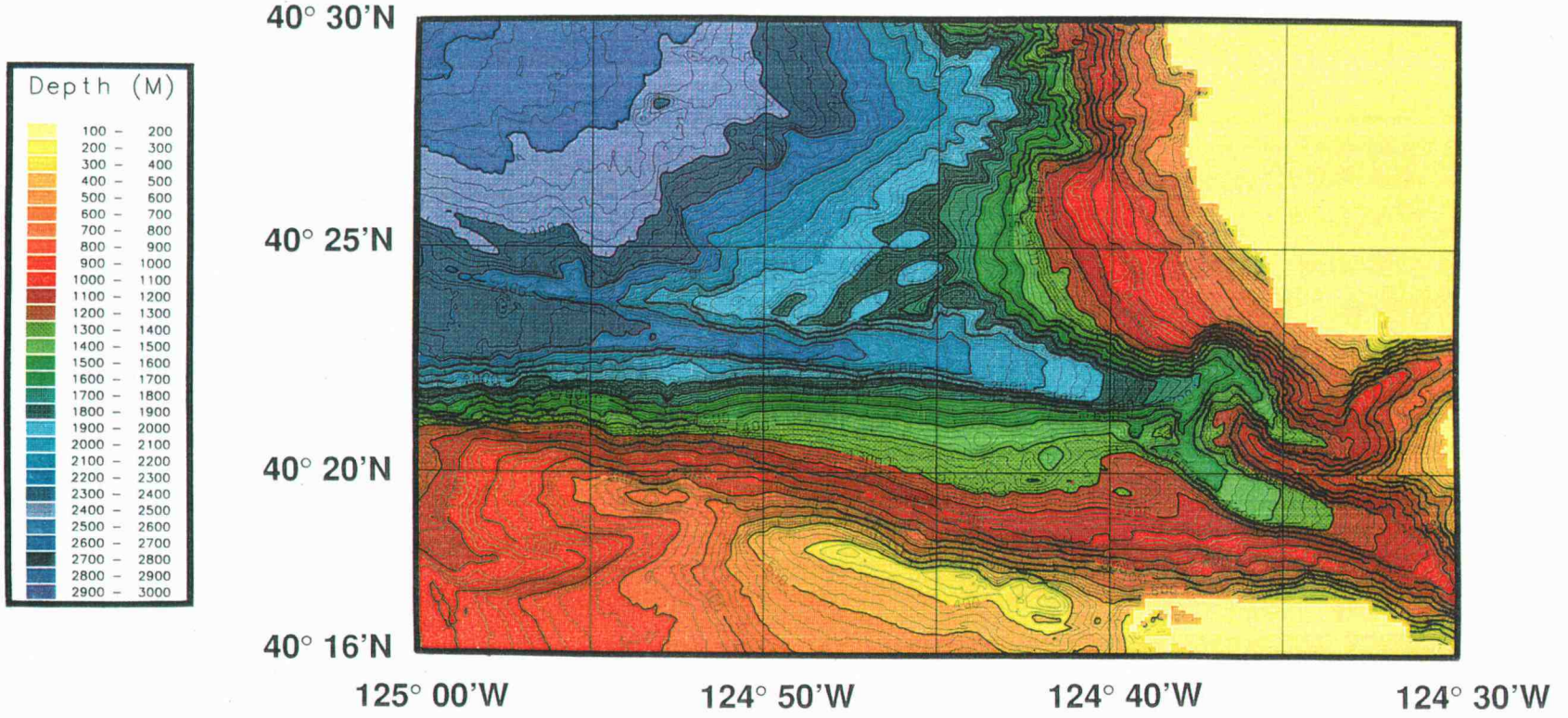
Depth (M)
100 – 200
200 – 300
300 – 400
400 – 500
500 – 600
600 – 700
700 – 800
800 – 900
900 – 1000
1000 – 1100
1100 – 1200
1200 – 1300
1300 – 1400
1400 – 1500
1500 – 1600
1600 – 1700
1700 – 1800
1800 – 1900
1900 – 2000
2000 – 2100
2100 – 2200
2200 – 2300
2300 – 2400
2400 – 2500
2500 – 2600
2600 – 2700
2700 – 2800
2800 – 2900
2900 – 3000
40° 30'N
40° 25'N
40° 20'N
40° 16'N
125° 00'W
124° 50'W
124° 40'W
124° 30'W

Figure 2.5

Figure 2.6. Sketch map of significant geologic features and major bathymetric contours interpreted from Figure 2.5. Inferred submarine slump scars are outlined and indicated by a large "S", with the direction of the slide indicated by the arrows. Slump debris at the base of the slide is marked by a "D". Drainage paths are shown by dashed lines. The locations of the Mattole and Mendocino Canyons and Gorda Escarpment are labeled. The epicenters (from Oppenheimer et al., 1993) estimated for the two large-offshore aftershocks are shown by the stars. Numbered circles show the T-wave derived locations for these events. The location of the cable break is denoted with an "X". The area is replete with slump features, many of these features are most likely seismogenic. The close timing of the cable break and third large aftershock suggests they are related events. Thus the most probable scenario is one in which the $M_L$=6.5 earthquake triggered a debris slide that broke the cable, rather than the earthquake actually rupturing through it.

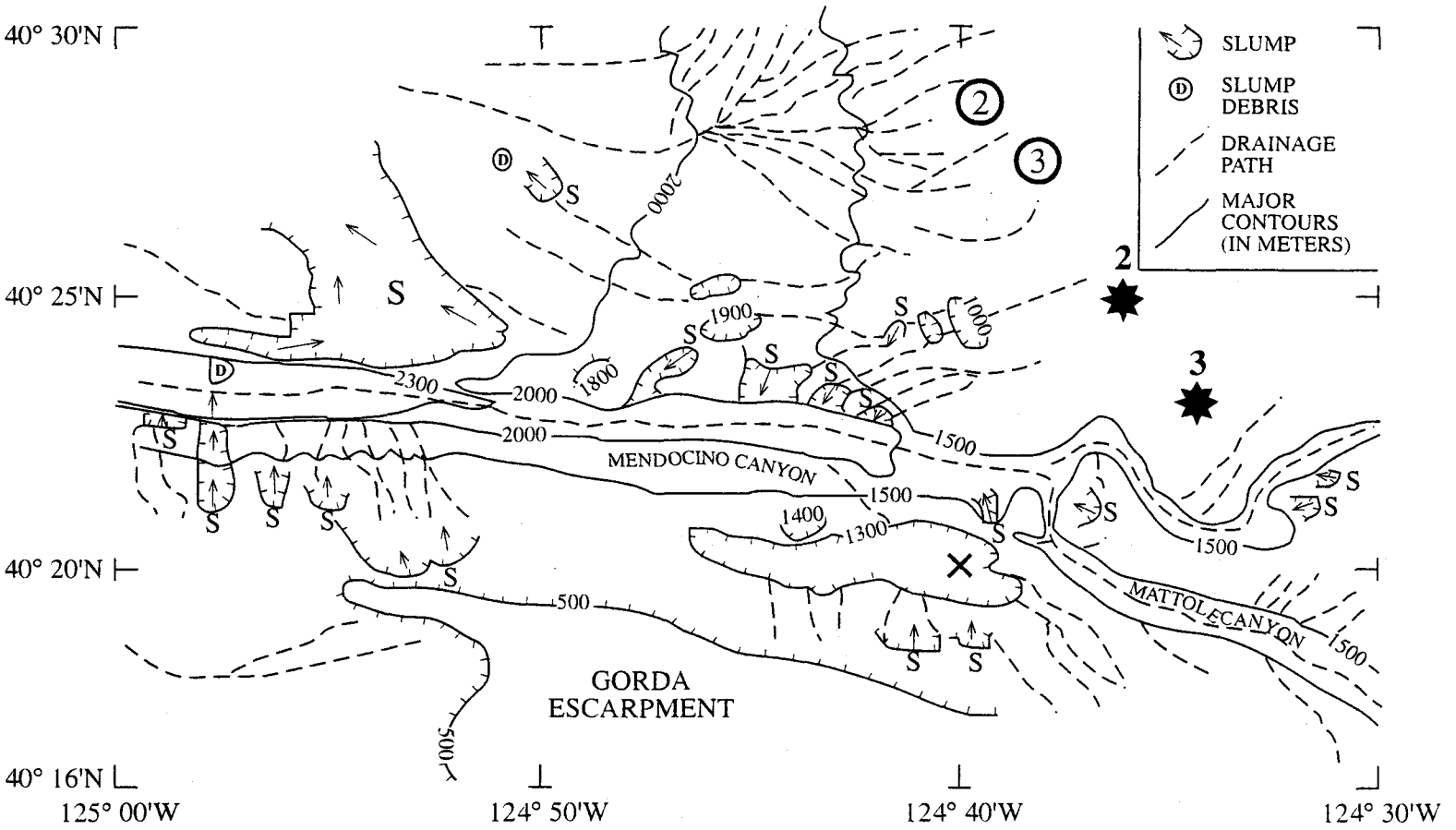
40° 30'N
40° 25'N
40° 20'N
40° 16'N
125° 00'W
124° 50'W
124° 40'W
124° 30'W
SLUMP
SLUMP DEBRIS
DRAINAGE PATH
MAJOR CONTOURS (IN METERS)
MENDOCINO CANYON
MATTOLE CANYON
GORDA ESCARPMENT
2
3
2300
2000
1900
1800
1500
1400
1300
1000
500

Figure 2.6

thrust earthquakes. The tsunami can only occur as a result of slumping because an individual thrust event will not likely rupture through the entire clastic wedge to the seafloor. The second mechanism occurs in subduction zones with an absence of sediment in the trench (i.e. offshore Nicaragua) where the displacement at the seafloor caused by the rupture of an interplate thrust event generates a tsunami. The occurrence of the slump after the second large aftershock (without generating a tsunami) appears to indicate that in the Cape Mendocino (CSZ) case, the tsunami was associated with uplift during an earthquake rather than with a marine slide. Of course there are several unknown details about the slide that may invalidate this statement, e.g. the volume of the slide, the sediment rigidity, aspect ratio of the slide, and the steepness of the slope on which the slide occurred. Furthermore, the difference in fault motion between the mainshock and second large aftershock may have played a pivotal role in determining which event generated a tsunami, although the exact relationship between fault motion and tsunamigenesis are not well understood (F. Gonzalez, NOAA/PMEL, pers. comm.).

## 2.4 Acoustic Data Discussion

Figure 2.2, 2.3, and 2.4 shows a hydrophone time series and corresponding sonograms of the mainshock and two large aftershocks from each of the SOSUS hydrophone arrays that recorded the events. The large amplitude signal present on each of the records is the direct T-wave arrival from each earthquake recorded at about 40 dB above ambient noise over the frequency range of 0 - 64 Hz. All hydrophone data are recorded at a 128 Hz sample rate with a high-pass filter at 0.6 Hz, and a low-pass eight-pole elliptic filter at 50 Hz. Numerous aftershocks are present within the coda of each event. Hydrophones 1, 3, and 5 were close to the epicenter ($\Delta < 10^{\circ}$), and recorded a crustal P-wave from each

earthquake. This crustal wave is the low frequency energy (0.6 ~ 10.0 Hz) that is the first arrival on the hydrophone records from each earthquake. Unidentified signals are also present within the hydrophone data as illustrated in the spectra by the short duration (~ 30 sec) upsweeping signals between 15 - 30 Hz on phones 1 and 3. These signals locate in the south Pacific at 51°S -150°W, have extremely loud source levels, are seen on hydrophone records throughout the Pacific basin, and are the subject of debate within the acoustics community. The extreme signal loudness and periodicity suggest a geologic source, whereas their short duration, swept frequency, and seasonal variation suggest a whale vocalization as the source. No ground-truth information is presently available to help resolve the issue. The following discussion will focus on the analysis of the lithospheric (seismic) P-waves and oceanic (acoustic) T-waves.

### *2.4.1 Lithospheric Phases*

Figure 2.7 shows the time series record of the mainshock on hydrophone 3. A lithospheric seismic wave is evident (most likely a direct crustal P-), but truncated in frequency by the roll-off of the hydrophone instrument response below 0.6 Hz. In recording acoustic waves, the bottom-mounted hydrophones convert pressure changes induced by the seismic wave arrival to voltage. The ability of the hydrophones to detect a given seismic wave is influenced by the epicentral distance to the source event, size of the source event, and the angle between the plane of maximum particle motion and the seafloor made by the incidence angle of the seismic wave. Empirical estimates based on observation of hydrophone records from several moderate sized earthquakes (M ~ 5 - 7) suggests the epicentral distance must be less than 10° in order for the seismic waves to be detected by the hydrophone arrays. This may occur since at large ranges the high-frequency (> 1 Hz) seismic signal components detectable by the hydrophones are probably attenuated.

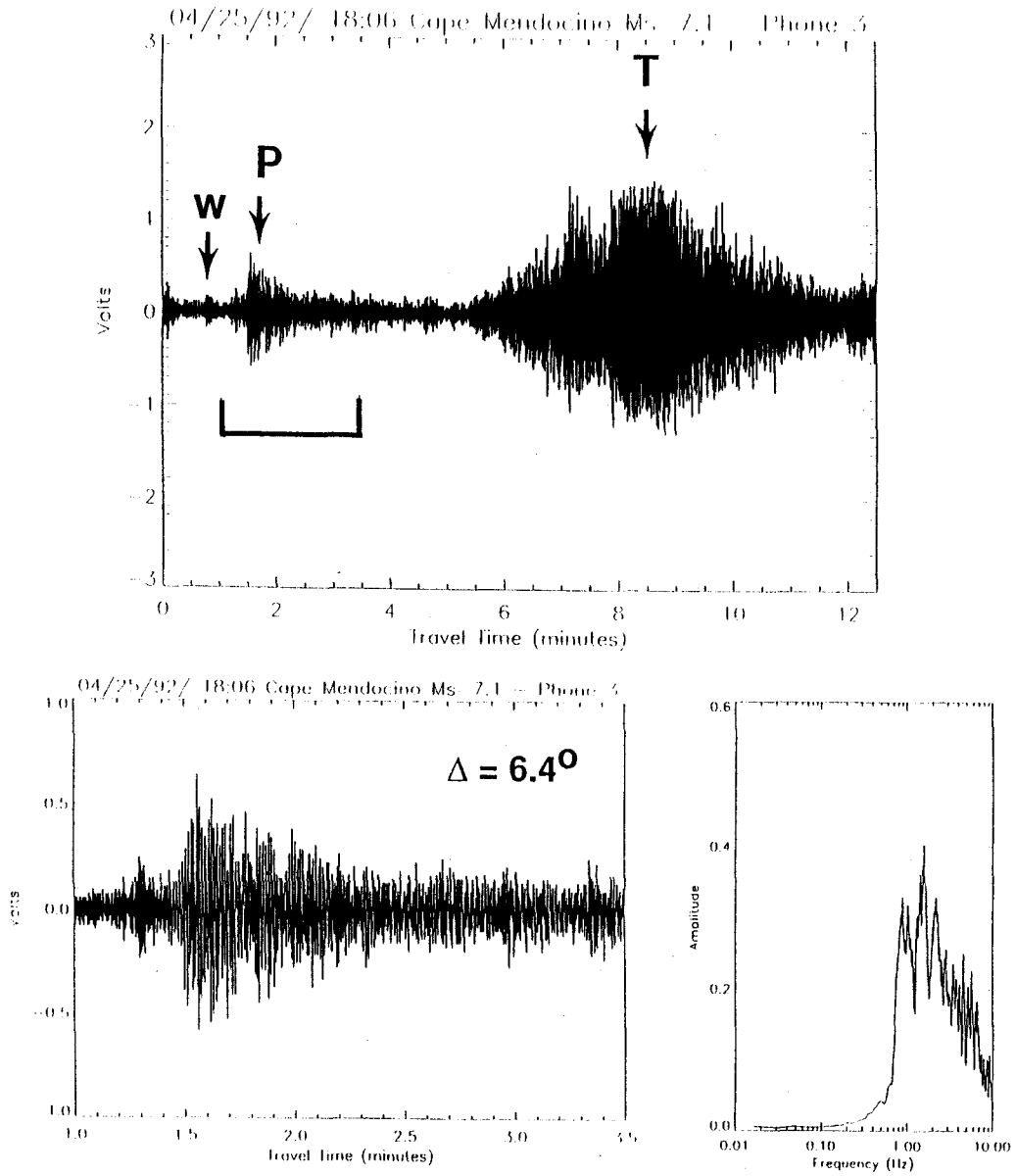


Figure 2.7. Time series of P- and T-waves from hydrophone 3 of the mainshock, with inset showing smaller time window of P-wave and its corresponding frequency spectra. The "W" shows the location of an unknown signal (possibly a whale call) within the time series. The P-wave shown was recorded at an epicentral distance of 6.4° with a high S/N ratio. The high frequency energy arriving just before the main P-wave packet (shown in inset) is another whale vocalization. The roll-off in hydrophone response is shown in the P-wave frequency spectra, and begins at 0.6 Hz.

Consequently, the hydrophone arrays are not particularly well suited for first-motion analyses to estimate focal-mechanisms since first-motions are typically estimated from long-period (< 1 Hz) signals recorded at optimal epicentral distances of between 30° and 90°. This was seemingly verified since the first-motion polarity of the large earthquakes observed on the hydrophones was generally not consistent with the focal-mechanisms estimated from inversion (Dziewonski et al., 1993).

Since the arrival times of the three largest Cape Mendocino earthquakes were well recorded by the hydrophone arrays, it was possible to make a crude estimate of mean velocity for the crustal phase. Examples of the P-wave first motion pick (after low-pass filtering at 2 Hz) from each of the three largest events in the sequence are shown in Figure 2.8. Estimating the crustal wave arrival time differences between the hydrophone arrays from the eight available measurements yields a mean velocity estimate of 7.89 km/sec ±0.2. These hydrophone-derived P-wave velocity estimates are consistent with velocity models from the Cape Mendocino region of 4.0 - 8.05 km/s (Walter, 1986), and with models from the Cascadia Subduction Zone of 4.0 - 7.0 km/s (Tréhú, et al., 1994), with both models representing the upper 30 km of crust.

There is no clear evidence of an S-wave within the time series even after low-pass filtering the data at 2.0 Hz (Figure 2.8). An estimate of the S-wave arrival time was made assuming that S-wave velocity is 0.58 times the P-wave velocity. This suggests that at array 3, the S-wave should arrive around 1.1 minutes after the initial P-wave for all three earthquakes, however, the S-wave is not obvious within the crustal wave coda at this arrival time (Figure 2.8). The S-wave may be present at the recording site, but the orientation of the S-wave particle motion induced at the hydrophone may not have had a vertical component strong enough to cause significant depth (pressure) changes. Furthermore, the S-wave radiation patterns as inferred from the focal mechanisms of the three events

Figure 2.8 Hydrophone 3 time series of P-wave coda from each of the largest earthquakes in the sequence. The time series data were low-pass filtered at 2 Hz. Start time for each plot is exactly 1 minute after the earthquake origin time. The first-motion of the P-wave is clear within the data; however, the polarity of the motion is not consistent with the focal mechanism inferred from CMT inversion. The estimated arrival time for the S-wave (calculated using Poisson's relation) is labeled. There is no clear S-wave arrival within the coda, which may be a result of the S-wave arrival not producing vertical motion detectable by the hydrophone arrays.

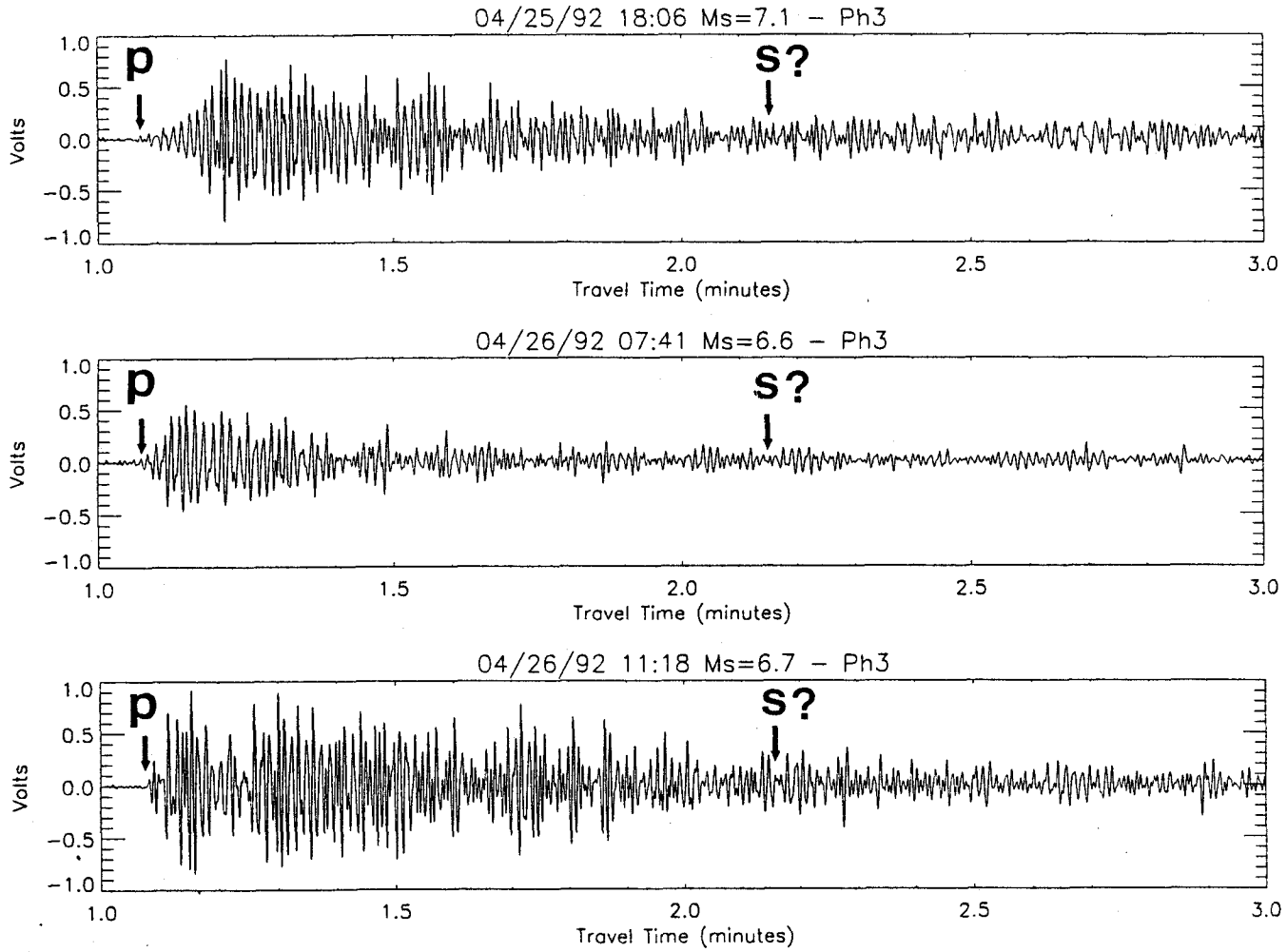
04/25/92 18:06 Ms=7.1 – Ph3
p
s?
Volts
1.0
0.5
0.0
−0.5
−1.0
1.0
1.5
2.0
2.5
3.0
Travel Time (minutes)
04/26/92 07:41 Ms=6.6 – Ph3
p
s?
Volts
Travel Time (minutes)
04/26/92 11:18 Ms=6.7 – Ph3
p
s?
Volts
Travel Time (minutes)

Figure 2.8

(Dziewonski et al., 1993; Velasco et al., 1994) have nodal points near the location of the hydrophones.

*2.4.2 Oceanic Phase*

Analyses of the oceanic phases begin with the modelling of the propagation path of the T-waves from epicenter to receiver. The approximate oceanic path and transmission loss (acoustic attenuation) was estimated using the Parabolic Equation (PE) model. The PE model is based on the Tappert and Hardin (1977) Split Step Algorithm which computes the complex pressure in the water column as a function of depth and distance from the source. Corrections to the pressure estimates involve a spherical-earth approximation and adding a phase error correction which is applied to the index of refraction. The numerical model was run on an IBM RISC 6000 using parameters derived from PC-based software (Holmes et al., 1990). The necessary input parameters for the model to calculate transmission loss are: 1) T-wave source and receiver location (latitude, longitude, depth); 2) an estimate of the seasonal sound-speed profile along the propagation path; 3) seafloor bathymetry along the propagation path at a minimum interval of 5 km; and 4) an estimate of the seafloor lithology, as provided by the Navy's Low Frequency Bottom Loss Table (NOO/SID, 1991). T-waves are generated when the earthquake's seismic waves are transmitted through the seafloor/ocean interface into the water column. Only those exiting acoustic rays with very low take-off angles will become confined within the sound channel and be recorded by the hydrophones at large distances. The PE model would not operate with a sub-seafloor source, so a horizontal point source with a Gaussian beam pattern (20° beam-width, ±10° about horizontal) at the seafloor/ocean interface was assumed to approximate the T-wave origin. The change in transmission loss due to a rough seafloor or the addition of S-wave energy at the seafloor interface was not considered.

A summary of the results from the PE modelling are shown in Figures 2.9a-d. Each color plot represents a cross-section, along the T-wave propagation path from source (left) to receiver (right) of the water column and bathymetry (brown). The transmission loss is plotted as a function of depth and distance from the source for a frequency of 10 Hz. In the transmission loss figures, the location of the first large aftershock is the source location. Figure 2.9a shows the expected transmission loss from source to phone 1; Figure 2.9b shows source to phone 9. Since phone 9 is ~4800 km farther from the source than phone 1, the expected transmission loss is about 10 - 20 dB greater for phone 9 (110 dB) than phone 1 (90 dB). The difference in transmission loss between 1 and 9 is significant, and illustrates the need for a transmission loss estimate along the acoustic propagation path. Figures 2.9c and 2.7d show raypaths from the source to receiver. The PE model predicts that only raypaths with take-off angles between 0° to 6° will reach phone 1, while only rays with take-off angles between -4° to 8° will reach phone 9, with 0° representing horizontal. No other take-off angles resulted in raypaths that became confined within, and propagated along, the sound channel. In Figure 2.9c, the raypaths for take-off angles of 8° and 10° are also plotted; however they do not enter the sound channel before reaching critical transmission loss (~170 dB) because of multiple surface and seafloor reflections. The change in reflection pattern of the raypath plot at a range of 1500 km in Figure 2.9d results from a change in the PE model's estimates of the seafloor lithology, sound velocity, and bathymetric slope. While the raypath frequency input into the model is preserved, the sea surface/seafloor reflection angles do change at that point.

Figure 2.10 shows the transmission loss versus depth and distance from the source to phone 3. The propagation path from the source to phone 3 has an azimuth that cuts eastward across the shallower part of the continental margin. The effect of such a path is to increase the transmission loss by about 50-70 dB because the path is obstructed by margin

Figure 2.9a-d. Summary of PE transmission loss modelling. Each color plot represents a cross-section along the T-wave propagation path from source (left) to receiver (right) of the water column and bathymetry (brown). The source used here was the epicenter of the first large aftershock. Source depth used is seafloor-water interface depth at the earthquake epicenter, and is same for all plots. The color scale within each plot shows the transmission loss (in dB) as a function of depth and distance from the source for a frequency of 10 Hz. Figure (a) shows the loss from source to phone 1, (b) shows the loss from source to phone 9. Phone 9 is ~4800 km (2667 nautical miles (nm)) farther from the source than phone 1, and consequently the expected loss is 10-20 dB greater. Thus the difference in transmission loss between 1 and 9 is significant and illustrates the need to estimate loss along the ray path. Figures (c) and (d) show the estimated raypaths from source to receiver. The PE model predicts that only raypaths with takeoff angles between $0^{\circ}$ and $6^{\circ}$ will reach phone 1, and $-4^{\circ}$ and $8^{\circ}$ will reach phone 9. In Figure (c), the raypaths for takeoff angles of $8^{\circ}$ and $10^{\circ}$ are also plotted; however, they do not reach the sound channel before reaching critical transmission loss (~170 dB) because of multiple seafloor and surface reflections. The change in reflection pattern of the raypath at 1500 km (833 nm) range in (d) results from a change in the PE model's estimates of seafloor lithology, sound velocity, and bathymetric slope. The raypath frequency input is the same, but the seafloor/surface reflection angles do change at that point.

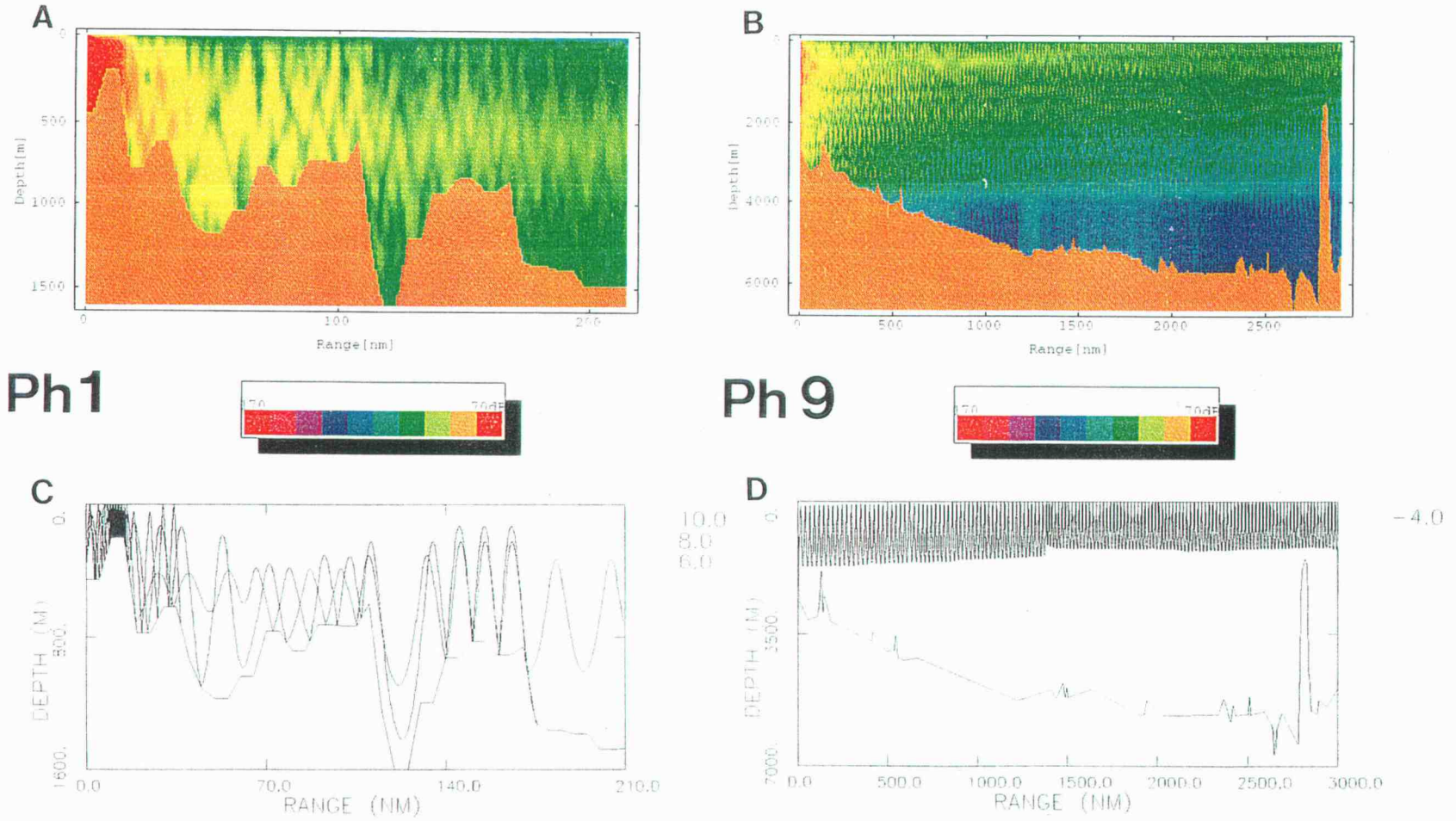
A
Depth [m]
0
500
1000
1500
0
100
200
Range [nm]
B
Depth [m]
0
2000
4000
6000
0
500
1000
1500
2000
2500
Range [nm]
Ph1
Ph 9
C
DEPTH (M)
0.
800.
1600.
0.0
70.0
140.0
210.0
RANGE (NM)
10.0
8.0
6.0
D
DEPTH (M)
0.
3500.
7000.
0.0
500.0
1000.0
1500.0
2000.0
2500.0
3000.0
RANGE (NM)
-4.0

Figure 2.9

Figure 2.10. Transmission loss versus depth and distance from the source (same as in figure 2.9) to phone 3. The T-wave propagation path from source to phone 3 cuts eastward across the shallower part of the continental margin. The effect of such a path is to increase the transmission loss by about 50-70 dB.

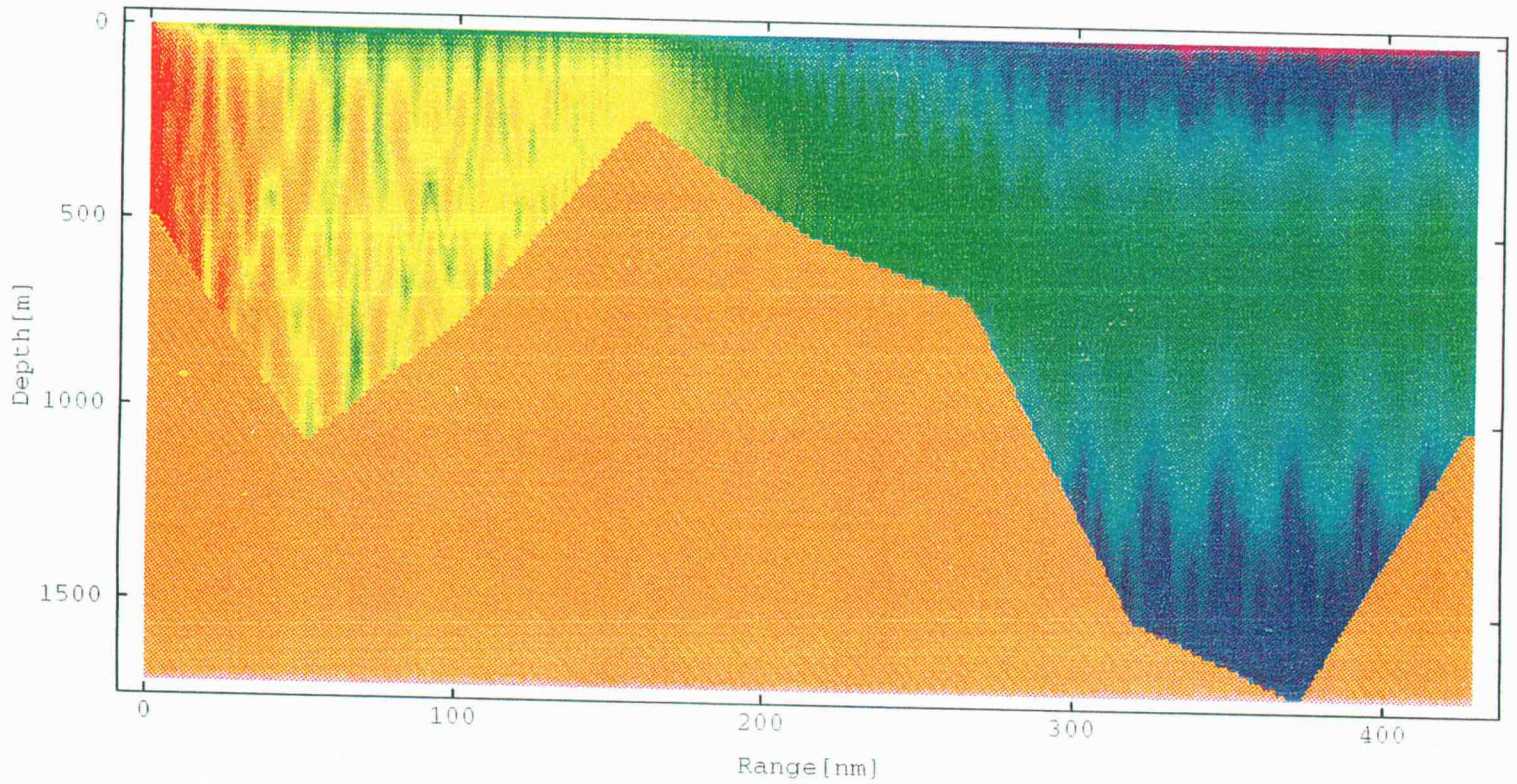


# Ph3

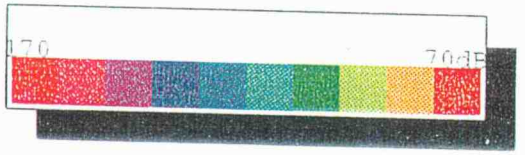

Figure 2.10

bathymetry. Bathymetric obstructions were also present in transmission loss models of the propagation path to phones 1 and 3 for the mainshock and first large aftershock. Since such a large amount of acoustic energy was put into the water column by the three largest earthquakes, the 50-70 dB loss in signal strength could not prevent a sizable amount of energy from reaching hydrophone 3. However, the PE model does predict that the shallow bathymetry will prevent the detection of small, less energetic earthquakes on phone 3. This is illustrated in Figure 2.11 by the records of two small earthquakes ($M_L$=2.4 and 3.1) on hydrophones 1 and 5, but the events are absent on phone 3.

After review of the hydrophone records following the mainshock of the Cape Mendocino sequence, the minimum magnitude earthquake that generated T-waves detectable by the SOSUS hydrophones was $M_L$ = 2.4 (Figure 2.11). This magnitude threshold does not represent an absolute, as not all magnitude 2.4 events were detected. Reliable detection of Cape Mendocino earthquakes begins around $M_L$ = 3.1-3.2. The magnitude 2.4 threshold is by no means the minimum detection level for the SOSUS arrays. The relative geometry of the hydrophone network to northern California is inferior to that of other parts of the northeast Pacific Ocean, and, as shown earlier, bathymetric shadowing is a problem for these near-shore events (Fox et al., 1994). And other factors do influence the detection of small earthquakes by the hydrophone arrays. The record of phone 3 shown in Figure 2.11 has ship noise, whale vocalizations, and earthquakes from other sources which complicate detection and event discrimination.

### 2.4.3 *T-wave Source Level*

A useful quantity to estimate from earthquake hydrophone records is the source level of each event. The source level calculated here is the amount of acoustic energy that an earthquake releases into the ocean at the seafloor-water interface, and is essentially the

Figure 2.11. The hydrophone records and sonograms of two small offshore earthquakes ($M_L$ 2.4 and 3.1) from the April 1992 Cape Mendocino sequence representing ~ 11 minutes of raw hydrophone. The Mendocino earthquakes are not well recorded on hydrophone 3, due to bathymetric obstruction along the T-wave travel path. Whale vocalizations (the short duration, swept frequency signals between 20-40 Hz) and ship noise (narrow band, continuous lines) dominate the records, yet the two small earthquakes are readily apparent. The large signal (BFZ) present late on hydrophones 1 and 3 is from an earthquake of unknown magnitude that occurred within the southeast segment of the Blanco Transform Fault Zone.

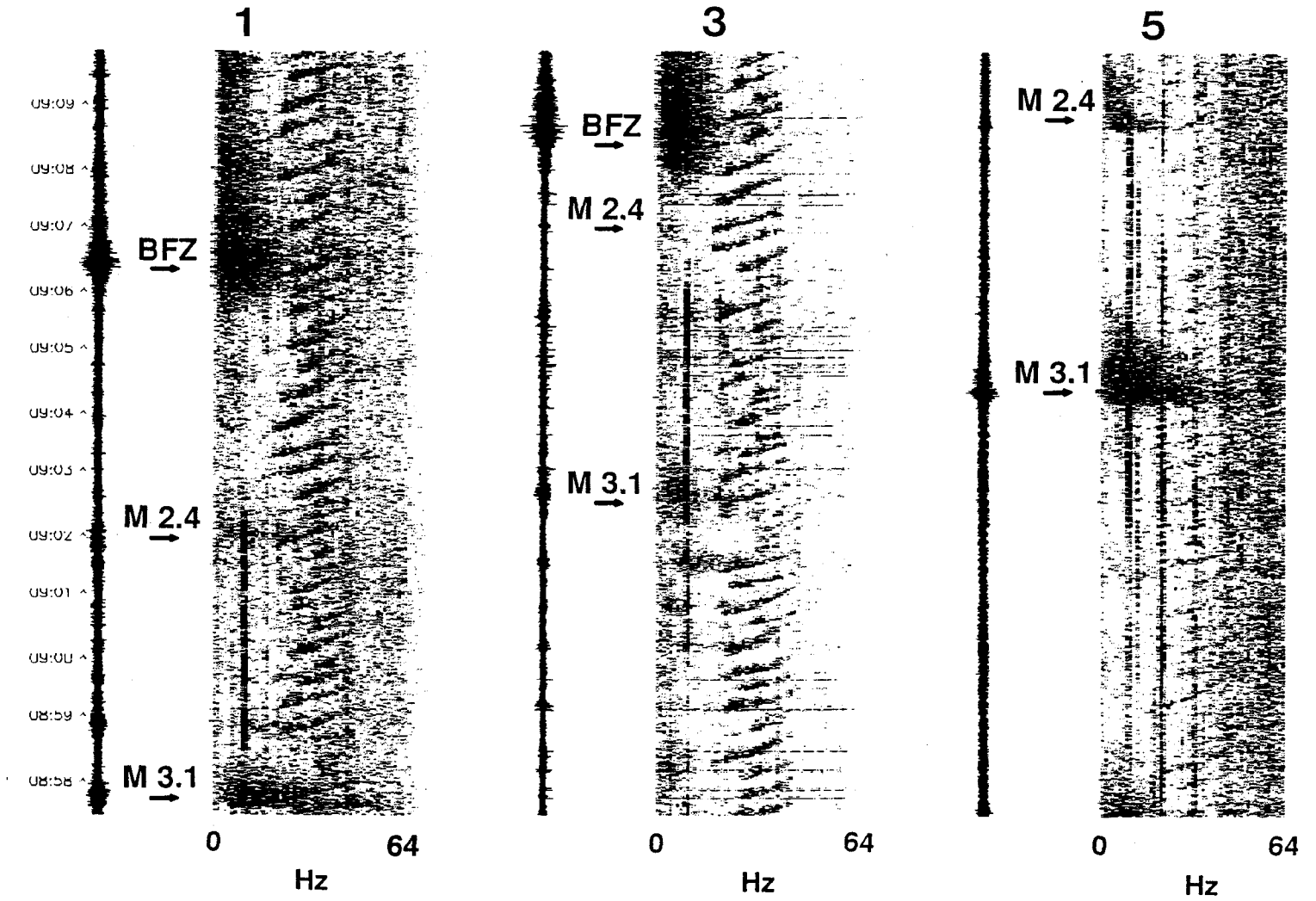
1
3
5
09:09
09:08
09:07
09:06
09:05
09:04
09:03
09:02
09:01
09:00
08:59
08:58
BFZ
M 2.4
M 3.1
0
64
Hz

Figure 2.11

power level recorded at the hydrophone with the instrument response and transmission loss removed. The source level represents power in units of decibels relative to 1 micro-Pascal, normalized by the square root of the spectral bin bandwidth. The first step in estimating source level is to evaluate the optimum frequency band of an earthquake's T-wave packet that provides the highest S/N ratio at a given hydrophone. Figures 2.12a and 2.12b show frequency versus power of T-waves from the largest earthquakes in comparison to ambient noise on phones 1 and 9. The ambient noise spectra were determined from hydrophone data recorded a few minutes prior to each earthquake, with the instrument response removed. Both the T-wave and ambient noise spectra in Figures 2.12a-b were estimated from 5 minutes worth of data (the T-wave event duration), have had the time-series mean removed, and were normalized by the FFT bandwidth. The power level of the earthquake T-waves is significantly above ambient noise over the frequency range of 5-30 Hz. The maximum difference in power level between T-wave and ambient energy is about 20-40 dB at 5-15 Hz.

The source levels of the mainshock, second large aftershock, and a small aftershock from each of the hydrophones that recorded the earthquakes are shown in Figures 2.13a-c. The source level estimates for each phone should be consistent if the transmission loss is modelled properly, and are in fairly good agreement being within about 20 dB of one another. However as illustrated earlier, the PE model's estimate of transmission loss from Cape Mendocino to hydrophone 3 is very large because of bathymetric obstructions along the oceanic travel path. The hydrophone 3 source level of the large earthquakes ($M_L > 6$) becomes excessive, in comparison to the other phones, with the addition of the transmission loss estimates and was therefore not included in Figure 2.13a-c. This suggests that more acoustic energy is being received at phone 3 than the PE model predicts. The cause of the PE model's underestimate may be that the model is only 2-dimensional. Thus the PE model

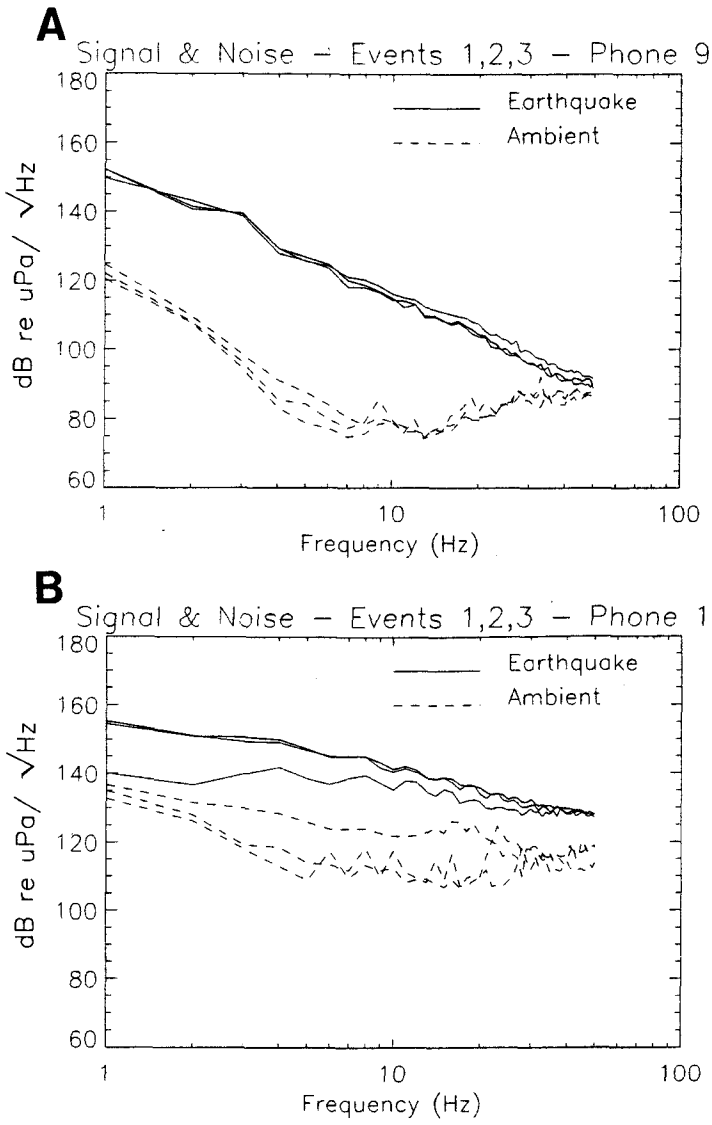


Figure 2.12. Shown is the frequency versus power of T-waves from the three largest earthquakes in comparison to ambient noise on phone 9 (a) and phone 1 (b). Ambient noise was sampled a few minutes prior to each event. Both T-wave and noise spectra in (a) and (b) had the instrument response removed, and were normalized by the square-root of the spectral bin bandwidth. The maximum difference in power level between T-wave and ambient energy is about 20-40 dB at 5-15 Hz, with signal being significantly above noise in the band 5-30 Hz.

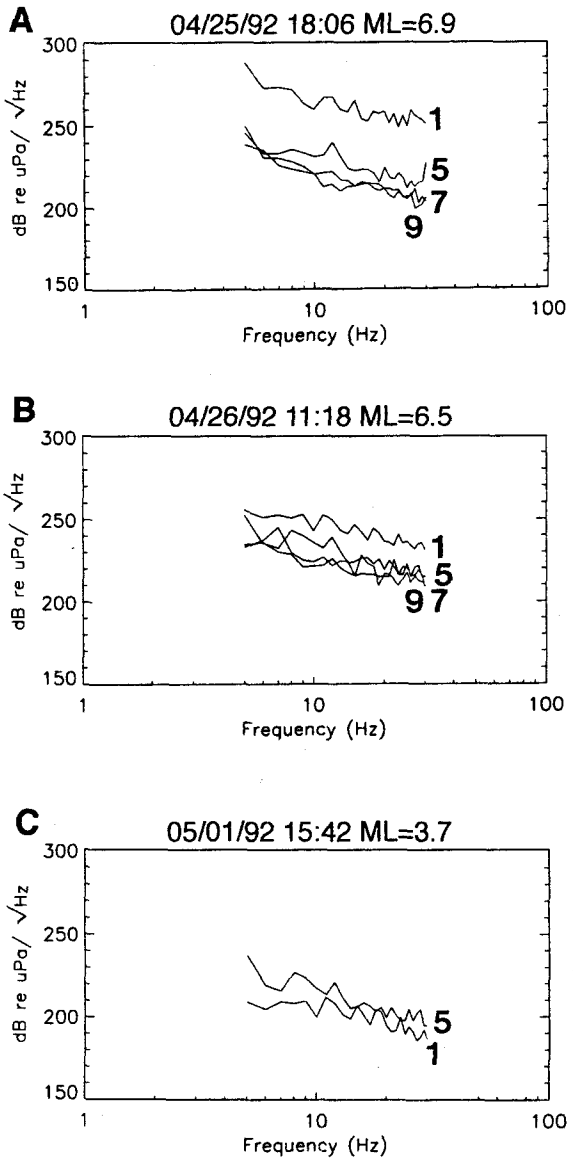


Figure 2.13a-c Shown are the source levels of the mainshock (a), second largest aftershock (b), and a small aftershock (c) from each of the hydrophones that recorded the earthquakes. As illustrated in figure 2.10, the PE model's estimate of transmission loss from Cape Mendocino to phone 3 is very large because of bathymetric obstruction along the travel path. Thus source level at hydrophone 3 becomes excessively large in comparison to the other phones with the addition of the loss estimates. Consequently, source levels from phone 3 were not used to derive a mean source level for the events in this study.

**TABLE 2.2**: Results of Acoustic Source Level Estimation

| Event | Source Level[1] | Number of Stations[2] | Stan Dev[3] | | Epicenter Location[4] |
|---|---|---|---|---|---|
| 1 | 236.851 | 4 | +07.85 | -8.47 | C |
| 2 | 288.758 | 4 | +13.68 | -16.23 | C |
| 3 | 207.087 | 2 | +04.71 | -05.16 | O |
| 4 | 215.900 | 2 | +09.48 | -11.88 | C |
| 5 | 212.986 | 2 | +12.42 | -13.93 | C |
| 6 | 212.554 | 2 | +11.64 | -10.42 | O |
| 7 | 210.839 | 2 | +10.80 | -11.39 | C |
| 8 | 229.971 | 2 | +09.94 | -11.72 | O |
| 9 | 218.289 | 2 | +11.56 | -14.37 | O |
| 10 | 225.651 | 2 | +11.69 | -12.65 | O |
| 11 | 212.441 | 2 | +09.19 | -11.03 | O |
| 12 | 216.127 | 2 | +09.64 | -08.55 | O |
| 13 | 265.880 | 4 | +11.67 | -13.08 | O |
| 14 | 209.531 | 2 | +09.51 | -11.83 | O |
| 15 | 222.959 | 2 | +09.44 | -09.24 | O |
| 16 | 208.078 | 2 | +09.79 | -10.74 | C |
| 17 | 221.677 | 2 | +10.58 | -10.95 | O |
| 18 | 219.068 | 2 | +09.99 | -11.49 | O |
| 19 | 211.886 | 2 | +06.58 | -09.31 | O |
| 20 | 222.417 | 2 | +09.72 | -11.54 | C |
| 21 | 216.648 | 2 | +06.28 | -07.03 | C |
| 22 | 216.184 | 2 | +10.18 | -08.94 | O |
| 23 | 265.601 | 4 | +10.39 | -11.93 | O |
| 24 | 220.024 | 2 | +08.02 | -08.82 | O |
| 25 | 213.317 | 2 | +09.76 | -10.21 | O |
| 26 | 216.532 | 2 | +08.63 | -09.02 | O |
| 27 | 212.274 | 2 | +09.44 | -10.26 | O |
| 28 | 205.615 | 2 | +10.27 | -10.58 | C |
| 29 | 211.361 | 2 | +11.82 | -10.34 | O |
| 30 | 246.908 | 2 | +07.18 | -09.17 | O |
| 31 | 242.444 | 2 | +07.35 | -08.03 | O |
| 32 | 234.322 | 2 | +06.66 | -06.82 | O |
| 33 | 214.952 | 2 | +09.14 | -10.05 | C |
| 34 | 223.900 | 2 | +08.60 | -09.44 | O |
| 35 | 219.430 | 2 | +13.53 | -14.81 | O |
| 36 | 221.035 | 2 | +15.39 | -14.22 | O |
| 37 | 219.957 | 2 | +11.28 | -10.38 | O |
| 38 | 220.248 | 2 | +15.26 | -15.70 | O |
| 39 | 227.876 | 2 | +10.44 | -10.71 | O |
| 40 | 222.500 | 2 | +11.14 | -12.58 | C |
| 41 | 248.731 | 4 | +10.37 | -13.63 | O |

[1]Source level and standard deviation are in units of decibels relative to microPascals (pressure),
normalized by the square-root of the spectral bin bandwidth, at 1 m from source.
[2]Number of stations used to determine average source level.
[3]Asymmetry in error bounds due to formulation in log space.
[4]Epicentral location of earthquake, either continental (C) or oceanic (O).

cannot take into account propagation of T-wave energy that is not on the great circle path to the receivers. This excess energy may arrive at phone 3 through horizontal refraction along the continental margin, or by local reverberation near the receiver. Also the bathymetry used by the model may be too coarse (averaged over 5-minute intervals) to accurately portray the continental margin. Regardless of the cause, the source level estimates from phone 3 were not used in determining each of the 41 earthquakes' mean source level. The source levels derived for phone 1 for the three largest earthquakes are also somewhat overestimated, which is reflected in the error of the mean source level calculation (Table 2.2). This mean source level was calculated by integrating each phone's source level curve over the 5-30 Hz bandwidth, then averaging the integrated values from every hydrophone that recorded the earthquake. This source level averaging technique results in a single source level value with which to describe each earthquake (listed in Table 2.2) and represents the T-wave acoustic power present in the 5-30 Hz band. Thus, this method can be used to quantitatively estimate the sizes, and the size differences, of earthquakes based solely on their acoustic energy release into the ocean water-column.

Another direct method to estimate earthquake size differences utilizing T-wave energy is to find each event's corner frequency within the source power spectrum. Searching for an event's corner frequency assumes that earthquake ocean-acoustic waves have similar source properties as crustal-seismic waves, or at least that the fault parameter information contained within the seismic waves is transferred across the seafloor-water interface to the ocean-acoustic waves. Theoretical estimates of far-field shear displacement spectra can be made from local magnitude using the equations:

$$\log(f_o) = 2.1 - 0.5M_L \quad (1)$$

and

$$\log(W_o) = 1.5M_L - 4.1 \quad (2)$$

where $f_o$ is the corner frequency, $W_o$ is the long-period spectral level, and $M_L$ is local magnitude. Equations (1) and (2) were obtained from Eaton (1977) who reduced the far-field shear displacement spectrum model of Thatcher and Hanks (1973) to a function of only three parameters. Figure 2.14 shows the displacement versus frequency for seismic and acoustic waves for a local magnitude 2.4 earthquake. The observed acoustic energy was converted from pressure to displacement by using equation (3),

$$D = 1 / T (P / (w\ Z)) \qquad (3)$$

where $D$ and $P$ represent ground displacement and acoustic pressure at the source (seafloor-ocean interface), $w$ is angular frequency, $Z$ is the acoustic impedence of water ($1.5 \times 10^5$ gm $s^{-1}$ $cm^{-2}$), and $T$ is the transmission coefficient used to adjust for the change in acoustic wave amplitude as the wave propagates from basalt (with $Z = 1.8 \times 10^6$ gm $s^{-1}$ $cm^{-2}$) into the water column. The theoretical seismic displacement also represents ground displacement at the source (in the crust), and was estimated assuming a crustal density of 2.7 gm/$cm^3$, shear velocity of 4.2 km/sec. The seismic displacement curve does not include effects from the radiation pattern or scattering along the transmission path. The acoustic displacement curves for a magnitude 2.4 earthquake are shown in Figure 2.14, since only earthquakes of $1.3 < M_L < 2.8$ have corner frequencies within the 5-30 Hz T-wave band. The acoustic displacement curves of the $M_L = 2.4$ earthquake show no indication of a corner frequency. The hydrophone records of small earthquakes in this magnitude range (Table 2.1) also lack corner frequencies in their acoustic displacement spectra. The lack of an acoustic corner frequency makes it difficult to directly estimate the seismic size of an earthquake from its hydrophone recorded T-wave. Thus, it is necessary to evaluate empirically the relationship between acoustic source level and seismic moment and magnitude in order to quantitatively derive earthquake size from its hydrophone records.

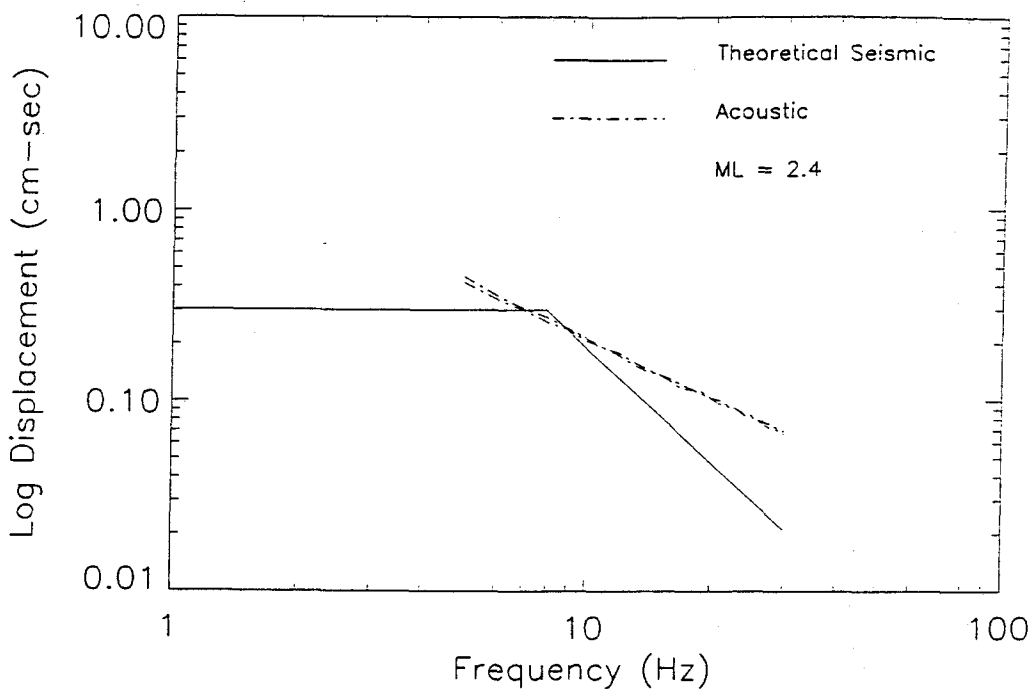


Figure 2.14. Estimates of displacement versus frequency for theoretical seismic and observed acoustic waves from a $M_L$=2.4 earthquake. Log scale reduces scatter in data, making acoustic spectra appear highly linear. Unlike the seismic spectra, the acoustic displacement curves show no indication of a corner frequency. The lack of a corner frequency makes it difficult to directly estimate the fault dimensions of an earthquake from its acoustically recorded T-wave. Therefore, empirical relations between acoustic source level and magnitude and seismic moment are needed to quantitatively derive size estimates of an earthquake from its hydrophone records.

The empirical relation between the source power level of an earthquake and its local magnitude and seismic moment were first investigated using a multiple regression model that addresses the connection between different indicator variables within the data. Figure 2.15 shows the relation between magnitude and power level of the earthquakes analyzed in this study, using an *O* or a *C* if the event was considered either oceanic or continental, respectively. An earthquake is designated as either oceanic or continental depending on whether it was located significantly west or east of longitude 124.40°W (Tables 2.1 and 2.2). This longitude line was chosen because it is the mean longitude of the 300 m bathymetric contour offshore of Cape Mendocino, where 300 meters is the approximate depth at which the sound channel begins in this region (Holmes et al., 1990). The indicator variable regression analysis of the magnitude versus power level relationship yielded two important results: 1) The three large earthquakes ($M_L > 6$) should not be modeled with the rest of the data set, and 2) the difference between the continental and oceanic earthquakes (excluding the three largest events) is significant. In both of these situations the three $M_L > 6$ events should be considered separately because they are so much larger (~10 - 1000 times) than the other 38 events that they dominate the regression model. Also, since a regression fit of 3 data points would be meaningless, the three large events were not considered for regression. This is not the case with any other magnitude range of earthquakes.

Figures 2.16a-b and Table 2.3 show the slopes (with 95% confidence intervals), and y-intercepts of the regression models fit to the oceanic and continental earthquakes ($2.4 < M_L < 5.3$). The difference between the two models is significant and suggests that for equivalent magnitudes, an oceanic earthquake will have a larger source power level than a continental earthquake. This may result from a difference in the seismic propagation path from the earthquake's hypocenter to the sound channel. Seismic waves from continental

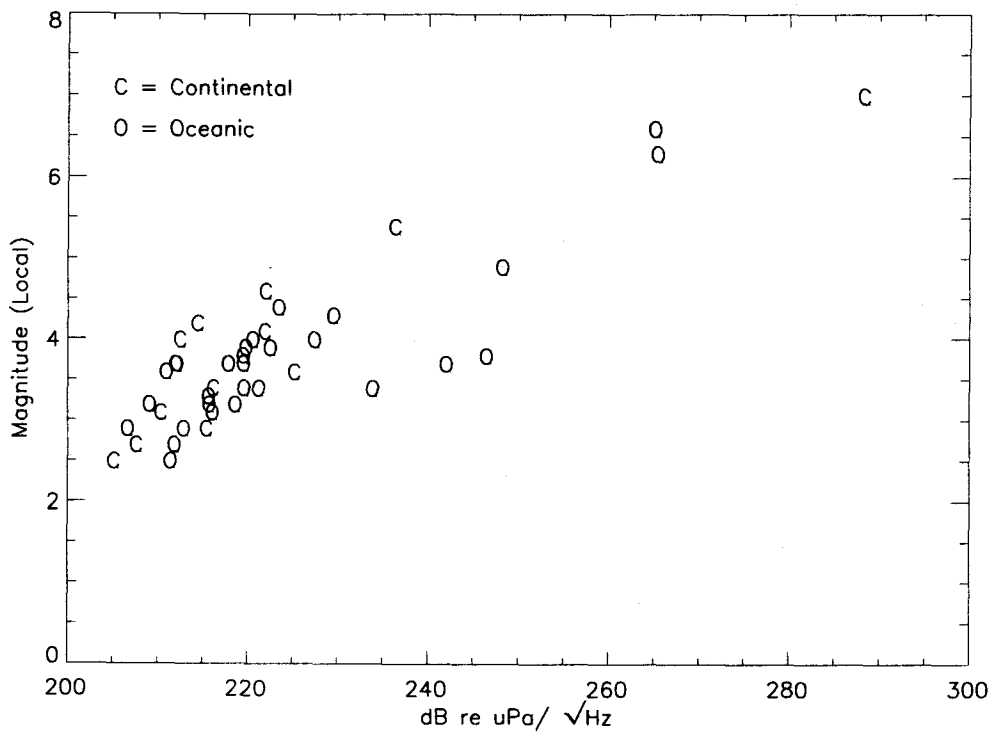


Figure 2.15. Relation between source power level and magnitude from the earthquakes analyzed in this study. O or C indicate whether the earthquake was oceanic or continental, respectively. Indicator regression analyses of the magnitude versus power level relationship yielded two results: The three earthquakes greater than $M_L$ 6.2 should be modelled independently of the rest of the data set, and the difference between continental and oceanic earthquakes is significant (95% confidence interval).

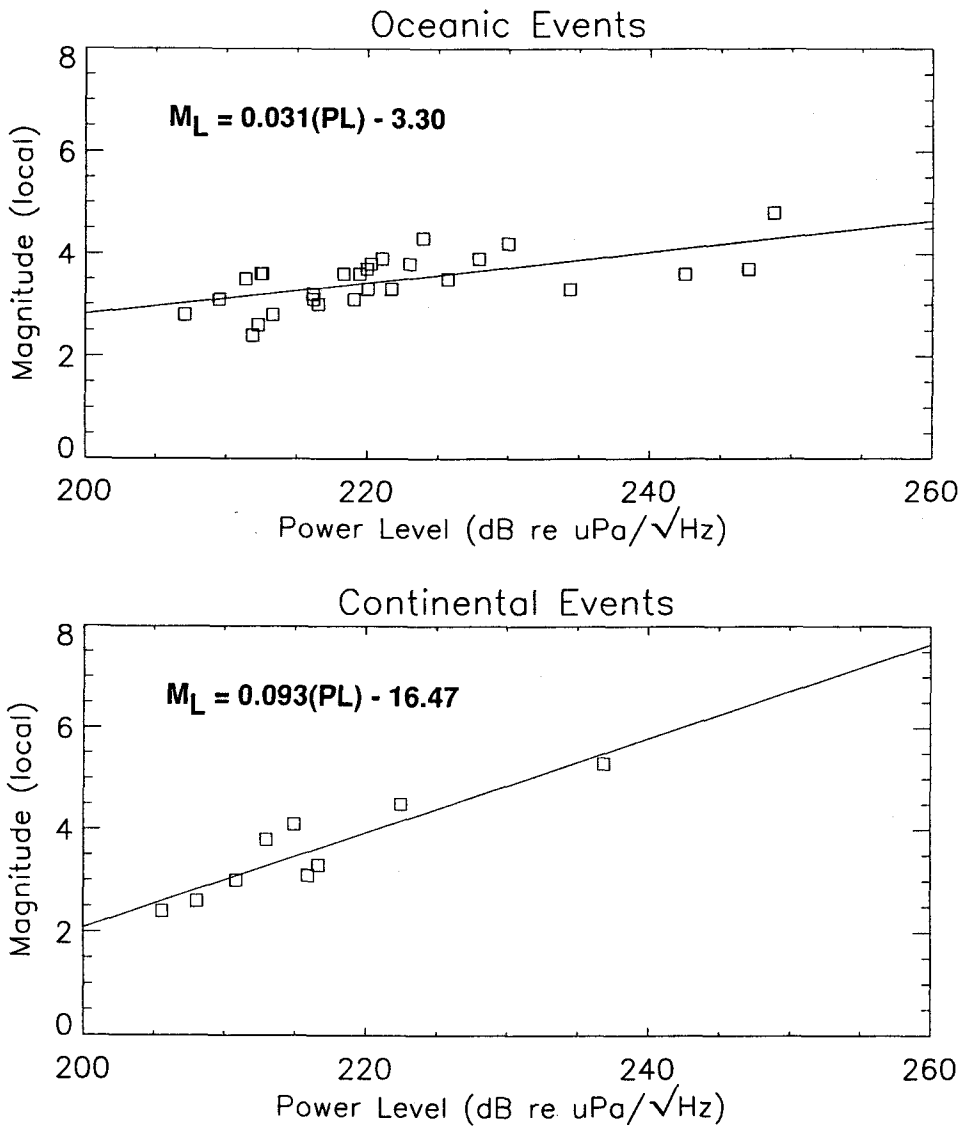


Figure 2.16a-b.The regression models fit to the oceanic (a) and continental (b) earthquakes. The regression model statistics are summarized in Table III. The results suggest that the difference in the models shown in (a) and (b) is significant, and that for an equivalent magnitude earthquake, an oceanic event will have a larger perceived source power level than a continental earthquake.

**TABLE 2.3: Results of Regression Analysis**

| Magnitude versus Power Level | | |
|---|---|---|
| Slope | Y-intercept | |
| Oceanic Events ($2.4 < M_L < 4.8$) | 0.031 .005 | -3.30 |
| Continental Events ($2.4 \; M_L \; 5.3$) | 0.093 .011 | -16.47 |

| Seismic Moment versus Power Level | | |
|---|---|---|
| Slope | Y-intercept | |
| Moderate Events ($10^{13} \; M_o \; 10^{17}$) | 0.025 .018 | 9.26 |

significance level of the regression analysis was well within the 95% confidence limit. events have a greater travel path within the strongly attenuating continental crust before exiting the seafloor-ocean interface and refracting into the SOFAR wave-guide than do oceanic earthquakes. Furthermore, in some cases the epicenter of the oceanic earthquakes are further down-slope along the continental margin and are within the sound channel itself. These two factors have been shown by several authors to play a major role, during conversion from P- to T-, of increasing the amplitude and duration of T-waves (i.e., Wadati and Inouye, 1953; Cansi and Bethoux, 1985). Another factor that may contribute to the observed source power level discrepancy between oceanic and continental events is different focal mechanisms. Although the exact mechanics are not clear, the difference in radiation pattern between a strike-slip (oceanic) and reverse (continental) fault mechanism could explain the disparity in the amount of energy radiated into the sound channel by these earthquakes. Earthquake radiation patterns could alter the efficiency of seismo-acoustic energy transfer from the crust to the sound channel. Also, different power levels for oceanic and continental events suggest that the detection threshold for the seismic events observed with hydrophone arrays may be less than $M_L$=2.4. Higher acoustic energy for oceanic events suggests that they are more likely to be detected. Many earthquakes were detected by the hydrophone arrays that were not listed by the land-based network, probably because they were oceanic in origin and too small to be detected on land.

An empirical relation of seismic moment and acoustic source power level is shown in Figure 2.17. The seismic moments listed in Table 2.1 were all taken from the NEIC (PDE) monthly listings. The indicator variable regression analysis of the seismic moment versus power level again showed, to a 95% confidence limit, that the three largest events ($M_o \geq 10^{18}$ N-m) should be treated statistically as an independent data set. However, because of the relatively few number (14) of earthquakes with calculated seismic moments

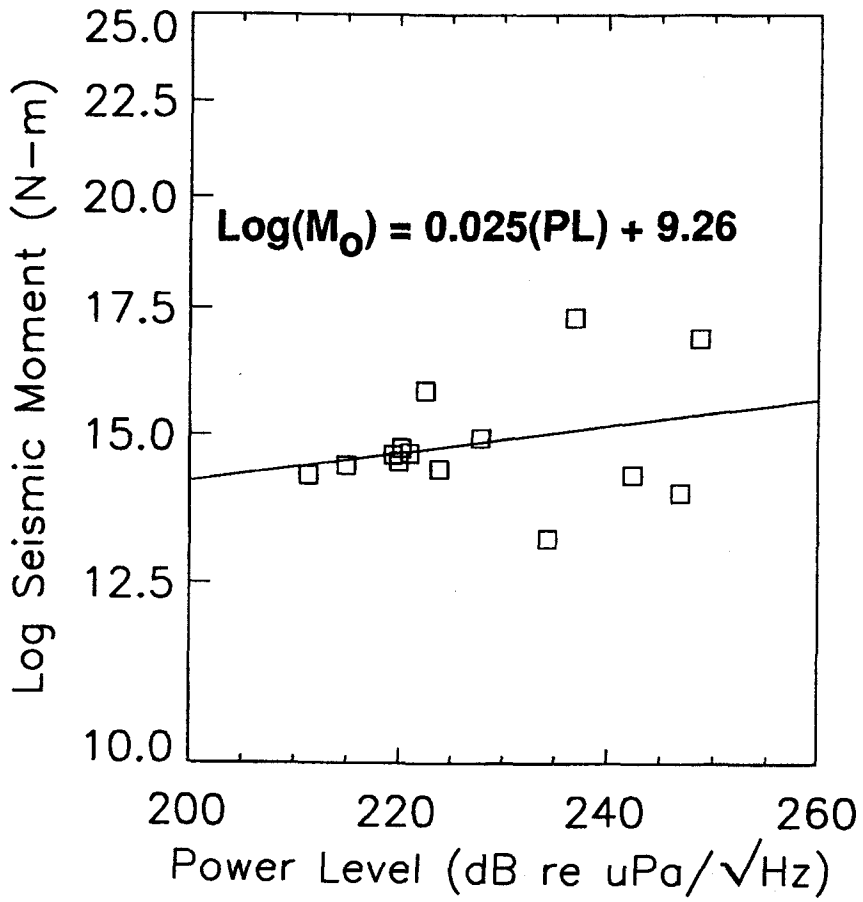


Figure 2.17. Empirical relation of seismic moment to source power level. Seismic moment data are listed in Table 2.1 and the results of the analyses are summarized in Table 2.3. Indicator regression analyses showed, to a 95% confidence interval, that the three largest events should again be treated statistically independent of the smaller events, so just the $M_o < 10^{18}$ events are considered here. However, since there are a relatively low number of earthquakes with moments below $10^{18}$ N-m, the difference between oceanic and continental earthquakes is not resolvable and regression was performed treating the events as a single group. As with the magnitude to power level relationship, seismic moment appears to scale linearly with an earthquake's acoustic power.

below $10^{18}$ N-m, the difference between oceanic and continental earthquakes was not resolvable. Thus, regression analyses were performed on the two different size clusters of earthquakes, and the results are summarized in Table 2.3. As with the magnitude to power level relationship, seismic moment scales linearly with acoustic power level. This scaling may arise from the fact that comparatively larger earthquakes have longer durations and consequently greater power levels. Additionally, the estimate of power level here uses spectral ranges typically much higher than seismic corner frequencies. Thus the scaling of coustic power level may reflect the increase in energy release of an earthquake, even at frequencies beyond the corner, as the size of the earthquake increases. Although this may only be applicable for events with corner frequencies within the 5 - 30 Hz acoustic spectral range since high frequency components of all earthquakes should theoretically have the same displacement amplitude.

## 2.5 Summary

The analysis of hydrophone array records from the April 1992 Cape Mendocino earthquake sequence yielded some notable results. The smallest earthquake detected by the hydrophone arrays (closest D = 3.5°) had a local magnitude of 2.4. The hydrophone records of the three largest shocks in the sequence ($M_L$=6.9,6.2,6.5) exhibited both T-waves and lithospheric phases from these events. Low-pass filtering (2 Hz) of the lithospheric phases yielded a clear P-wave arrival for epicentral distances of < 10°, but no apparent S-wave. The lack of a clear S-wave arrival may reflect limitations in the hydrophone sensitivity in detecting non-vertical ground motion. A seafloor cable-break was detected immediately after the second M > 6 aftershock, possibly the result of a submarine slide. The T-wave records of the second large aftershock showed no clear anomalous signal attributable to a

marine slide; however, the hydrophone records of the direct lithospheric phase showed a relatively high-amplitude and high-frequency arrival compared to the two previous large events, consistent with land-based seismic records. The seismic amplitude and frequency information were used by others to estimate rupture direction (Velasco et al.,1994). The rupture direction was shown to be toward the location of the cable break, possibly initiating the slide event.

Model estimates of transmission loss along T-wave travel paths indicate that loss is typically 10-20 dB (in the observed frequency range) for the most distant phones. Transmission loss can be as large as 50-70 dB for acoustic ray paths that cut across the continental margin, mostly due to bathymetric obstruction of the T-wave energy. The amount of acoustic energy each earthquake released into the ocean at the seafloor-water interface was estimated by applying the transmission loss and hydrophone instrument response to the recorded T-wave signals. This acoustic energy-release estimate, referred to in this study as the source power level, was calculated for 41 events with magnitudes over a recorded range of $2.4 < M_L < 6.9$. Seismic moment estimates were available for 17 of these events through the N.E.I.S. Once source power level spectra were obtained for each earthquake, the acoustic spectra were converted from pressure to displacement and compared to their seismic ground-displacement spectra. Unlike the seismic spectra, the acoustic displacement curves showed no indication of a corner frequency. The lack of an acoustic corner frequency makes it difficult to directly estimate the seismic size of an earthquake from its T-wave record. Therefore it is necessary to use empirical analyses in relating source level to seismic moment and magnitude to quantitatively derive earthquake size estimates.

The results of indicator variable regression analysis of the seismic magnitude and acoustic power level suggest the three largest earthquakes ($M_L > 6$) should not be modeled

with the rest of the data set, and the difference between the continental and oceanic earthquakes (excluding the three largest events) is significant. The difference in power level between the oceanic and continental earthquakes most likely results from a difference in the seismic propagation path from the earthquake's hypocenter to the sound channel. Seismic waves from continental events have a longer travel path within strongly attenuating continental crust, and oceanic earthquakes occur further downslope along the continental margin, possibly even within the sound channel. In another comparison, the indicator variable regression analysis of seismic moment and acoustic power level again suggests that the three largest events ($M_0 \geq 10^{18}$ N-m) should be considered separately from the rest of the events. However, because of the small number (17) of earthquakes with calculated seismic moments, the difference between continental and oceanic earthquakes was not resolvable. As with the magnitude to power level relationship, the seismic moment scales linearly with power level for events less than $10^{18}$ N-m. The observed scaling probably reflects the increased duration and power release expected as earthquake magnitude and moment increase, even at frequencies beyond the seismic corner frequencies. Regardless of the exact cause of the scaling between the acoustic and seismic energy estimates, these results indicate that acoustic measurements provide reasonable estimates of magnitude and moment for oceanic earthquakes that are not detected by land-based seismic networks.

## 2.6 Acknowledgements

The authors wish to thank Phil Slack and John Hildebrand for excellent constructive reviews. The authors also wish to thank TomYelin for providing the P-wave arrival time information from the Washington-Oregon Regional Seismograph Network (U. of W. and U.S.G.S.). Martha Winsor ministered expert statistical support in deciphering indicator variable regression. Hardware and software assistance were furnished by Eddie Radford

and Tai-Kwan Lau, and graphics production by Julia Getsiv. This article was reprinted with the kind permission of Kluwer Academic Publishers. Support for this work was provided by NOAA's VENTS Research Program, PMEL contribution #1641 .

## 2.7 References

Ben-Menahem, A. and M.N. Toksoz. 1963. Source-Mechanism from spectra of long-period seismic surface waves, 3: The Alaska earthquake of July 10, 1958. *Bull. Seism. Soc. Am.*, 53:905-919.

Brazee, R.J. 1965. A study of T-phases in the Aleutian earthquake series of March and April 1957. *Earthquake Notes*, 36:9-14.

Brocher, T.M. 1983. T-phases from an earthquake swarm on the Mid-Atlantic Ridge at 31.6°N. *Mar. Geophys. Res.*, 6:39-49.

Cansi, Y. and N. Bethoux. 1985. T-waves with long inland paths: Synthetic seismograms. *J. Geophys. Res.*, 90:5459-5465.

Dengler, L., G. Carver, and R. McPherson. 1992. Sources of north coast seismicity. *Calif. Geol.*, 45:40-53.

Dziewonski, A.M., G. Ekstrom, M.P. Salganik. 1993. Centroid-moment tensor solutions for April - June 1992. *Phys. Earth Planet. Inter.*, 77:151-163.

Eaton, J.P.. 1977. Frequency response of the U.S.G.S. short period telemetered seismic system and its suitability for network studies of local earthquakes. *Geol. Surv. Open-File Rep.*, 77-844, 1-45.

Fox, C.G., R.P Dziak, H. Matsumoto, and A.E. Schreiner. 1994. Potential for monitoring low-level seismicity on the Juan de Fuca Ridge using fixed hydrophone arrays. *Mar. Tech. Soc.*, 27:22-30.

Fox, C.G., W.E. Radford, R.P. Dziak, T-K Lau, H. Matsumoto, and A.E. Schreiner. 1995. Acoustic detection of a seafloor spreading episode on the Juan de Fuca Ridge using military hydrophone arrays. Geophys. Res. Lett., 22:131-134.

Gibowicz, S.J., J.H. Latter, and G.K. Sutton. 1974. Earthquake swarm associated with a volcanic eruption, Curacoa Reef area, northern Tonga, July 1973. *Ann. Geofis.*, 27:443-475.

Gupta, I.N. 1964. Discussion of "Source-mechanism from Spectsa of long-period seismic surface waves, 3: The Alaska earthquake of July 19, 1958", by A. Ben-Menahem and M.N. Toksoz. *Bull. Seism. Soc. Am.*, 54:2085-2086.

Hiyoshi, Y., D.A. Walker, C.S. McCreery. 1992. T-phase data and regional tsunamigenesis in Japan. *Bull. Seism. Soc. Am.*, 82:2213-2223.

Holmes, E.S., E.C. Miller, and R.H. Stephens 1990. A PC-based acoustic model operating system. IEEE *Oceans '90*, 227-231.

Johnson, R.H., J. Northrop, and R. Eppley. 1963. Sources of Pacific T-phases. *J. Geophys. Res.*, 68:4251-4260.

Johnson R.H. and J. Northrop 1966. A comparison of earthquake magnitude with T-phase strength. *Bull. Seism. Soc. Am.*, 56:119-124.

Johnson, R.H. 1970. Estimating rupture length from T-waves. In Tsunamis in the Pacific Ocean, P*roc. of the International Symposium on Tsunamis and Tsunami Research*, ed. W.M. Adams, 253-259, East West Center Press, Honolulu, HI.

Kanamori, H, and M. Kikuchi. 1993. The 1992 Nicaragua earthquake: A Slow tsunami earthquake associated with Subducted Sediments. *Nature*. 361:714-716.

Linehan, D. 1940. Earthquakes in the West Indian Region. *Trans. Am. Geophys. Union*, 229-232.

Naval Oceanographic Office, System Integration Division. 1991. Software requirements and specifications for the Parabolic Equation model, OAML-SRS-22C, Stennis Space Center, Mississippi 39522-5001, March.

Northrop, J., M. Blaik, and I. Tolstoy 1960. Spectrum analysis of T-phases from the Agadir earthquake, February 29, 1960, 23h 40m 12s GCT, 30°N, 9°W (USGCS). *J. Geophys. Res.*, 65:4223-4224.

Okal, E.A., and J. Talandier. 1986. T-wave duration, magnitudes, and seismic moment of an earthquake: Application to tsunami warning. *J. Phys. Earth*, 34:19-42.

Oppenheimer, D., G. Beroza, G. Carver, L. Dengler, J. Eaton, L. Gee, F. Gonzalez, A. Jayko, W.H. Li, M. Lisowski, M. Magee, G. Marshall, M. Murray, R. McPherson, B. Romanowicz, K. Satake, R. Simpson, P. Somerville, R. Stein, D. Valentine. 1993. The Cape Mendocino, California earthquake sequence of April, 1992: Subduction at the Triple Junction. *Science*, 261:433-438.

Richter, C.F. 1949. *Seismicity and structure of the Pacific Region of North America.* Proc. 7th Pacific Sci. Congr., 2, pp 671.

Riddihough, R. 1984. Recent movements of the Juan de Fuca plate system. *J. Geophys. Res.*, 89:6980-6994.

Silver, E.A. 1971. Tectonics of the Mendocino Triple Junction. *Geol. Soc. Am. Bull.*, 82:2965-2978.

Stoddard, P.R. 1987. A kinematic model for the evolution of the Gorda plate. *J. Geophys. Res.*, 92:11524-11532.

Tappert, F.D. and A.A. Hardin. 1977. The Parabolic Approximation Method. In *Wave Propagation and Underwater Acoustics*, J.B. Keller and J.S. Papadakis eds., Lecture Notes in Physics, Springer-Verlag, Heidelberg, 70, 224pp.

Thatcher, W., and T.C. Hanks. 1973. Source parameters of southern California earthquakes. *J. Geophys. Res.*, 78:8547-8576.

Tolstoy, I., and M. Ewing (1950). The T-phase of shallow-focus earthquakes. *Bull. Seism. Soc. Am.*, 40:25-51.

Tréhú, A.M., I. Asudeh, T.M. Brocher, J. Luetgert, W.D. Mooney, J.L. Nabelek, and Y. Nakamura. 1994. Crustal Structure of the Cascadia Forearc. *Science*, 266:237-243.

Velasco, A.A., C.J. Ammon, and T. Lay. 1994.. Recent Large Earthquakes near Cape Mendocino and in the Gorda Plate: Broadband Source Time Functions, Fault Orientations, and Rupture Complexities. *J. Geophys. Res.*, 99:711-728.

Wadati, K. and W. Inouye. 1953. On the T-phase of Seismic waves observed in Japan. *Proc. Japan Acad.*, 29, 47-54.

Walker, D.A., C.S. McCreery, and Y. Hiyoshi. 1992. T-phase Spectra, Seismic Moments, and Tsunamigenesis. *Bull. Seism. Soc. Am.*, 82:1275-1305.

Walter, S.R. 1986. Intermediate-Focus Earthquaks Associated with Gorda Plate Subduction in Northern California. *Bull Seism. Soc. Am.*, 76:583-588.

Wilde, P, T.E. Chase, M.L. Holmes, W.R. Normark, J.A. Thomas, D.S. McCulloch, and L.D. Kulm. 1978. Oceanographic Data off Northern California-Southern Oregon 40° to 43° North Including the Gorda Deep Sea Fan. Lawrence Berkeley Laboratory, Pub. 251, University of California, Berkeley.

Wilson, D.S. (1989). Deformation of the So-called Gorda Plate. *J. Geophys. Res.*, 94:3065-3075.

# Chapter 3

## Detection of and Response to a Probable Volcanogenic T-wave Event Swarm on the Western Blanco Transform Fault Zone

Robert P. Dziak
Department of Geosciences
Oregon State University
Corvallis, OR 97331

Christopher G. Fox, Robert W. Embley, John E. Lupton
National Oceanic and Atmospheric Administration,
Pacific Marine Environmental Laboratory
Hatfield Marine Science Center
Newport, OR 97365

Greg C. Johnson
National Oceanic and Atmospheric Administration,
Pacific Marine Environmental Laboratory
7600 Sand Point Way NE
Seattle, WA 98115

William W. Chadwick
Cooperative Institute for Marine Resources Studies,
Oregon State University
Hatfield Marine Science Center
Newport, OR 97365

Randolf A. Koski
United States Geological Survey
345 Middlefield Rd
Menlo Park, CA 94025

*Geophysical Research Letters*
American Geophysical Union, Washington, D.C.
April 15, 1996, p 873-876

## 3.1 Abstract

The East Blanco Depression (EBD), a pull-apart basin within the western Blanco Transform Fault Zone (BTFZ), was the site of an intense earthquake swarm that began at 1317 GMT on January 9, 1994. The swarm's T-waves were detected by the U.S. Navy's SOSUS hydrophone arrays and analyzed by the NOAA T-phase Project. Although tectonically generated earthquakes occur frequently along the BTFZ, this swarm was unusual in that it was preceded and accompanied by periodic, low-frequency, long-duration acoustic signals, that originated from near the swarm epicenters. These tremor-like signals were very similar in character to acoustic energy produced by the documented shallow-submarine eruption near Socorro Island, a seamount several hundred km west of Baja California, Mexico. The 69 earthquakes and 400 tremor-like events at the EBD occurred sporadically, with two periods of peak activity occurring between January 5-16 and 27-31. The swarm-like character of the earthquakes and the similarity of the tremor activity to the Socorro eruption, indicated that the EBD was undergoing an intrusion or eruption episode.

On January 27, the NOAA ship *Discoverer* conducted six CTD/rosette casts at the site. Water samples from two of the stations yielded anomalous $^{3}He$ concentrations, with maxima at ~2800 m depth over the main basin. During the June 1994 northeast Pacific cruise of the R/V *Atlantis II*, two camera tows within the basin yielded evidence of pillow-lava volcanism and hydrothermal deposits, but no conclusive evidence of a recent seafloor eruption. In September 1994, deployments of the U.S. Navy's Advanced Tethered Vehicle (ATV) from the R/V *Laney Chouest* resulted in the discovery of an active hydrothermal mound on the flanks of a pillow-lava volcano. The hydrothermal mound consists of Fe-rich hydrothermal precipitate and bacterial mats. Temperatures to

60°C were measured 30 cm below the surface. This is the first discovery of active hydrothermal vents along an oceanic fracture zone. Although no conclusive evidence of volcanic activity associated with the T-wave event swarm was found during these response efforts, the EBD has been the site of recent seafloor eruptions.

## 3.2 Introduction

Tertiary (T-) waves are seismically generated acoustic waves that propagate over great distances in the oceanic sound channel. On August 29, 1991, the National Oceanic and Atmospheric Administration (NOAA) began continuously recording digital data from the Navy's fixed hydrophone array (SOSUS) systems in the northeast Pacific ocean (Fox et al., 1994). On June 22, 1993, NOAA installed a prototype system at the U.S. Naval Facility, Whidbey Island, Washington, to allow real-time acoustic monitoring of the northeast Pacific. Earthquake and volcanic tremor T-waves associated with the June/July 1993 magmatic-dike injection along the CoAxial Segment (Juan de Fuca Ridge) have been well documented using this system (Fox et al., 1995; Schreiner et al., 1995; Dziak et al., 1995). Unprecedented water column and geologic ground-truth information was provided through rapid response efforts to the CoAxial eruption site (Embley et al., 1995; Lupton et al., 1995; Baker et al., 1995; Massoth et al., 1995). On January 2, 1994, low-frequency periodic signals were detected from the western Blanco Transform Fault Zone. These tremor-like signals, later interpreted to be of volcanic origin, occurred over the next four weeks. On January 9, a large earthquake swarm began within the East Blanco Depression (Figure 3.1). This paper examines the spatial and temporal distribution of T-wave earthquakes and tremor-like signals observed during the episode at the EBD, the findings of three response efforts that surveyed the water column seafloor in the region,

Figure 3.1. National Oceanic and Atmospheric Administration bathymetry of the Blanco Transform Fault Zone (20 m contours). The circles show the estimated epicenters of the T-wave earthquake swarm. The 'X' denotes the event location centroid. Stars are the location of CTD cast sites near the EBD, with cast site "6" (anomalous $He^3/He^4$ profile) labelled. Also shown are the camera-tow (CAM) and ATV dive tracklines, and the locations of the pillow-lava mound, hydrothermal mounds, barite chimneys, and hornitos found during the collective response efforts. The bottom-left inset map shows structural interpretation map of the Blanco Transform Fault Zone (after Embley and Wilson, 1992). The pull-apart basins (depressions) are shaded, and strike-slip fault segments are labelled with opposing arrows. Bottom-right inset map shows sketch of the northeast Pacific plate boundaries with geographic location of the Blanco Transform Fault Zone and East Blanco Depression.

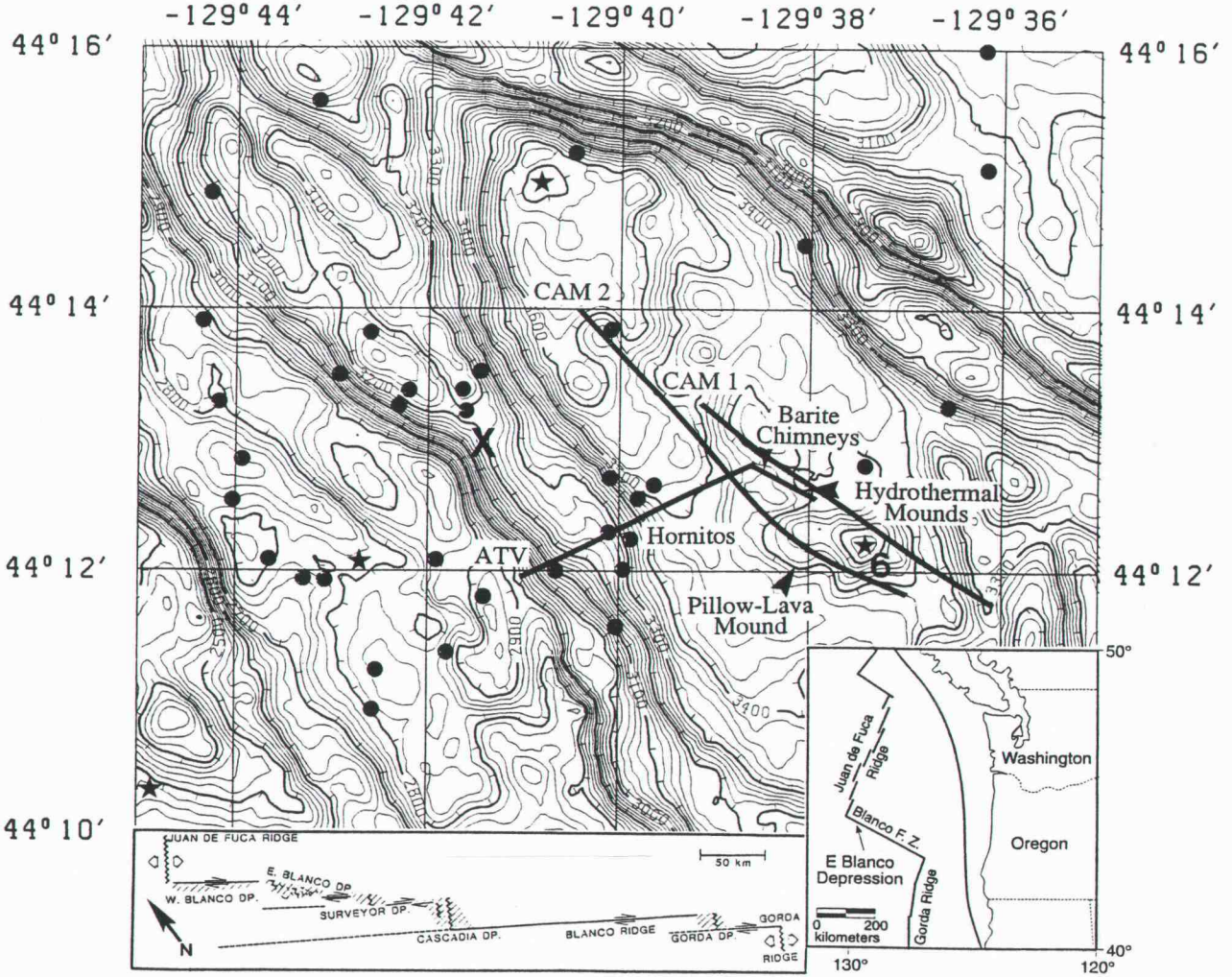
-129° 44′
-129° 42′
-129° 40′
-129° 38′
-129° 36′
44° 16′
44° 14′
44° 12′
44° 10′
CAM 2
CAM 1
Barite Chimneys
Hydrothermal Mounds
Hornitos
ATV
Pillow-Lava Mound
JUAN DE FUCA RIDGE
E. BLANCO DP.
W. BLANCO DP.
SURVEYOR DP.
CASCADIA DP.
BLANCO RIDGE
GORDA DP.
GORDA RIDGE
50 km
N
Juan de Fuca Ridge
Blanco F. Z.
E Blanco Depression
Gorda Ridge
Washington
Oregon
0 200 kilometers
50°
40°
130°
120°

Figure 3.1

and the implications for volcanic and hydrothermal processes along oceanic fracture zones.

The Blanco Transform Fault Zone (BTFZ), located in the Pacific Ocean off the coast of Oregon, is a right-lateral transform fault that links the moderate-spreading rate Juan de Fuca and Gorda Ridges (Figure 3.1). The BTFZ generated numerous large earthquakes ($m_b$ 6.1) that are tectonic in origin (Tobin and Sykes, 1968; Chandra, 1974; Dziak et al., 1991). Recently, with the advent of high-resolution multibeam sonar systems, detailed structural maps of the BTFZ have been produced (Embley et al., 1987; Embley and Wilson, 1992). Embley and Wilson (1992) divided the BTFZ into five major right-stepping strike-slip fault segments that are separated by deep extensional basins. These basins were interpreted to be the oceanic analog of pull-apart basins along continental divergent wrench-fault systems. The East Blanco Depression, a pull-apart basin in the western third of the BTFZ (Figure 3.1), exhibits extensional fabric oblique to the trend of the strike-slip fault segments (inset, Figure 3.1).

Evidence for volcanic activity within pull-apart basins along oceanic-transform faults is not uncommon, especially transforms along the fast-spreading East Pacific Rise. Fresh pillow-lava flows and young constructional volcanic mounds have been found along the Clipperton (Kastens et al., 1986), the Garret (Hekinian et al., 1992), and the Siqueiros (Perfit et al., 1993) transform fault zones. Although, the majority of recent lava flows along these transform faults are located within their pull-apart basins, the Siqueiros and Garret exhibit recent flows along their strike-slip fault segments as well. Evidence for recent extrusive volcanism within a continental pull-apart basin is rare, possibly due to the thick crust along continental strike-slip faults. A prime example of a pull-apart basin within a continental wrench fault that exhibits high-heat flow and Quaternary volcanic activity is the Salton Trough along the southern San Andreas - Imperial Fault

system (Newmark et al., 1988; Herzig and Elders, 1988). In the Salton Trough, early-Pleistocene diabase sills have intruded to within a few kilometers of the surface, and are thought to be the heat sources driving the hydrothermal system.

### 3.3 T-wave Event Detection

The East Blanco Depression earthquake swarm began at 1317 GMT on January 9, 1994 with a total of 61 earthquakes occurring over a 3-day period. The T-waves from this earthquake swarm were detected and located using formed-beams from the U.S. Navy's SOSUS hydrophone arrays within the NE Pacific Ocean (Figures 3.1 and 3.2). Formed-beams were used because they improve the signal/noise ratio of the T-wave event records (Fox et al., 1994). Since none of the events were detected by land-based seismic networks (U.S.G.S. Preliminary Determination of Epicenters Catalog, January 1994), and few were detected by SOSUS omni-directional hydrophones, the swarm earthquakes were all probably low magnitude events ($m_b < 4$). However, seismic activity associated with volcanic systems tends to occur at magnitudes below 4 (Klein et al., 1987; Einarsson, 1991). The earthquakes were located using a non-linear regression algorithm that minimizes error between observed and predicted arrival times (Dziak et al., 1995). It was difficult to select a consistent peak arrival phase for each earthquake, possibly due to either local bathymetric roughness, the volcanic nature of the events, a deep-crustal source for the earthquakes, or all of these factors. The inconsistent arrival picks resulted in the rather large scatter in event locations (Figure 3.1). For the purposes of a response effort, the centroid of the event cluster (44° 13.0' 4.2'N; 129° 41.3' 5.4'W) was taken to be the practical source of the earthquakes.

Figure 3.2. The time series and sonograms (frequency spectra) of (a) a beam that recorded the East Blanco Depression tremor-like events (January 7, 1994), (b) a beam that recorded EBD earthquakes (January 10, 1994), and (c) an omni-directional hydrophone record of volcanic tremor detected from the Socorro Island eruption (January 30, 1993). Vertical axis is time with ticks representing one minute intervals, total time shown is 66 minutes, and increases upward. Horizontal axis shows both amplitude (2.5 volts for beams and 5 volts for the hydrophone), and spectra range (0-50 Hz for beams, 0-64 Hz for hydrophones). Sonograms were estimated using successive one second time series windows. Both the tremor from Socorro and the proposed tremor from the EBD are emergent, low-frequency (<25 Hz), and have highly periodic arrival times. The EBD earthquakes tend to be impulsive, broad-band, and random in occurrence. Continuous energy in the 15-20 Hz band on all three records are Fin whale vocalizations. The ubiquitous broad-band clipped amplitude signals present in the beam records are electronic system noise.

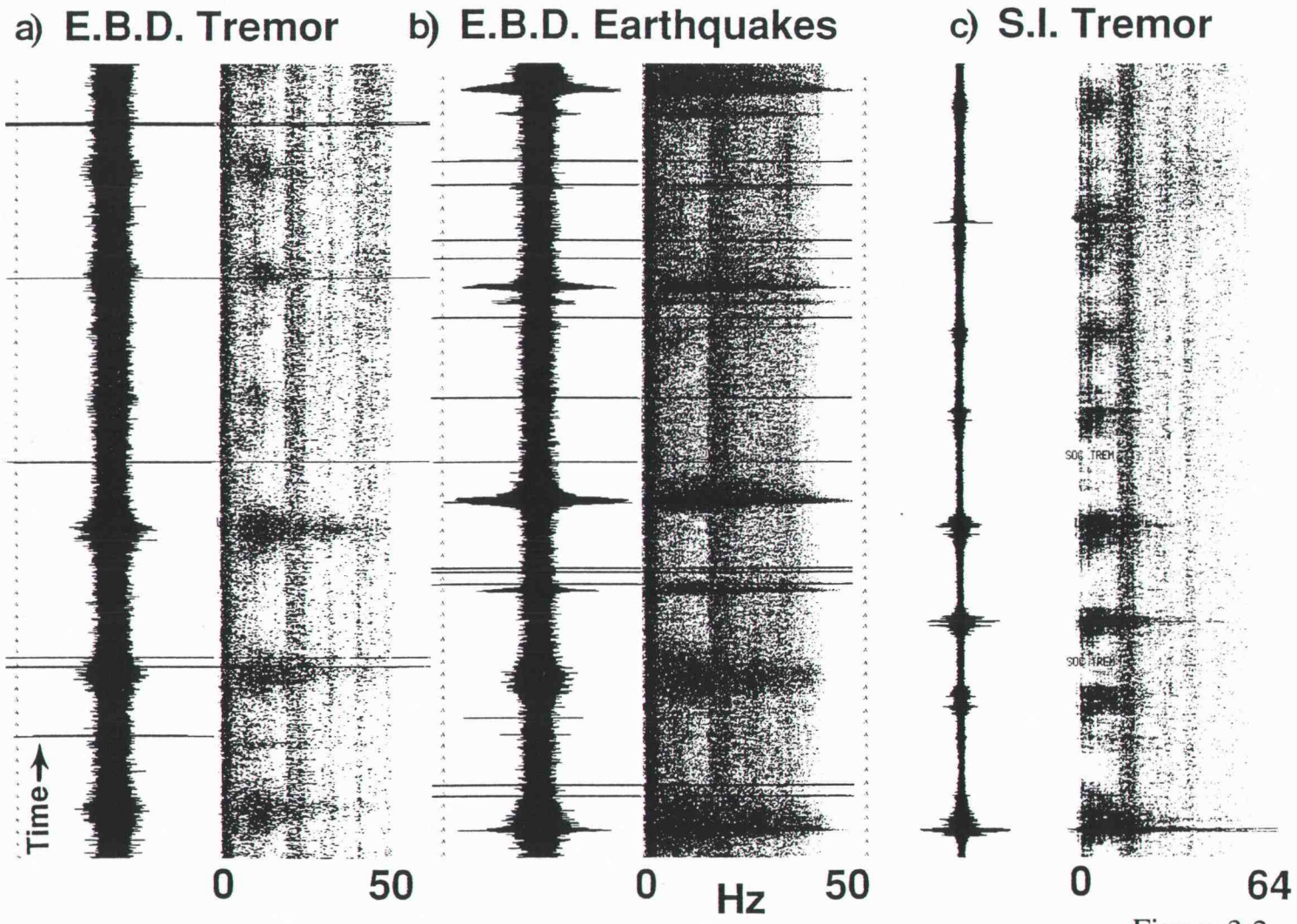


Figure 3.2

The earthquake swarm was preceded and accompanied by low-frequency long-duration acoustic signals that originated from near the swarm epicenters (Figure 3.2). The earthquakes differ significantly in acoustic character from the low frequency signals in that the earthquakes are short-duration, impulsive, and broad-band. The unidentified acoustic events are longer in duration, emergent, low-frequency (~ 2-20 Hz), and most importantly have arrival times that are periodic (every ~15-20 minutes). All periodic events had low source levels (< 190 dB) and were rarely detected on two hydrophone arrays making precise location impossible. However, since arrival time data from each hydrophone array can be used to estimate a bearing to a signal's source, the detection of the periodic events on two hydrophones arrays made it possible to estimate their approximate location. The bearings from two hydrophone arrays to the periodic events intersected at the East Blanco Depression. The error in bearing locations does not allow for any greater location accuracy other than to conclude that the periodic events occurred within the EBD.

The periodic tremor-like signals were interpreted as volcanogenic because of their similarity to T-wave arrivals, detected by the SOSUS hydrophone arrays, from an eruption offshore of Socorro Island (Figure 3.2). Socorro Island is located several hundred kilometers west of the Baja California coast (18R 45'N; 110R 57'W). Eruption activity began on January 16, 1993 when Mexican Naval authorities based on Socorro Island began feeling continuous seismic activity (Bulletin of the Global Volcanic Network (BGVN), 1993). Then on January 19, 1993, strong T-wave signals were detected from the area throughout the Pacific basin (Talandier and Okal, 1995). Ten days later, the crew of the sailing vessel Mystique observed a steam column and a 6000 $m^2$ mat of scoriaceous-lava blocks floating in ~140 m of water about 3 km offshore of Socorro Island (BGVN, 1993). In April 1993, the Mexican Navy performed a bathymetric survey

in the area and imaged a new (328 m deep) conical shaped vent extending westward from the island (Ignacio Galindo, Universidad de Colima, pers. com.). During the survey, steaming-lava blocks were observed rising to the sea surface. The Socorro Island T-wave signals were detected by the SOSUS hydrophone arrays when the activity began, and almost continuously throughout the following year. The Socorro T-wave tremor events were similar to the tremor-like East Blanco events in that both were long duration, low-frequency, and had very periodic arrival times. During the peak tremor activity from Socorro, T-wave signals would arrive roughly every 10 to 20 minutes.

Figure 3.3 shows a histogram of the T-wave earthquake and tremor time-frequency distribution. The tremor-like events initiated the activity at the EBD with 11 events on January 2. After a 2 day quiet period, tremor began again on January 5 and occurred discontinuously during the next eleven days. Peak tremor activity was observed on January 12 (64 events) and January 30 (57 events), with period of near quiescence from January 16 through 26. The earthquakes began on January 9, and intense earthquake activity lasted through January 12, with earthquakes occurring sporadically thereafter. A total of 69 earthquakes and 400 tremor events were detected during the entire month of seismo-acoustic activity, with earthquake and tremor activity peaking on different days. By comparison, the ridge-crest eruption observed at the CoAxial Segment generated very little tremor but nearly 700 T-wave earthquakes during the 3 weeks of peak activity (Dziak et al., 1995). Both earthquake and tremor T-wave event rise times, from the EBD, were analyzed for indications that the source of the events shoaled over time. Neither showed clear evidence of a change in source depth during the intrusion episode.

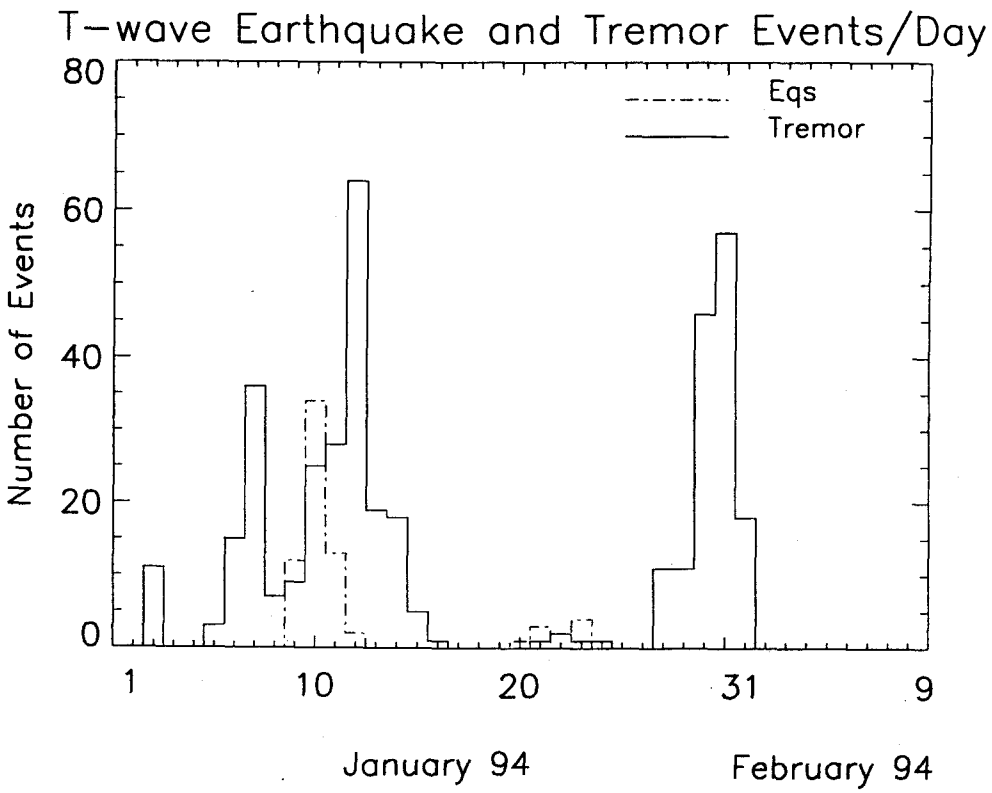


Figure 3.3. Histogram showing time and frequency distribution of the East Blanco Depression T-wave earthquake and tremor-like events. A brief period of tremor activity began on January 2, which was followed by nearly continuous tremor activity from January 5 through January 16. Peak tremor activity occurred on January 12 (64 events) and 30 (57 events), with a 5 day quiescent period separating the two main clusters of events. Earthquakes began on January 9 and lasted through January 12, with earthquakes occurring sporadically thereafter. A total of 69 earthquakes and 400 tremor events were detected during the month of seismo-acoustic activity.

### 3.4 Response Efforts

Since the East Blanco Depression T-wave activity was interpreted as potentially being volcanogenic, ground-truthing water-column and seafloor surveys were initiated. The NOAA ship Discoverer arrived on site on January 27, and six Conductivity-Temperature-Depth/rosette casts were taken around (four directly over) the EBD during the next few days. Two of the casts showed excesses in $^{3}He$ and temperature compared to background values. The highest water-column signals were detected at Cast 6, directly above the central bathymetric high within the basin (Figure 3.1). The $^{3}He$ profile for Cast 6 reached a maximum value of $\delta(^{3}He) = 83\%$ (defined in the figure caption 3.4) at a depth of 2800 m, ~800 m above the basin floor (Figure 3.4). This large excess in $^{3}He$, comparable to values observed directly over active black-smoker vent fields, was accompanied by a small (~0.005°C) temperature anomaly ($\Delta T$) at the same depth (Figure 3.4). The corresponding $^{3}He$/Heat ratio for the anomalous fluid residing at 2800 m depth is $8.7 \times 10^{-12}$ cc STP $cal^{-1}$, higher than any other hydrothermal $^{3}He$/heat ratios observed on the Juan de Fuca - Gorda Ridge system (Lupton et al., 1989; Lupton et al., 1995). The large rise height of the hydrothermal fluid (800 m above the bottom) might be interpreted as evidence for a single catastrophic release of hydrothermal fluid resulting from magma injection into the shallow crust of the EBD. However, the hydrothermal layer detected in Cast 6 does not have the thickness or high-temperature anomaly associated with event plumes observed previously on the Juan de Fuca Ridge (Baker et al., 1987; Baker et al., 1995). Furthermore, the apparent large rise height of the hydrothermal plume in the EBD can be attributed to the low density gradient in the water column below the basin sill depth which allows plumes to ascend more easily (Figure 3.4). Thus the water-column anomalies in $^{3}He$ and temperature detected in January, 1994 are probably due to a long

Figure 3.4. Profiles of $^3He/^4He$ ratio, temperature anomaly DT, and potential density $s_3$ versus depth for Cast 6. The largest $^3He$ anomaly occurs at ~2800 m depth, which corresponds to the sill depth of the basin and is also the depth below which there is a marked decrease in the density gradient. The $^3He/^4He$ ratio is expressed as $\delta(^3He)\%$, which is defined as $\delta(^3He) = 100 * (R_{sample}/R_{air} - 1)$, where $R_{sample} = ^3He/^4He$ and $R_{air} = 1.39 \times 10^{-6}$ is the $^3He/^4He$ ratio in air. The temperature anomaly $\Delta T$ is calculated as the deviation of potential temperature from the background potential temperature vs. potential density relationship in the region. $\sigma_3$ is density corrected for adiabatic effects referenced to 3000 decibars pressure.

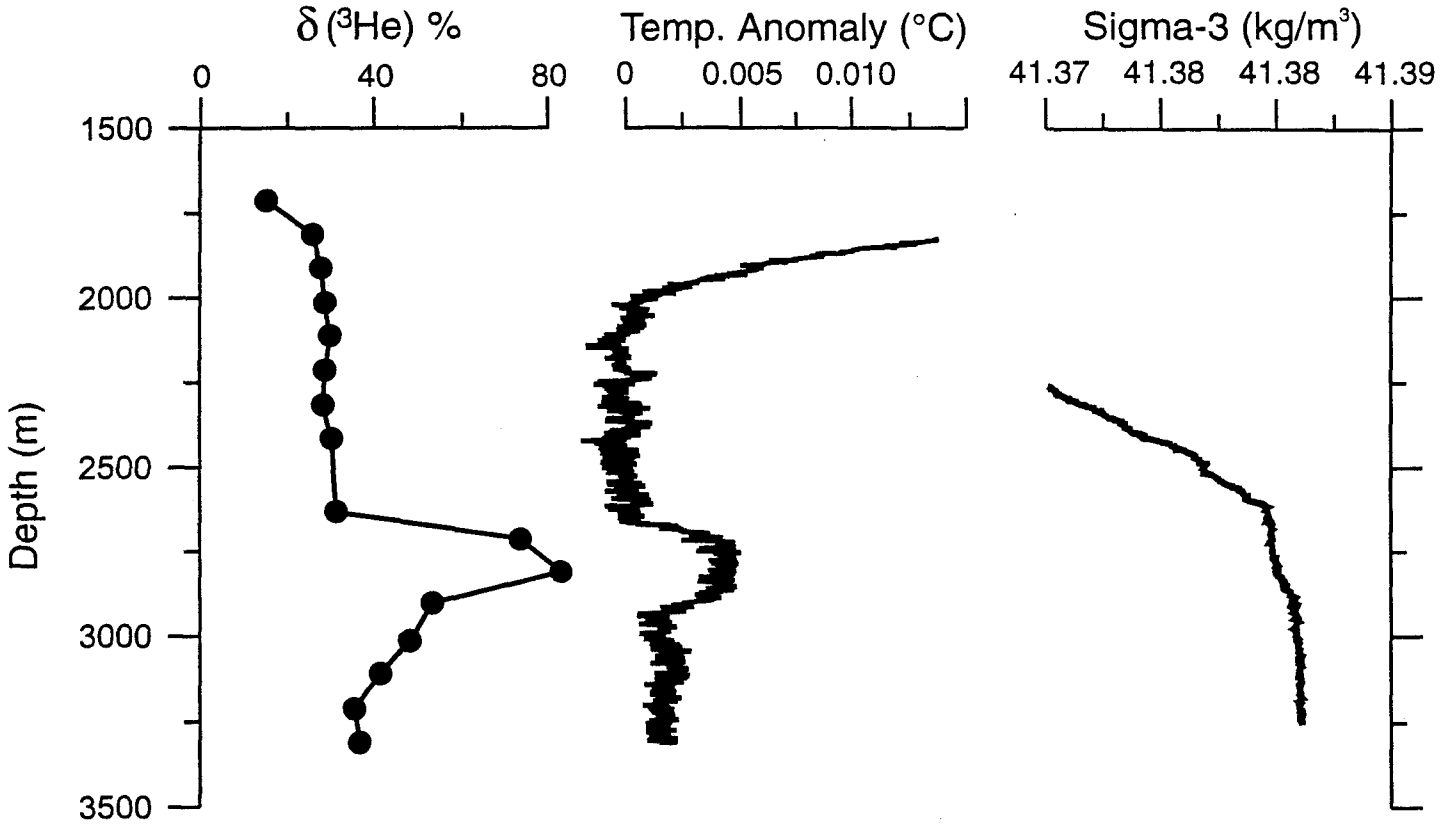
δ (3He) %
0
40
80
Temp. Anomaly (°C)
0
0.005
0.010
Sigma-3 (kg/m3)
41.37
41.38
41.38
41.39
Depth (m)
1500
2000
2500
3000
3500

Figure 3.4

-term accumulation of hydrothermal input rather than a single catastrophic release of fluid directly associated with the T-wave events.

On June 18 and 19, 1994, the R/V Atlantis II deployed the USGS camera system in two parallel tows from southeast to northwest across the basin (Figure 3.1). Both camera tows crossed the central-bathymetric high within the basin. Photographs and video from the tows showed the shallow area to be a constructional pillow-lava mound of a few square kilometers in area. None of the pillow lavas surveyed appeared to be recently erupted and are at least decades old. Additional bottom photographs along the northwest base of the volcanic edifice showed hydrothermal crusts, bacterial mats, and sediments that probably formed by low-temperature hydrothermal discharge.

A SeaBeam re-survey of the basin area was done in late August, 1994 by the Discoverer to look for any depth changes that might be associated with a volcanic eruption. The results of the survey were equivocal due to the low-quality of the navigation in the original survey, and the difficulty of resolving depth changes on steep slopes which are common in this area.

The last response effort to date occurred September 4 - 6, 1994, when a traverse was conducted across the floor of the EBD using the U.S. Navy's Advanced Tethered Vehicle (ATV). The ATV dive lasted 36 hours during which the constructional pillow-lava mound and the basin's western boundary scarp were surveyed (Figure 3.1). Small blocks and mounds of volcanic breccia cemented by barite, silica, and sulfide minerals were found in the vicinity of the target vent area (northwest base of the pillow-lava mound). The region between the volcanic mound and the western edge of the basin was almost exclusively constructional pillow-lava terrain. Along the western edge of the basin several small cones (hornitos), formed within the pillow-lava, were observed. Surveys up the western basin (east-facing) scarp showed it to be heavily sedimented.

Finally, an area of active hydrothermal mounds was found near the vent position indicated by the camera tow data, and about 1.5 km north of Cast 6 where the $^{3}He$ anomaly was detected (Figure 3.1). The mounds (~5 m high and ~15 m in diameter) are composed of unconsolidated Fe-oxide deposits and bacterial mats. Although no shimmering water was observed, temperature probe measurements up to 60°C were recorded within 30 cm of the mound surface. To our knowledge, this is the first known active hydrothermal site discovered within an oceanic transform fault system, albeit in an extensional regime along the transform.

## 3.5 Summary

The great depth of the East Blanco Depression (3650 m) suggests that it is an area of crustal thinning, as well as low magma supply. Although surface eruptions at this site might be rare, low-temperature, diffuse hydrothermal vent sites would be characteristic because of high heat flow. Toward this end, follow up work has been proposed to do detailed petrographic analysis of the existing basalt samples, comprehensive geologic mapping, heat-flow surveys of the hydrothermal mounds, and sampling and analysis of the vent fluids.

The major results of this study can be summarized as follows:

(1) The January 1994 East Blanco Depression T-wave swarm included earthquakes and tremor-like events and is interpreted as volcanogenic, possibly associated with intrusions into the shallow crust of the extensional basin.

(2) Although there is as of yet no evidence of extrusion with this T-wave swarm, the EBD has been the site of volcanism in the recent geologic past (100 yrs?). Volcanic activity in a pull-apart basin like the EBD probably occurs in a less organized, more diffuse zone than on a primary seafloor spreading center.

(3) An active hydrothermal center was found near the base of the major constructional pillow-lava edifice within the basin. Active hydrothermal mounds appear to consist of low-temperature precipitate and bacterial mats. The entire mound area is probably warm with temperature measurements up to 60RC ~30 cm inside individual mound surfaces. This is the first discovery of an active hydrothermal vent site along an oceanic fracture zone.

(4) The $^{3}$He and temperature anomalies observed at the 2800-m sill depth most likely resulted from a gradual accumulation of hydrothermal fluids within a density horizon over time rather than from a sudden catastrophic release of fluid directly associated with the T-wave swarm.

(5) The previous observations, in conjunction with the lack of a clear bathymetric change within the basin, suggests that either the eruptive site has not yet been located or the T-wave tremor signals and earthquakes were generated by magma movement at depth.

### 3.6 Acknowledgements.

The authors wish to thank A. Schreiner for evaluation of the earthquake and tremor event rise times, L. Evans for collecting and processing the helium samples, K. McTaggart for collecting and processing CTD data, J. Getsiv for enthusiastic graphics production, V. Smith and S. Ross for excellent at sea support, and H. Chezar for providing excellent support for the U.S.G.S camera system onboard the AII. Also, the authors owe a great debt of gratitude to the officers and crew of the ships *Laney Chouest*, *Discoverer*, *Atlantis II*, and the Deep Submergence Unit/Advanced Tethered Vehicle for expertise at sea without which this study could not have been conducted. This paper was reprinted with the kind permission of the American Geophysical Union. Support for this

work was provided by NOAA's VENTS Program, and the NOAA Undersea Research Program 1994 Laney Chouest Cruise Series. PMEL contribution No. 1688.

### 3.7 References

Baker, E.T., G.J Massoth, and R.A. Feely. 1987. Cataclysmic Hydrothermal Venting on the Juan de Fuca Ridge. *Nature*, 329:149-151.

Baker, E.T., G.J. Massoth, R.A. Feely, R.W. Embley, R.E. Thomson, and B.J. Burd. 1985. Hydrothermal Event Plumes from the CoAxial Seafloor Eruption Site, Juan de Fuca Ridge. *Geophys. Res. Lett.*, 22:147-150.

Bulletin of the Global Volcanism Network. 1993. No. 1, 9-12, January 31.

Chandra, U. 1974. Seismicity, Earthquake Mechanisms, and Tectonics along the Western Coast of North America from 42°N to 61°N. *Bull. Seism. Soc. Amer.*, 64:1529-1549.

Einarsson, P. 1991. Earthquakes and present-day tectonism in Iceland. *Tectonophys.*, 189:261-279.

Dziak, R.P., C.G. Fox, and R.W. Embley. 1991. Relationship Between the Seismicity and Geologic Structure of the Blanco Transform Fault Zone. *Mar. Geophys. Res.*, 13:203-208.

Dziak, R.P, C.G. Fox, and A.E. Schreiner. 1995. The June-July 1993 Seismo-acoustic Event at CoAxial Segment, Juan de Fuca Ridge: Evidence for a Lateral Dike Injection. *Geophys. Res. Lett.*, 22:135-138.

Embley, R.W., Kulm, L.D., Massoth, G., Abbott, D., Holmes, M. 1987. Morphology, Structure, and Resource Potential of the Blanco Transform Fault Zone. In *Geology and Resource Potential of the Continental Margin of Western North America and Adjacent Ocean Basins - Beaufort Sea to Baja, California*, 549-561, (ed. Scholl, D. W., Grantz, A., Yedder, J. G., Amer. Assoc. Petro. Geologists).

Embley, R.W., and D.S. Wilson. 1992. Morphology of the Blanco Transform Fault Zone-NE Pacific: Implications for its Tectonic Evolution. *Mar. Geophys. Res.*, 14, 25-45.

Embley, R.W., W.W. Chadwick, I.R. Jonasson, D.A. Butterfield, and E.T. Baker. 1995. Initial Results of the Rapid Response to the 1993 CoAxial Event: Relationships Between Hydrothermal and Volcanic Processes. *Geophys Res. Lett.*, 22, 143-146.

Fox, C.G., R.P. Dziak, H. Matsumoto, and A.E. Schreiner. 1994. Potential for Monitoring Low-Level Seismicity on the Juan de Fuca Ridge using Fixed Hydrophone Arrays. *Mar. Tech. Soc.*, 27:22-30.

Fox, C.G., W.E. Radford, R.P. Dziak, T-K Lau, H. Matsumoto, and A.E. Schreiner. 1995. Acoustic Detection of a Seafloor Spreading Episode on the Juan de Fuca Ridge Using Military Hydrophone Arrays. *Geophys. Res. Lett.*, 22:131-134..

Hekinian, R., D. Bideau, M. Cannat, J. Francheteau, and R. Hebert. 1992. Volcanic Activity and Crust-Mantle Exposure in the Ultrafast Garret Transform Fault near 13R28'S in the Pacific. *Earth and Planet. Sci. Lett.*, 108:259-275.

Herzig, C.T. and W.A. Elders. 1988. Nature and Significance of Igneous Rocks Cored in the State 2-14 Research Borehole: Salton Sea Scientific Drilling Project, California. *J. Geophys. Res.*, 93:13069-13080, 1988.

Kastens, K.A., W.B.F. Ryan, and P.J. Fox. 1986. Structural and Volcanic Expression of a Fast Slipping Ridge-Transform-Ridge-Plate Boundary: Sea Marc I and Photographic Surveys at the Clipperton Transform Fault. *J. Geophys. Res.*, 91:3469-3488.

Klein, F.W., R.Y. Koyanagi, J.S. Nakata, and W.R. Tanigawa. 1987. The seismicity of Kilauea's magma system. *U.S. Geol. Surv. Prof. Paper* 1350, 1019-1186.

Lupton, J.E., E.T. Baker, and G. Massoth. 1989. Variable $^{3}$He/heat Ratios in Submarine Hydrothermal Systems: Evidence from two Plumes over the Juan de Fuca Ridge. *Nature*, 337, 161-164, 1989.

Lupton, J.E., E.T. Baker, G.J. Massoth, R.E. Thomson, B.J. Burd, D.A. Butterfield, R.W. Embley, and G.A. Cannon. 1995. Variations in Water Column $^{3}$He/heat Ratios Associated with the 1993 CoAxial Event, Juan de Fuca Ridge. *Geophys. Res. Lett.*, 22:155-158.

Massoth, G.J., E.T. Baker, R.A. Feely, D.A. Butterfield, R.W. Embley, and G.A. Cannon. 1995. Variations of Manganese and Iron at the CoAxial Seafloor Eruption Site, Juan de Fuca Ridge. *Geophys. Res. Lett.*, 22:151-154.

Newmark, R.L., P.W. Kasameyer, and L.W. Younker. 1988. Shallow Drilling in the Salton Sea Region: The Thermal Anomaly. *J. Geophys. Res.*, 93, 13005-13023.

Perfit, M.R., D.J. Fornari, J.F. Casey, K.A. Kastens, W.I. Ridley, P.D. Kirk, M. Edwards, D. Desonie, J.R. Reynolds, R. Shuster, S. Paradis, C. Xia, D. Barlaz. 1993 Recent Volcanism in the Siqueiros Transform Fault: Eruption of Picritic and High-MgO Basalts and Implications for MORB Magma Genesis. *Earth and Planet. Sci. Lett.*, 109:4501-460.

Preliminary Determination of Epicenters. 1994. United States Geological Survey, National Earthquake Information Center, January.

Schreiner, A.E., C.G. Fox, and R.P. Dziak. 1995. Spectra and Magnitudes of T-waves from the 1993 Earthquake Swarm on the Juan de Fuca Ridge. *Geophys. Res. Lett.*, 22:139-142.

Talandier, J. and E.A. Okal. 1996. Monochromatic T-waves from Underwater Volcanoes in the Pacific Ocean: Ringing Witnesses to Degassing Processes?. *Bull. Seism. Soc. Am.*, in press.

Tobin, D.G. and L.R. Sykes. 1968. Seismicity and Tectonics of the Northeast Pacific Ocean. *J. Geophys. Res.*, 73:3821-3845.

# Chapter 4

## Internal Deformation of the Gorda Plate Observed Using Hydro-acoustic Techniques: Implications for Southern Cascadia Subduction Zone Tectonics

Christopher G. Fox

National Oceanic and Atmospheric Administration
Pacific Marine Environmental Laboratory
Oregon State University Hatfield Marine Science Center
Newport, OR 97365 U.S.A.

Robert P. Dziak

Cooperative Institute for Marine Resources Studies
National Oceanic and Atmospheric Administration, and
Department of Geosciences
Oregon State University Hatfield Marine Science Center
Newport, OR 97365 U.S.A.

Chris Goldfinger

College of Oceanic and Atmospheric Sciences
Oregon State University
Corvallis, OR 97331 U.S.A.

Submitted to *Geophysical Research Letters*
American Geophysical Union, Washington, D.C.
Spring 1997, 25 pages

## 4.1 Abstract

On August 29, 1991, the NOAA VENTS Program began monitoring the northeast Pacific ocean plate boundaries using continuously recorded data from the U.S. Navy's SOund SUrveillance System (SOSUS) hydrophone arrays. Routine detection and location of small (2.4<M<4.2) earthquakes revealed a NE-SW trending band of seismicity along the outer-rise region of the Gorda plate. This band of microearthquakes was active from the initiation of SOSUS recording in August 1991 through July 1992 at a rate of approximately 20 events per week. Since August 1992, the activity has effectively ceased. The microseismicity band appeared to follow along N-NE trending high-angle reverse faults that are reactivated spreading-fabric normal faults. It is proposed that the eventual termination of Gorda plate micro-earthquake activity is due to strain reduction in the mid-plate associated with the Cape Mendocino subduction zone earthquake sequence.

## 4.2 Introduction

The largest earthquakes recorded in historical time have occurred as a result of the thrusting of oceanic lithosphere beneath continental lithosphere along subduction zones. Strongly coupled subduction zones along Chile and Alaska have produced earthquakes with moment magnitudes $M_w > 9$, while weakly coupled subduction zones such as along the Marianas Arc produce events with $M_w < 8$ (Kanamori, 1977). The Cascadia subduction zone (CSZ), the subduction boundary between the North American and Gorda/Juan de Fuca plates along the coasts of California, Oregon, and Washington (Figure 4.1), has been an enigma due to its lack of large recorded earthquakes, although it shows characteristics of a strongly-coupled subduction zone (Heaton and Hartzell, 1987). The 1992 Cape Mendocino event ($M_w$=7.2) was the first large thrust earthquake recorded in historical time that probably occurred along the CSZ interplate interface (Oppenheimer et al., 1993). However,

Figure 4.1. Location map showing major plates and plate boundaries in the vicinity of the southern Cascadia Subduction Zone (CSZ). JdF is Juan de Fuca plate, NA is North American plate, BFZ is Blanco Fracture Zone, GR is Gorda Ridge, MFZ is Mendocino Fracture Zone, MTJ is Mendocino Triple Junction, SAF is the San Andreas Fault. CA and OR are California and Oregon, respectively. SAF, MTJ, and MFZ termini are dashed to illustrate the complexity of the region. Relative motion vectors between the North American and Juan de Fuca and Gorda plates are given with directions and rates shown (after Riddihough, 1984). The Gorda plate is separated from the larger Juan de Fuca plate by the extension of the Blanco Fracture Zone (dashed line). Hachured lines with NNE trend represent reactivated mid-Gorda plate reverse faults. Brackets in mid-Gorda plate illustrate location of 1991-1992 T-wave microseismicity band. The ~40 km long Cape Mendocino fault plane (Velasco et al., 1994) is shown along with the earthquake's slip vector (azimuth of 262±26°).

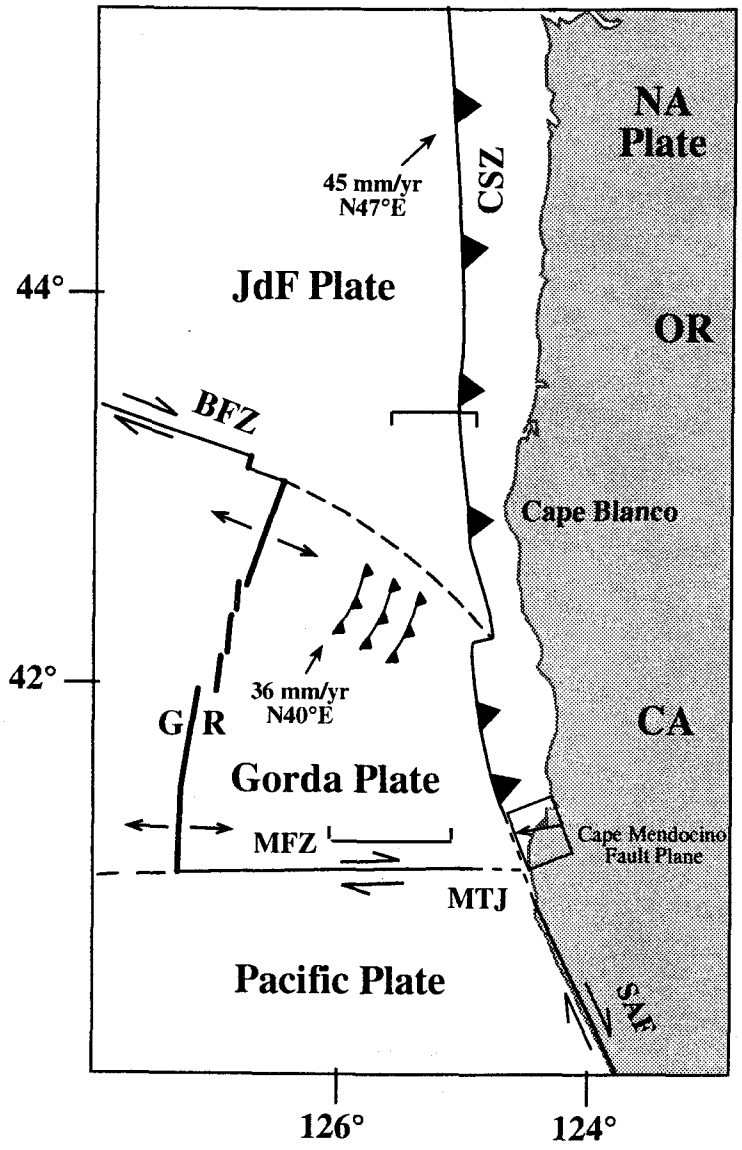
NA
Plate
45 mm/yr
N47°E
CSZ
44°
JdF Plate
OR
BFZ
Cape Blanco
42°
36 mm/yr
N40°E
G
R
CA
Gorda Plate
MFZ
Cape Mendocino
Fault Plane
MTJ
Pacific Plate
SAF
126°
124°

Figure 4.1

the proximity of the earthquake to the seismically active Mendocino Triple Junction further complicates the interpretation. Thus it is still not clear whether the CSZ plate interface is truly aseismic or if earthquakes are occurring below the detection threshold of regional seismic networks.

In 1991, the National Oceanic and Atmospheric Administration (NOAA) was granted access to the U.S. Navy's SOund SUrveillance System (SOSUS) in the northeast Pacific Ocean for use in monitoring the Juan de Fuca Ridge spreading center for low-level seismic activity. Although SOSUS is designed for tracking submarine activity in the open ocean, NOAA developed a parallel processing system to allow monitoring and localization of microseismicity along the seafloor spreading centers of the northeast Pacific (Fox et al., 1994). The system was successfully used to detect a volcanic dike injection along the Juan de Fuca Ridge in 1993 (Fox et al., 1995; Dziak et al., 1995) and to direct research vessels to the site of a volcanic eruption on the seafloor (Embley et al., 1995).

The method relies on the detection of hydro-acoustic waves (T-waves) that propagate within the oceanic water column and offers certain advantages over land-based systems. The presence of a layer of slow sound speed (sound channel) throughout much of the tropical and temperate ocean focuses seismo-acoustic energy entering the ocean into a limited wave guide. This wave guide exhibits quasi-cylindrical spreading, versus spherical spreading in the solid earth, which allows earthquakes as small as magnitude ~1.8 to be detected at ranges of several hundred kilometers (Fox et al., 1994). Also, epicenter location estimates are aided by the generally slower sound speeds (~1475m/s) and the availability of accurate sound speed models based on decades of oceanic measurements. The method has the advantage of detecting smaller events with greater location accuracy than land-based seismic systems, but is not capable of determining earthquake source parameters due to the complexity of the propagation pattern. The precise locations of the hydrophone arrays are

not for public distribution, but earthquake locations can be published. Continuous hydroacoustic seismic monitoring of the northeast Pacific continues as of this writing.

From the onset of SOSUS recording by NOAA on August 29, 1991, a band of low-level T-wave seismicity, trending N-NE, was detected in the Gorda plate offshore southern Oregon and northern California. The microseismicity band is parallel to N-NE trending high-angle reverse faults in the Gorda plate that are reactivated spreading-fabric normal faults. Recording of the band was preceded by three large strike-slip earthquakes that occurred within the Gorda plate on July 13 ($M_w$=6.8), August 16 ($M_w$=6.2), and August 17 ($M_w$=7.1) of 1991. The band terminated a few months after the April 25, 1992 Cape Mendocino earthquake ($M_w$=7.2) and its two large aftershocks ($M_w$=6.5 and 6.6) located offshore in the upper mantle of the Gorda plate.

The purpose of this paper is to present and discuss the distribution and temporal pattern of this T-wave microseismicity band detected within the mid-Gorda plate. Combining the microearthquake epicenters with analysis of available earthquake moment-tensor solutions from land-based seismometers (Dziewonski et al., 1992, 1993) and recently mapped Pliocene and younger active faults in the mid Gorda plate (Goldfinger, 1992), may provide insight into the state of stress within the Gorda plate and the coupling strength of the southern Cascadia forearc.

### 4.3 Gorda Plate Microseismicity

A band of low-level T-wave seismicity was detected in the Gorda plate offshore southern Oregon and northern California (Figure 4.2), from the onset of SOSUS recording on August 29, 1991. Since the Navy does not archive SOSUS data, it is not possible to recover data from earlier periods. The pattern of seismicity forms a NNE-SSW trending band, apparently extending under the continental slope in the north and to the Mendocino

Figure 4.2. Gorda plate T-wave earthquakes recorded from (a) beginning of hydrophone monitoring on August 29, 1991 through August 1, 1992, and (b) August 2, 1992 through January 4, 1996. Polygon highlights T-wave earthquakes shown in Figure 4.3 histogram, and illustrates the pronounced decrease in Gorda plate seismicity after mid 1992. Contours show bathymetry of region at 100 m intervals.

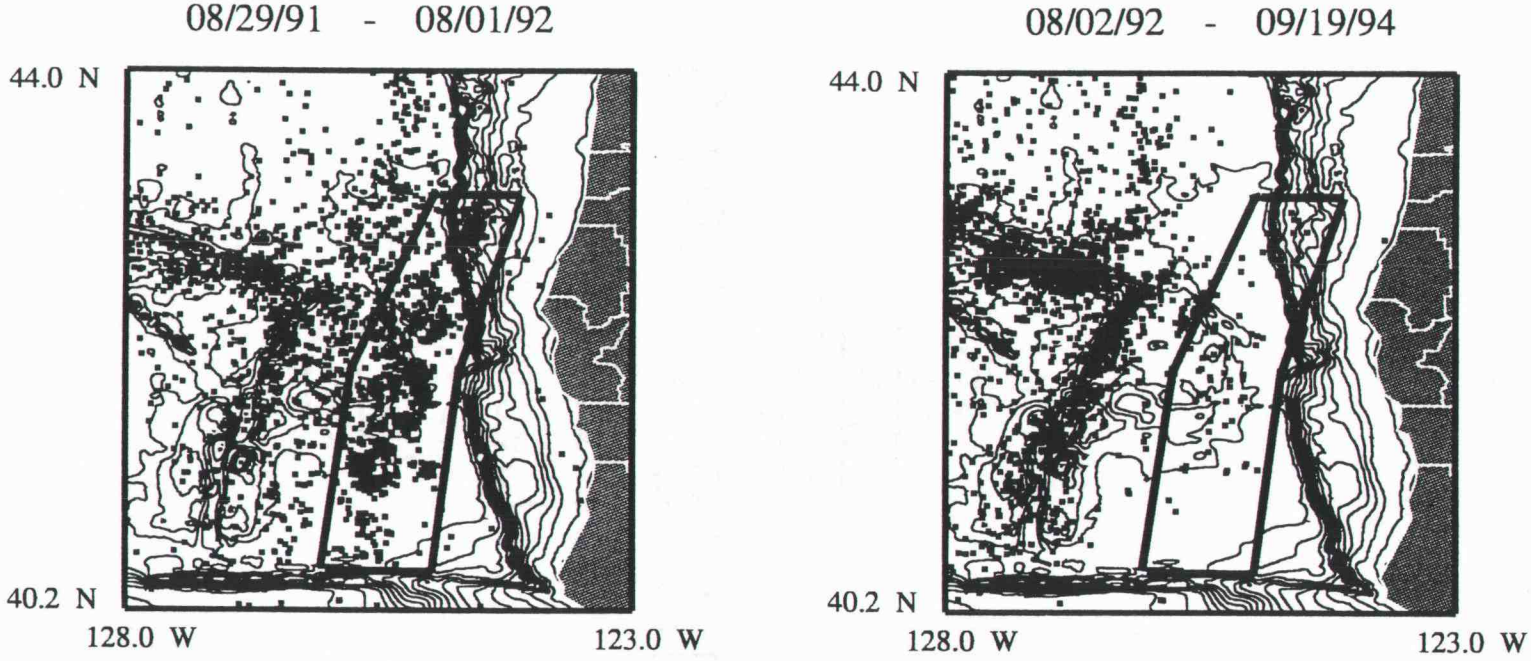
08/29/91 - 08/01/92
44.0 N
40.2 N
128.0 W
123.0 W
08/02/92 - 09/19/94
44.0 N
40.2 N
128.0 W
123.0 W

Figure 4.2

Fracture Zone in the south. Figure 4.2 summarizes the location time dependence of the T-wave events within the Gorda plate and Figure 4.3a-b shows a weekly count histogram and latitudinal distribution of the Gorda plate events occurring within the band. At the initiation of monitoring, the seismicity began at an intense rate of 80 events/week distributed along the entire Gorda plate and extending into the Juan de Fuca plate (40.5N to 43.8N) The seismicity then declined to < 10 events/week by November 1991. By December 1991 and early 1992, the seismicity once again increased (averaging > 20 events/week) and became concentrated along the center of the plate between 41°N and 43°N (Figure 4.3b). The seismicity maintained this higher level of activity until mid-1992, at which time the activity ceased and has not resumed since. There were no changes to the SOSUS recording system or processing methods at that time, and other areas of high seismic activity in the area (for example the Blanco Fracture Zone to the west) show no change in activity level at that time. Once the intensity of the Gorda plate T-wave earthquake activity began to increase again in December 1991, the only significant event to occur in the region was the April 1992 Cape Mendocino earthquake sequence. After the Cape Mendocino events, the T-wave seismicity decayed rapidly over the next two months, eventually ending by late July to early August 1992.

## 4.4 Gorda Plate and Mendocino Triple Junction Teleseismic Activity

During 1991, three large strike-slip earthquakes (Figure 4.4) occurred within the Gorda plate on July 13 ($M_w$=6.8), August 16 ($M_w$=6.2), and August 17 ($M_w$=7.1), and had focal depths of 11, 10, and 14 km, respectively (Dziewonski et al., 1992). All three earthquakes have moment-tensor solutions indicating high-angle (68°-86°) strike-slip faulting on either NE or NW striking fault planes (Table 4.1). Only the August 17 event exhibited a significant dip-slip component of ~30% reverse motion. Unfortunately,

Figure 4.3. Histogram of T-wave earthquakes per week from Gorda plate (top) and latitude variation of T-wave seismicity through time (bottom). Seismicity shown is from within polygon shown in figure 2a-b. The time of occurrence of the large (M>6) Gorda mid-plate events and the April 1992 Cape Mendocino earthquake are indicated on top diagram. There is a marked decrease in earthquake activity by July 1992, with seismicity essentially ceasing by August.

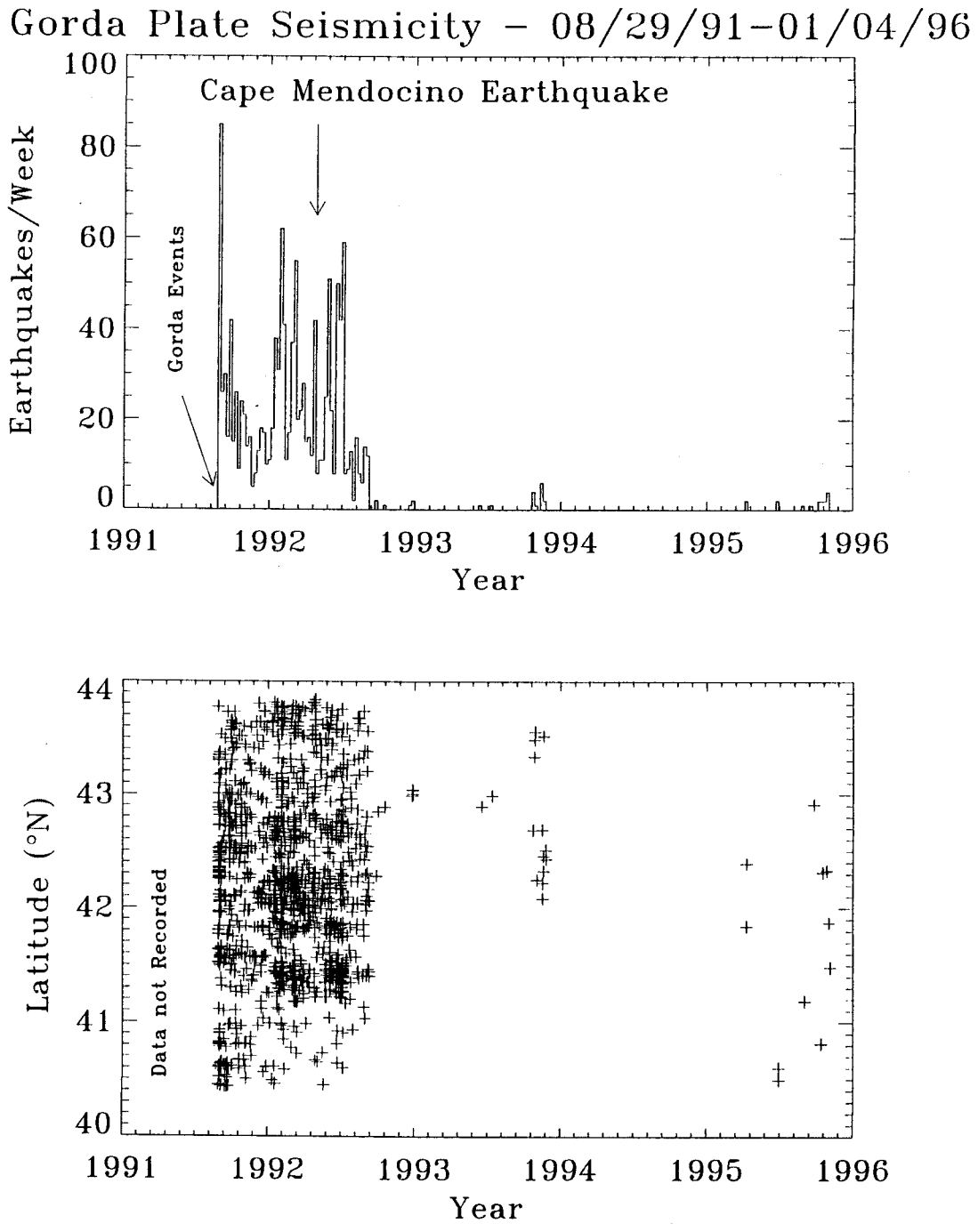
Gorda Plate Seismicity – 08/29/91–01/04/96
Cape Mendocino Earthquake
Gorda Events
Earthquakes/Week
100
80
60
40
20
0
1991
1992
1993
1994
1995
1996
Year
Data not Recorded
Latitude (°N)
44
43
42
41
40
1991
1992
1993
1994
1995
1996
Year

Figure 4.3

Figure 4.4. Upper left diagram shows bathymetry (100 m contour) of the Gorda plate, focal mechanisms of large earthquakes during the time period of interest, and location of coast. Brackets show approximate location of T-wave seismicity band. Box shows location of Gloria sidescan image shown at right. Mechanisms are lower-hemisphere equal area projections, with compressional quadrant shaded. Dots on each mechanism indicate location of P-axes. Earthquake source parameter information is listed in Table 4.1. Middle right diagram is Gloria sidescan mosaic showing the northeastern Gorda and southeastern Juan de Fuca plates. Overlays show bathymetric contours. Heavy line from A to B locates Gloria 2-channel seismic reflection profile (lower left image) trackline. West-vergent reverse faults in the northeastern Gorda plate are evident in the sidescan image.. Faults are parallel to spreading fabric, and are likely reactivated normal faults. Lower left image shows Gloria 2 channel unmigrated reflection profile showing west-vergent reverse faulting of the northeastern Gorda plate. Recent deformation indicated by uplift of uppermost reflectors indicating deformation of uppermost abyssal plain sediments. Basement involvement is likely since faults parallel magnetic lineations of the Gorda plate (Wilson, 1989).

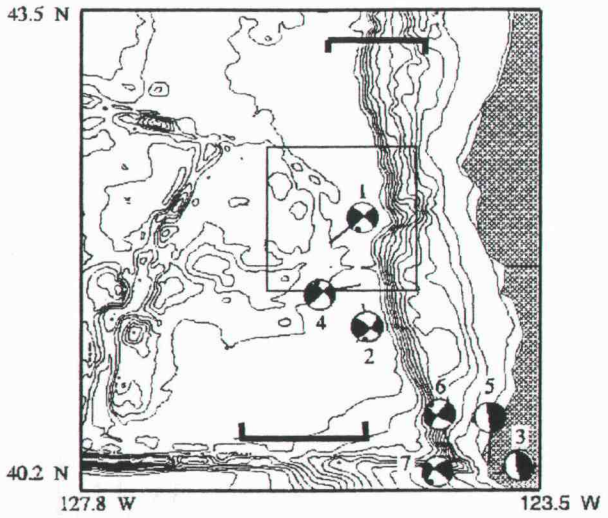
43.5 N
40.2 N
127.8 W
123.5 W
1
2
3
4
5
6
7

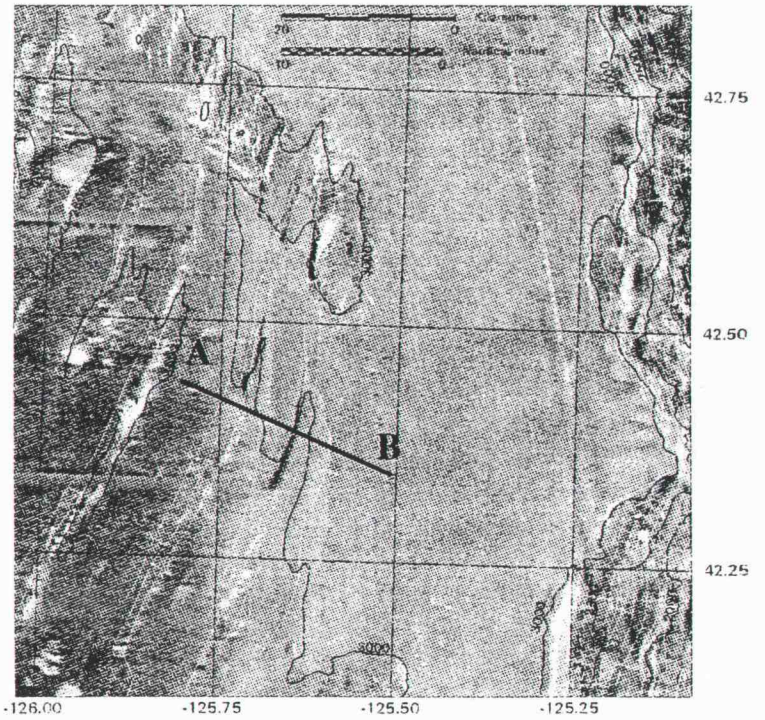
42.75
42.50
42.25
-126.00
-125.75
-125.50
-125.25
A
B

A B

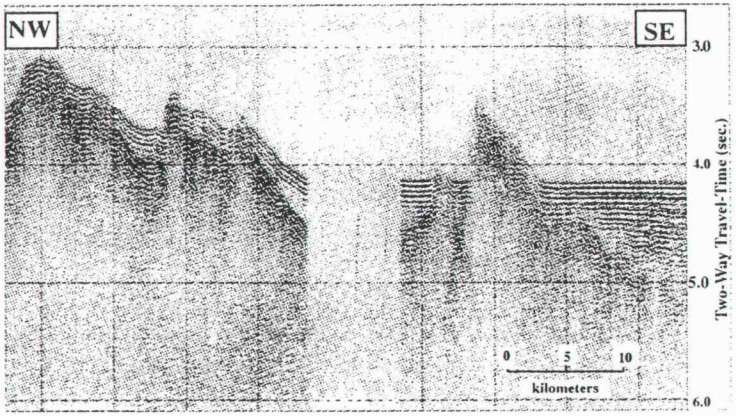
NW
SE
3.0
4.0
5.0
6.0
Two-Way Travel-Time (sec.)
0 5 10
kilometers

Figure 4.4

**Table 4.1: Earthquake Source Parameters †**

| Evt. | Date | Time UT | $M_w$ | Lat (°N) | Lon (°W) | Depth km | Strike (°) | Dip (°) | Rake (°) |
|---|---|---|---|---|---|---|---|---|---|
| 1 | 07/13/91 | 02:50:15 | 6.8 | 42.18 | 125.64 | 11 | 315 | 078 | -178 |
| 2 | 08/16/91 | 22:26:17 | 6.2 | 41.70 | 125.39 | 10 | 040 | 086 | 006 |
| 3 | 08/17/91 | 19:29:40 | 6.2 | 40.28 | 124.25 | 10 | 311 | 022 | 051 |
| 4 | 08/17/91 | 22:17:15 | 7.1 | 41.82 | 125.40 | 14 | 046 | 086 | 028 |
| 5 | 04/25/92 | 18:06:04 | 7.2 | 40.37 | 124.32 | 15 | 331 | 009 | 068 |
| 6 | 04/26/92 | 07:41:40 | 6.5 | 40.42 | 124.60 | 20 | 215 | 083 | 015 |
| 7 | 04/26/92 | 11:18:26 | 6.6 | 40.38 | 124.57 | 22 | 132 | 089 | 157 |

† Data from National Earthquake Information Center and Dziewonski et al. (1992, 1993)

hydrophone data are not available from the time these events occurred so that T-wave based locations for the micro-seismicity band and the large mid-plate earthquakes can not be directly compared. The July-August 1991 events are the largest intraplate earthquakes in the Gorda plate since a 1980 ($M_w$=7.3) strike-slip earthquake occurred in the continental margin offshore of Eureka, CA (Lay et al., 1982). Also on August 17, 1991, approximately two hours earlier than the Gorda event, a large ($M_w$=6.2) earthquake occurred within the area of the Mendocino Triple Junction (MTJ) near Honeydew, CA. The Honeydew event was interpreted by Velasco et al. (1994) as a fore-shock to the April 25, 1992 Cape Mendocino earthquake since its location and focal mechanism are very similar to the Cape Mendocino mainshock, and thus the events likely ruptured the same fault plane.

The April 25, 1992 Cape Mendocino earthquake ($M_w$=7.2) occurred near the MTJ and caused considerable damage to the towns of Ferndale, Fortuna, Petrolia, and Scotia, CA. (National Earthquake Information Center (NEIC), 1992). The focal mechanism of the event indicates predominantly thrust faulting (Dziewonski et al., 1993; Velasco et al., 1994). The Cape Mendocino earthquake is the largest historic earthquake in this region to have occurred on land, and may be the first recorded thrust earthquake within the Cascadia subduction zone (Dengler et al., 1992). Prior to this earthquake, there was no conclusive evidence in the 150-year historic record that such an event had occurred anywhere along the CSZ from Cape Mendocino to Vancouver Island. The Cape Mendocino event was followed on April 26 by two large aftershocks ($M_w$=6.5 and 6.6) located offshore in the upper mantle of the Gorda plate (Dziewonski et al, 1993; Oppenheimer et al., 1993). The occurrence of the two aftershocks suggests significant coupling of the stresses between the Gorda and North American plates and highlights the complexity of the fault interactions within the region (Velasco et al., 1994). Acoustically-derived locations for the Cape Mendocino events are very close to their seismic network epicenters (Dziak et al., 1997), so

for consistency with the mid-plate events, only the seismic locations are considered.

The 1991 mid-Gorda plate moment-tensor solutions, and the April 1992 Cape Mendocino aftershocks that occurred in the Gorda plate exhibit horizontal north-south P-axes ($\sigma_1$) and horizontal east-west T-axes ($\sigma_3$), a stress state that has been previously recognized in the Gorda plate (Wilson, 1986). The 1991 Honeydew and 1992 Cape Mendocino events both show vertical $\sigma_3$ and east-west $\sigma_1$, and are possibly subduction zone earthquakes, although they occur near the triple junction/collision zone.

## 4.5 Gorda Plate Active Faults

Recently, a map of Pliocene and younger faults was compiled of the continental margin off the Washington, Oregon, and northern California coasts using SeaBeam bathymetry, seismic reflection, and Gloria sidescan data (Goldfinger, 1992). The overlap region of these geophysical surveys covers the northern Gorda and southern Juan de Fuca plates from 42° - 46°N; 127° - 124°W, which provides fault structure information for two-thirds of the Gorda plate T-wave seismicity band. The location of the T-wave seismicity band correlates well with a series of mid-plate reverse faults (Figure 4.4). The reverse faults trend NE to NNE, and are likely reactivated spreading-fabric normal faults since they are parallel to the magnetic fabric. The reverse faults are mostly west-vergent, deform young sediment overlying the basement basalt, and have structural evidence for a component of right-lateral strike-slip motion. The reverse faults are reactivated structures, which might explain why the outer-rise T-wave seismicity band is not perfectly parallel to the margin. Also, the T-wave seismicity extends across the Blanco Fracture Zone and beneath the continental margin off southern Oregon. The Juan de Fuca plate T-wave seismicity may be a result of reactivation of the Juan de Fuca plate basement fabric since it has approximately the same trend as that of the Gorda plate basement fabric.

## 4.6 Discussion

Review of NEIC earthquake catalogues for the mid-Gorda plate showed that a total of two earthquakes occurred from November 1990 through June 1991, then during July-August 1991 when the M>6 earthquakes occurred, thirty-nine events were detected. The seismicity declined to three events in September 1991, and effectively ceased by October 1991. Since the NEIC Gorda plate earthquake locations are limited to M>3.5 events, the T-wave microseismicity band was not detected by the seismic networks. Although some of the T-wave events are no doubt aftershocks from the three large earthquakes that occurred in the Gorda plate in July and August of 1991, the majority of T-wave events do not occur in the proximity of the M>6 1991 earthquakes, and therefore represent a more general pattern of deformation within the Gorda plate. Further, all of the Gorda plate seismicity (T-wave band and M>6 events inclusive) are most likely related to regional deformation and fault reactivation in the mid-plate outer-rise, but this relationship could not be inferred based on the NEIC data alone.

The mid-Gorda plate reverse faults may be accommodating E-W shortening in the mid-Gorda plate. The orientation and style of motion of the faults do not seemingly coincide with NE-SW or NW-SE left-lateral strike-slip faulting in the upper slab, inferred from focal mechanism data from the M>6 1991 events. Thus it is necessary to attempt to reconcile the T-wave seismicity band, the mid-plate reverse faults, and the source parameter information.

The T-wave microseismicity band is interpreted here to likely represent aftershocks from the large 1991 earthquakes. If they are aftershocks, the T-wave earthquakes are probably strike-slip events (possibly with a reverse component) occurring on the re-activated mid-plate faults. Hence the T-wave epicenters delineate the aftershock zone of deformation and fault slip associated with the 1991 earthquakes as the central region along

the entire length of the Gorda plate. Furthermore, if the T-wave earthquakes reflect motion on the mid-plate faults and are indeed strike-slip with a reverse component, then this might explain the reverse motion observed on the mid-plate faults in the seismic reflection profile, not requiring E-W compression. Even a small reverse component (< 10°) along the 40-60 km long mid-plate faults (Figure 4.4) is enough to produce the 5-10 km reverse fault offsets seen on the reflection profiles.

The spatial-temporal distribution of the Gorda plate T-wave earthquakes suggests to us a relation to the strain release associated with the 1992 Cape Mendocino thrust mainshock and aftershock sequence. The idea that the Gorda plate N-S maximum compression could be coupled to the subduction zone stress was seemingly demonstrated by the occurrence of the two Cape Mendocino strike-slip aftershocks immediately following the thrust mainshock, which suggests significant coupling of the stresses between the Gorda and North American plates (Velasco et al., 1994). Indeed, finite element modeling (Wang et al.; 1997) suggests that Gorda plate N-S compression is primarily a result of strike-parallel subduction resistance at the Cascadia Subduction Zone. Thus the M>6 mid-plate earthquakes and aftershocks (T-wave band) occurred due to strain accumulation within the Gorda plate, possibly similar to strain accumulation (though not a perfect analogy) that occurs in the outer-rise of a subducting oceanic plate prior to a large subduction event (Chapple and Forsyth, 1979; Christensen and Ruff, 1988). Since the T-wave events increased in December 1991 and early 1992 after decreasing during the three months following the M>6 mid-plate events, this suggests that the M>6 earthquakes did not completely reduce strain within the mid-Gorda plate. Not until the Cape Mendocino earthquake occurred did the T-wave band intensity reduce and finally terminate. Since the T-wave band did not terminate immediately after the Mendocino earthquakes, we interpret

the eventual decline of the T-wave seismicity to represent a relaxation of mid-Gorda plate strain over the two months following the Mendocino events.

Another model also considered here is based on the idea that the T-wave band and the mid-plate reverse faults are occurring due to E-W horizontal compression. Following a model of the Cascadia Subduction Zone stress regime proposed by Wang et al. (1995), first the M>6 Gorda plate strike-slip earthquakes resulted from the regional, margin-parallel (N-S) maximum compressive stress field. Then the Gorda plate stress field may have shifted to a stress state with vertical $\sigma_3$ due to increased cross margin tectonic stress, while $\sigma_1$ remained oriented horizontal and N-S. This small, transient stress state, which may have resulted in slip along the mid-plate reverse faults and produced the microearthquake band, would be just a perturbation to the regional margin-parallel $\sigma_1$ and margin-normal horizontal $\sigma_3$ stress field. The stress field remained in this state until the Cape Mendocino mainshock, whereupon the regional stress field returned to horizontal E-W least compressive stress, and the microearthquake band subsided. This model is supported by the observation that the Cape Mendocino earthquake occurred under very low shear stress, with a stress drop of < 5 MPa (Velasco et al., 1994), and was followed within a day by two large Gorda plate aftershocks that occurred under strong N-S compression. Thus the M>6 Gorda plate strike-slip earthquakes might not have to be reconciled with the T-wave seismicity band since they may result from different stress states. Moreover, since mid-plate E-W compression is so prominent in the active fault data, it may be that E-W compression was only reduced somewhat after the Cape Mendocino event, and that E-W compressive strain continues to accumulate throughout the Gorda plate.

These dynamic models of the Gorda plate stress field may allow resolution of the observed seismicity and fault information, although several issues with the model remain equivocal. For example, the relatively small fault length of the Cape Mendocino earthquake

(~40 km), located at the extreme southern end of the Gorda plate, must provide the slip barrier for the ~300 km long Gorda-North American plate interface in order for the Mendocino event to affect the strain within the northern Gorda and southern Juan de Fuca plates. This may not be an issue since slip along the entire Gorda - North American interplate interface is not needed for the stress perturbation resulting in the T-wave band to be released, and therefore the rest of the interface could remain locked. Also, it is not clear how Gorda - North America relative plate motion relates (since it is oblique) to the observed mid-plate stress states and slip along the reactivated reverse faults. Relative plate motion fits best with the proposed models if the forearc is deforming rapidly, thus the coupling stress is more E-W. Lastly, since the Cape Mendocino event was near the MTJ, it may be that the observed Gorda - North America plate interactions at Cape Mendocino are more representative of a collision zone rather than a true subduction zone.

## 4.6 Implications

Although the nature of the actual stress state in the region at the time of the microseismicity band is not clearly resolved, the timing and spatial pattern of the hydroacoustically derived seismic activity seems to suggest some linkage between microseismicity in the mid-Gorda plate and the large earthquakes at Cape Mendocino. Such a relationship would be of tremendous value to earthquake risk assessment for populations on the adjacent active margin. To understand better the plate dynamics of the region and to help put this study in a clearer context, NOAA/PMEL is planning bathymetric and shipboard gravity surveys of the entire Gorda plate, from the continental margin out to and including the Gorda Ridge. Furthermore, it is not known from this single example whether this linkage is specific to the Cascadia Subduction Zone, with its extremely young and easily deformed down-going plate, or is a relationship that can be generally applied to

subduction zones worldwide. In order to address this question, in June 1994 NOAA/PMEL expanded the number of SOSUS channels collected to extend the area of monitoring to include the western/central Aleutian Trench and the subduction zones of the western North Pacific. In addition, autonomous hydrophone moorings have been developed by NOAA/PMEL and were deployed in the eastern central Pacific in May 1996, allowing hydroacoustic monitoring of the subduction zones offshore Central and South America (Fox and Matsumoto, 1995). It is anticipated that as hydroacoustically derived epicenters are accumulated for these more active subduction zones, a better understanding will be obtained of the generality of the apparent relationship between outer-rise microseismicity and subsequent large subduction zone earthquakes.

## 4.8 Acknowledgments

The authors wish to thank Robert S. Yeats for helpful reviews and comments. This research was supported through the NOAA VENTS Program, PMEL Contribution Number 1807.

## 4.9 References

Chapple, W.M. and D.W. Forsyth. 1979. Earthquakes and Bending of Plates at Trenches. *J. Geophys. Res.*, 84:6729-6749.

Christensen, D.H. and L.J. Ruff. 1988. Seismic Coupling and Outer Rise Earthquakes. *J. Geophys. Res.*, v:93, 13421-13444.

Dengler, L, G. Carver, and R. McPherson. 1992. Sources of North Coast Seismicity. *Calif. Geol*, 45:40-53.

Dziak, R.P., C.G.Fox, A.E. Schreiner. 1995. The June-July 1993 Seismo-acoustic Event at CoAxial Segment, Juan de Fuca Ridge: Evidence for a Lateral Dike Injection. *Geophys. Res. Lett.*, 22:135-138.

Dziak, R.P., C.G. Fox, H. Matsumoto, A.E. Schreiner. 1997. The April 1992 Cape Mendocino Earthquake Sequence: Seismo-acoustic Analysis Utilizing Fixed Hydrophone Arrays. *Mar. Geophys. Res.*, in press.

Dziewonski, A.M., G. Ekstrom, and M.P. Salganik. 1992. Centroid-Moment Tensor Solutions for July- September 1991. *Phys. Earth Planet. Inter.*, 72:1-11.

Dziewonski, A.M., G. Ekstrom, and M.P. Salganik, Centroid-Moment Tensor Solutions for April-June 1992, Phys. Earth Planet. Inter., 77:151-163, 1993.

Embley, R.W., W.W. Chadwick, Jr., I.A. Jonasson, D.A. Butterfield, and E.T. Baker. 1995. Initial results of the rapid response to the 1993 CoAxial event: relationships between hydrothermal and volcanic processes. *Geophys. Res. Lett.*, 22:143-146.

Fox, C.G., W.E. Radford, R.P. Dziak, T-K. Lau, H. Matsumoto, and A.E. Schreiner. 1995. Acoustic detection of a seafloor spreading Episode on the Juan de Fuca Ridge using military hydrophone arrays. *Geophys. Res. Lett.*, 22:131-134.

Fox, C.G. and H. Matsumoto. 1996. Monitoring northeast Pacific seismicity using autonomous hydrophone moorings. *EOS, Trans. Amer Geophys. Un.*, 76:412.

Fox, C.G., R.P. Dziak, H. Matsumoto, and A.E. Schreiner. 1994. Potential for Monitoring Low-level Seismicity on the Juan de Fuca Ridge Using Fixed Hydrophone Arrays. *Mar. Tech. Soc.*, 27:22-30.

Goldfinger, C., L.D. Kulm, R.S. Yeats, C. Mitchell, R. Weldon, II, C. Peterson, M. Darienzo, W. Grant, and G.R. Priest. 1992. Neotectonic Map of the Oregon Continental Margin and Adjacent Abyssal Plain. *Oregon Dep. Geol. Min. Ind. Open File Rep. 0-92-4.*

Heaton, T.H. and S.H. Hartzell. 1987. Earthquake Hazards on the Cascadia Subduction Zone. *Science*, 236:162-168.

Kanamori, H.. 1977. Seismic and Aseismic Slip along Subduction Zones and their Tectonic Implications. In *Island Arcs, Deep Sea Trenches, and Back-Arc Basins*, Maurice Ewing Ser., v:1, ed M. Talwani and W.C. Pitman III, 163-174, AGU, Washington, D.C.

Lay, T., J.W. Given, and H. Kanamori. 1982. Long-period Mechanism of the 8 November 1980 Eureka, California, Earthquake. *Bull.Seism. Soc. Am.*, 71:1-24.

McCaffrey, R., and C. Goldfinger. 1995. Forearc Deformation and Great Subduction Zone Earthquakes: Implications for Cascadia Offshore Earthquake Potential. *Science*, 267:856-859.

Oppenheimer, D., G. Beroza, G. Carver, L. Dengler, J. Eaton, L. Gee, F. Gonzalez, A. Jayko, W.H. Li, M. Lisowski, M. Magee, G. Marshall, M. Murray, R. McPherson, B. Romanowicz, K. Satake, R. Simpson, P. Somerville, R. Stein, D. Valentine.

1993. The Cape Mendocino, California Earthquake Sequence of April 1992: Subduction at the Triple Junction. *Science*, 261:433-438.

Preliminary Determination of Epicenters. 1992. National Earthquake Information Center, April.

Riddihough, R.P. 1984. Recent Plate Motions. *JFP-9, Open file 83-6*, Pacific Geoscience Centre, Earth Physics Branch, Sydney, B.C., Canada.

Rogers, G.C.. 1979. Earthquake Fault Plane Solutions Near Vancouver Island. *Can. J. Earth Sci.*, 16:523-531.

Velasco, A.A., C.J. Ammon, T. Lay. 1994. Recent Large Earthquakes near Cape Mendocino and in the Gorda plate: Broadband Source Time Functions, Fault Orientations, and Rupture Complexities. *J. Geophys. Res.*, 99:711-728.

Wang, K., T. Mulder, G.C. Rogers, R.D. Hyndman. 1995. Case for Very Low Coupling Stress on the Cascadia Subduction Fault. *J. Geophys. Res.*, 100:12907-12918.

Wang, K., J. He, and E. E. Davis. 1997. Transform Push, Oblique Subduction Resistance, and Intraplate Stress of the Juan de Fuca Plate. *J. Geophys. Res.*, 102:661-674.

Wilson, D. 1986. A Kinematic Model for the Gorda Deformation Zone as a Diffuse Southern Boundary of the Juan De Fuca Plate. *J. Geophys. Res.*, 91:10259-10269.

Wilson, D. 1989. Deformation of the So-Called Gorda Plate. *J. Geophys. Res.*, 94:3065-3075.

# Chapter 5

## Recent Tectonics of the Blanco Ridge, Eastern Blanco Transform Fault Zone

Robert P. Dziak
Department of Geosciences
Oregon State University
Corvallis, OR 97331

Christopher G. Fox and Robert W. Embley
National Oceanic and Atmospheric Administration
Pacific Marine Environmental Laboratory
Hatfield Marine Science Center
Newport, OR 97365

John L. Nabelek and Jochen Braunmiller
College of Ocean and Atmospheric Sciences
Oregon State University
Corvallis, OR 97331

Randolf A. Koski
United States Geological Survey
MS999 345 Middlefield Rd
Menlo Park, CA 94025

In Preparation
*Journal of Geophysical Research*
American Geophysical Union
Washington, D.C.

## 5.1 Abstract

Bathymetric, hydro-acoustic, seismic, submersible, and gravity data are used to investigate the active tectonics of the eastern Blanco Transform Fault Zone (BTFZ). The eastern BTFZ is dominated by the ~150 km long transform-parallel Blanco Ridge (BR) which is a right-lateral strike-slip fault bordered to the east and west by the Gorda and Cascadia Depressions. Acoustic locations, fault-parameter information, and slip vector estimates of 43 earthquakes ($M_w \geq 3.8$) that occurred along the eastern BTFZ over the last 5 years reveal that the Blanco Ridge is a high-angle right-lateral strike-slip fault, with a small component of dip-slip motion, where the Juan de Fuca plate is the hanging wall relative to the Pacific plate. Furthermore, the Cascadia and Gorda basins are undergoing normal faulting with extension predominantly oblique to the transform trend. Earthquake P-axes are generally horizontal and oriented 39°-59° to the strike of the BR, suggesting the fault may exhibit a high shear stress. Seafloor submersible observations help constrain the active transform fault trace to be an elongate basin that runs the length of the BR summit. Brecciated and undeformed basalt, diabase, and gabbro samples were collected at the four submersible survey sites along the Blanco Ridge. These petrologic samples indicate the Blanco Ridge is composed of an ocean crustal sequence that has been uplifted and highly fractured. The petrologic samples also appear to show an increase in elevation of the crustal section from east to west along the Blanco Ridge, with gabbros exposed at a shallower depth farther west along the southern (Pacific plate side) BR ridge flank. Further supporting evidence for BR uplift exists in the presence of sedimentary rocks found at the BR summit, seismic reflection profiles across the BR showing uplift of turbidite sequences along the north and south ridge base, and gravity and magnetics profiles that indicating possible basement uplift and a low-density zone centered on the ridge's Pacific plate side. The BR formation mechanism preferred here is

first, uplift achieved partially through strike-slip motion (with a small dip-slip component). Second, seawater penetration along the fault into the lower crust upper mantle, which then enhanced formation and intrusion of a mantle-derived serpentinized-peridotite diapir into the shallow ocean crust, causing further uplift along the fault

## 5.2 Introduction

The Blanco Transform Fault Zone (BTFZ), located in the NE Pacific ocean off the coast of Oregon, is a 350 km long right-lateral strike-slip transform fault that links the moderate-spreading rate Juan de Fuca and Gorda Ridges (Figure 5.1). Utilizing available high resolution bathymetry, Embley and Wilson (1992) divided the BTFZ into five major right-stepping strike-slip fault segments that are separated by deep extensional basins. The majority of these basins were interpreted to be the oceanic analog of pull-apart basins observed along continental divergent wrench fault systems, while one, the Cascadia Depression, was interpreted as a proto-spreading center (deCharon, 1988). The BTFZ has long been known to generate large earthquakes ($m_b > 6$) that are tectonic in origin (Tobin and Sykes, 1969; Chandra, 1974; Dziak et al., 1991). The Blanco Ridge (BR), the fault segment that connects the Cascadia and Gorda Depressions, is the longest structurally uninterrupted strike-slip fault segment within the BTFZ (~150 km in length). Accordingly, the largest earthquakes within the entire BTFZ have occurred along the BR, with five earthquakes of $m_b \geq 6$ occurring in the last 30 yrs (Dziak et al., 1991). However, comparison of BTFZ slip rates estimated from plate motion models to slip rates estimated from seismic moment release over the past 30 yrs suggests that >80% of the slip along the BTFZ is occurring aseismically (Dziak et al., 1991). This may be due to the thermal character of oceanic crust along transform faults, with elevated crustal

isotherms that may result in a less well coupled fault zone (Bergman and Solomon, 1988).

The Blanco Ridge is an example of one of the more enigmatic features of fracture zones, the transform-parallel or transverse ridge. Origins proposed for these transform ridges includes serpentinite intrusion (Bonatti, 1976; Bonatti, 1978), volcanism resulting from extension across the transform (Thompson and Melson, 1972), dip-slip faulting from a component of extension or compression (Bonatti, 1978), or uplift of the plate on the young side of the fracture zone due to thermal constrasts (Craig and MacKenzie, 1986). Serpentinite intrusion involves seawater percolating down along the fault to mantle depths where, once in the presence of water, mantle peridotite is altered to serpentinite which then rises diapirically and contributes to the formation of a transform parallel ridge (Bonatti, 1978). Ridge forming volcanic activity along fracture zones exists as hotspot volcanism at the Louisville Ridge/Heezen Fracture Zone (Epp, 1984), ridge-perpendicular non-hotspot volcanoes near the East Pacific Rise (Batiza and Vanko, 1983), and small linear chains of volcanoes along East Pacific Rise non-transform offsets (Lonsdale, 1985). Pockalny et al., (1995) and Pockalny et al. (1996) demonstrated that a shift in the pole of plate rotation and a subsequent change in the ridge spreading direction has lead to extension and normal faulting along the Kane and Siqueiros Fracture Zones, and compression and reverse faulting along the 21°30'N (Atlantic) and Clipperton Fracture Zones, with both faulting styles leading to the flexural formation of a transform parallel ridge. Hekinian et al. (1992) propose a combination of mechanisms for uplift of ultramafics and gabbros associated with the median ridge along the Garret Transform. They suggest that the transform ridge formed through strike-slip (with a small component of dip-slip) tectonism, which allowed penetration of seawater to the lower crust upper mantle and enhanced serpentinization and diapiric ascent. Estimates of a Blanco Ridge

formation mechanism generally have been hampered by a lack of data, since prior to this work rock samples have been recovered from only two sites along the BR's extreme east and west ends. During August and September of 1994, a dive program utilizing the U.S. Navy's DSV *Turtle* and Advanced Tethered Vehicle (ATV) was carried out along the Blanco Ridge and Gorda Depression to map significant structural features and better understand eastern BTFZ tectonics and BR formation.

The availability of the U.S. Navy's SOund SUreveillance System (SOSUS) hydrophone arrays in combination with the recent establishment of a broadband seismograph network allows for monitoring of the Juan de Fuca plate seismicity with unprecedented location accuracy and source parameter detail. The SOSUS data are analyzed by the NOAA T-phase Project and locates offshore earthquakes utilizing the event's water-borne Tertiary (T-) wave. Precisely known ocean sound speed models and an array geometry that is much improved over land-based seismic networks allows for highly accurate (±3 km error in latitude and longitude) event locations over a wide range ($2.0<M<7$) of magnitudes (Fox et al., 1994). Seismograph-derived epicenters for NE Pacific ocean earthquakes typically have a 10 to 35 km northeastward bias in location (Dziak et al., 1991). Although the hydrophone array locations are not for public distribution, earthquake locations are not classified. The Pacific-Northwest broadband array, deployed in 1992, consists of over twenty digital 3-component broadband high-dynamic range seismic stations distributed along coastal northern California, Oregon, Washington, and British Columbia. Effective, routine estimation of an events source moment tensor, depth, and source time function for events of magnitude 4.0 and larger has been demonstrated (Nabelek and Xia, 1995; Braunmiller et al., 1995).

The purpose of this study is to combine the preliminary geologic mapping and petrologic results of the 1994 BTFZ dive series with the recent earthquake moment-tensor

solutions, SOSUS earthquake locations, and high resolution bathymetry to understand the state of stress and the mechanics of crustal deformation along the eastern BTFZ, and attempt to address the question of a formation mechanism of the Blanco Ridge.

## 5.3 Blanco Ridge Tectonic Setting and Regional Morphology

The Blanco Ridge (BR) is the right-lateral strike-slip fault segment, trending at about 111°, that forms the eastern portion of the Blanco Transform Fault Zone connecting the pull-apart basins of the Cascadia and Gorda Depressions. Figure 5.1 shows the Blanco Ridge bathymetry with the location of faults, fracture zones, and turbidite channels identified from the bathymetry, while Figures 5.2 and 5.3 show three-dimensional perspectives of the ridge. The Blanco Ridge is composed of a series of lozenge-shaped highs with about 600 to 1000 m of bathymetric relief, and varying from 3.5 km wide just north of the Gorda Depression to 7 km wide about midway between the Gorda and Cascadia Depressions. The shoalest point along the Blanco Ridge is at 128°00'W, where the ridge rises to less than 1900 m deep. West of its shoalest point, the ridge deepens until it ends at the intersection with the SE corner of the Cascadia Depression at 128°40'W. From 128°35'W to 128°20'W, a series of back-tilted normal fault blocks from the Cascadia Depression form the northwestern boundary of the Blanco Ridge. The blocks direct the Cascadia Channel along the base of the Blanco Ridge and into the Cascadia Depression. South of the ridge, between 127° 50'W and 127° 35'W, the Pacific plate exhibits a series of bent abyssal ridges that are probably drag folds that formed in response to strike-slip motion along the transform.

The detailed bathymetry of the ridge from about 128°00'W to 127°40'W reveals a series of closed basins and lineaments which collectively appear to follow the 111° BTFZ trend, at least along distances of about 10 km. These features were interpreted by Embley

Figure 5.1. Sea Beam bathymetric map of the Cascadia Depression, Blanco Ridge, and Gorda Depression, eastern Blanco Transform Fault Zone (BTFZ). Inset maps show location and generalized geologic structure of the BTFZ. Line drawing on top of bathymetry delineates active faults and major geologic features of the region. Solid lines represent faults, dashed lines are fracture zones, and dotted lines show course of turbidite channels. When possible to estimate sense of motion on a fault, a filled circle shows the down-thrown side. Location of seismic reflection and gravity/magnetics profiles indicated by opposing brackets. D-D' and E-E' are the seismic reflection profiles shown in Figure 5.9, F-F' is the seismic reflection profile shown in Figure 5.10, and G-G' is the gravity and magnetics profile shown in Figure 5.15. Location of a Blanco Ridge slump scar indicated by half-rectangle, inferred direction of slump shown by arrow, and debris location designated by an "S". CD stands for Cascadia Depression, BR is Blanco Ridge, GD is Gorda Depression, and GR is Gorda Ridge. Numbers on north and south side of transform represent Juan de Fuca and Pacific plate crustal ages inferred from magnetic anomalies. Long-term plate motion rate between the Pacific and southern Juan de Fuca plates from Wilson (1989).

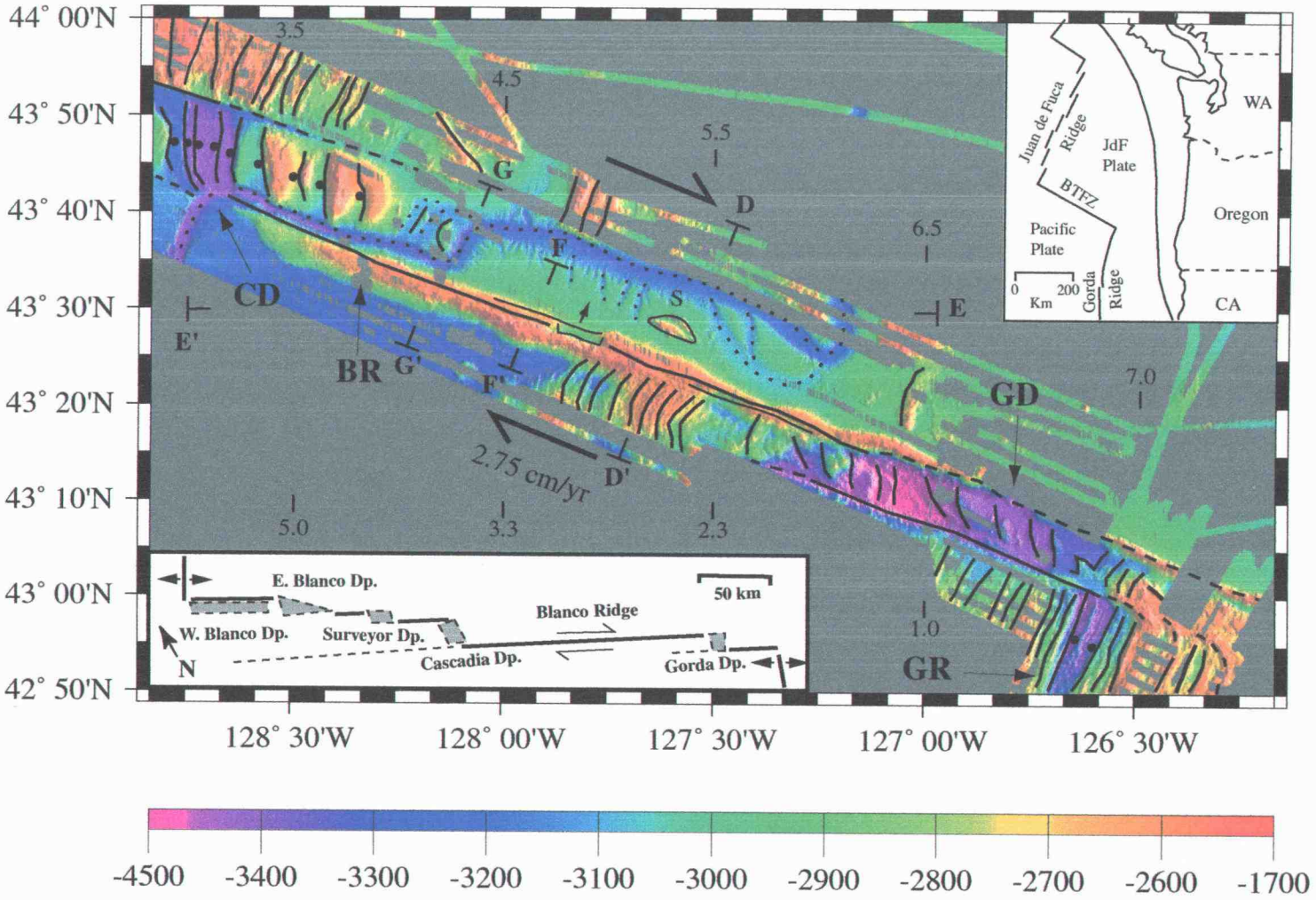
44° 00'N
43° 50'N
43° 40'N
43° 30'N
43° 20'N
43° 10'N
43° 00'N
42° 50'N
128° 30'W
128° 00'W
127° 30'W
127° 00'W
126° 30'W
3.5
4.5
5.5
6.5
7.0
5.0
3.3
2.3
1.0
G
D
F
S
E
CD
E'
BR
G'
F'
D'
GD
GR
2.75 cm/yr
E. Blanco Dp.
50 km
Blanco Ridge
W. Blanco Dp.
Surveyor Dp.
Cascadia Dp.
Gorda Dp.
N
Juan de Fuca
Ridge
JdF
Plate
BTFZ
Pacific
Plate
WA
Oregon
CA
Gorda
Ridge
0
200
Km
-4500
-3400
-3300
-3200
-3100
-3000
-2900
-2800
-2700
-2600
-1700

Figure 5.1

Figure 5.2. Three-dimensional perspective of bathymetry from the western half of the Blanco Ridge and Cascadia Depression. Black arrows delineate transform-parallel linear notch at the BR summit, which is the probable active transform fault trace. White arrows highlight uplifted turbidite bench identified by Ibach (1981), and a lineation (fault generated) that cuts the bench.

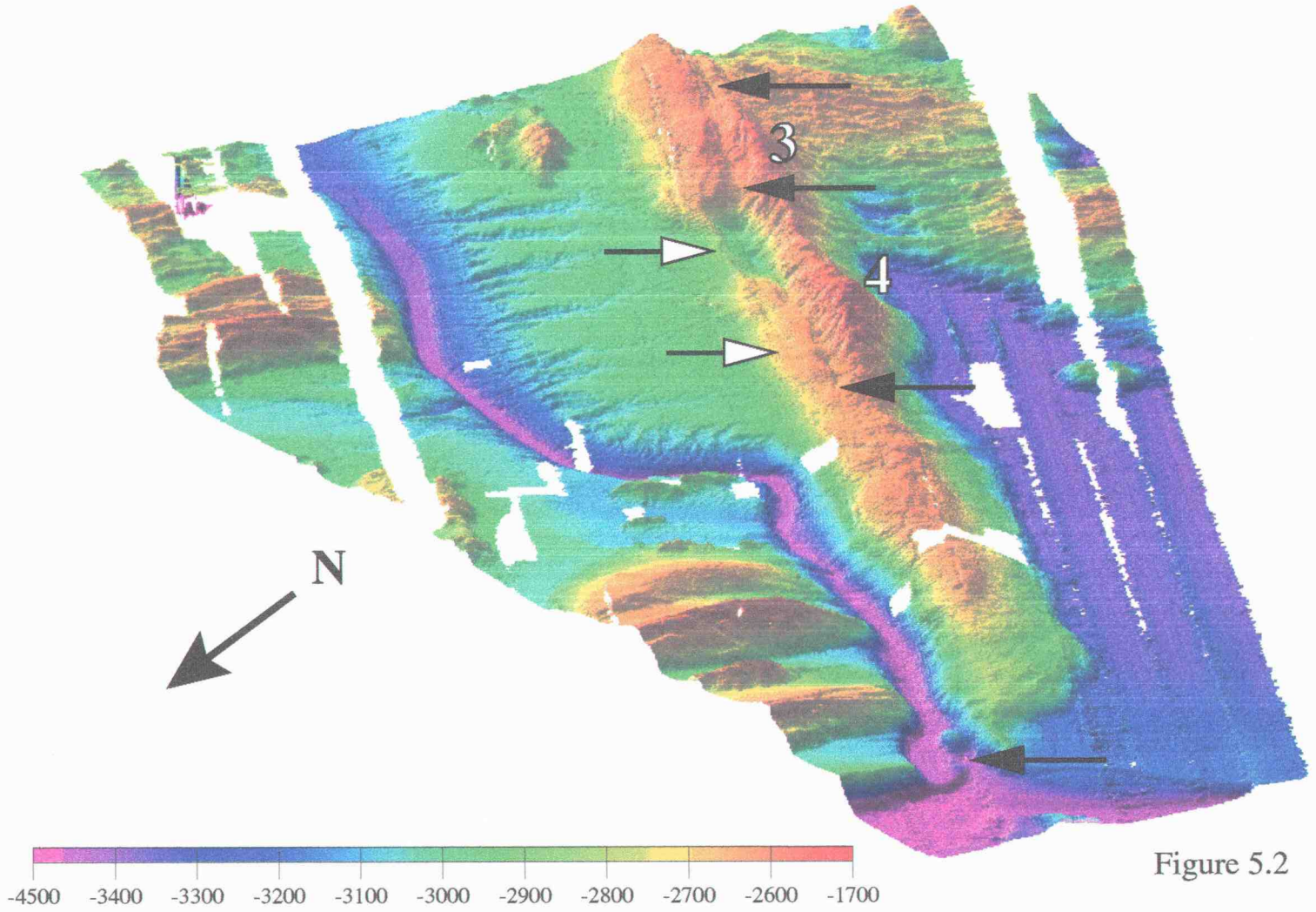


Figure 5.2

Figure 5.3. Three-dimensional perspective of bathymetry from the eastern half of the Blanco Ridge, Gorda Depression, and northern tip of the Gorda Ridge. Black arrows highlight probable location of active transform fault trace as it enters the northwestern section of Gorda Depression from the Blanco Ridge, and as it borders the south Gorda Depression and northern Gorda Ridge. White arrows delineate fault generated lineation observed from bathymetry (discussed further in text).

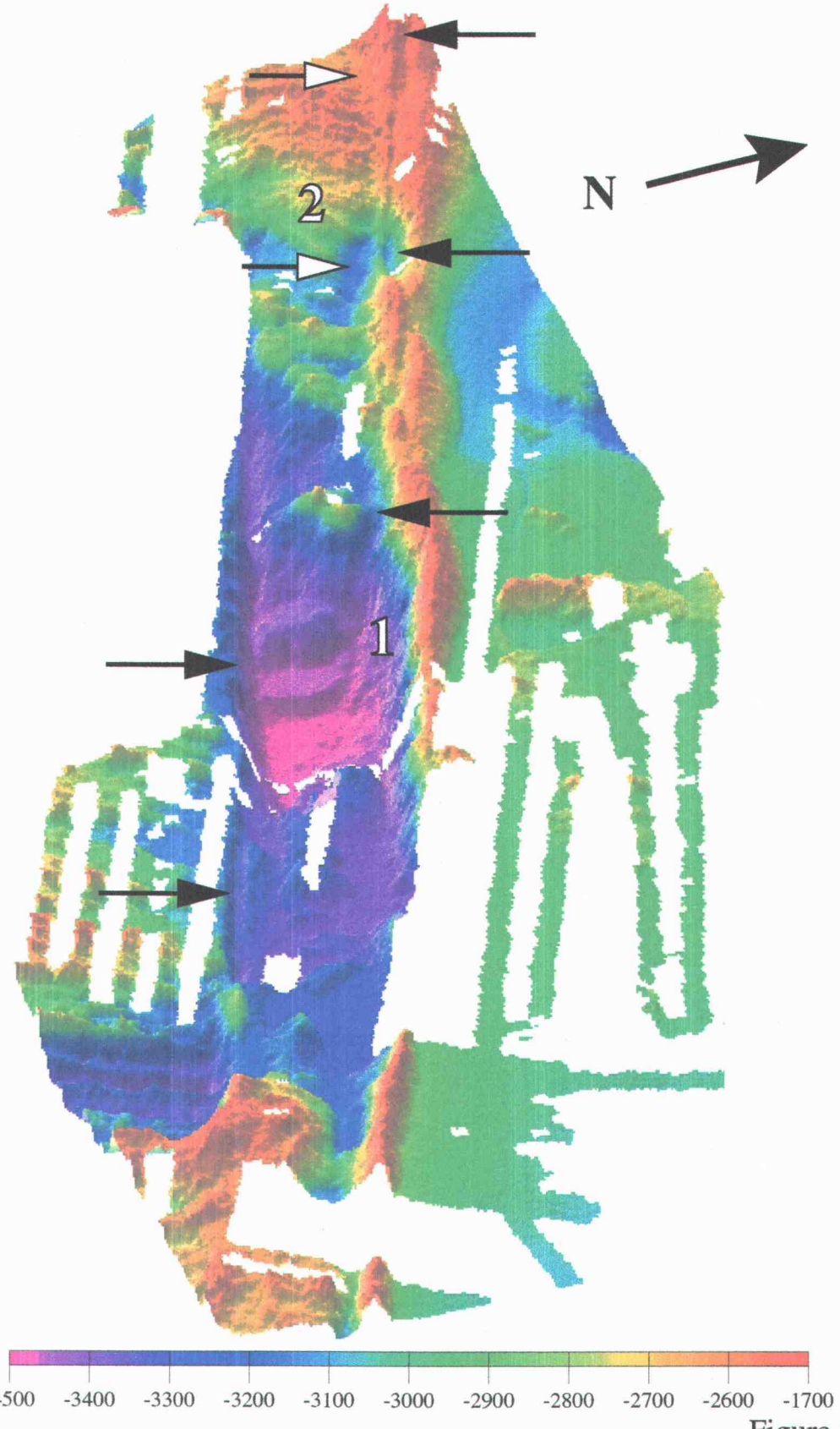


Figure 5.3

and Wilson (1992) to delineate the zone of most recent strike-slip faulting. Indeed, these narrow basins can be traced as a long narrow lineation along the summit of the Blanco Ridge (identified by black arrows in Figures 5.2 and 5.3), and could be the active transform fault zone. The narrow cross-section of the Blanco Ridge and the lack of any obvious volcanic-constructional features (such as small cones) make a volcanic origin of the ridge highly unlikely. Ibach (1981) presents a seismic reflection profile across the north side of the ridge between 127° 30'W and 128° 05'W that shows a bench of uplifted (~500 m) and layered turbidite sequence (Figure 5.2, identified by the white arrows). Along the north flank of the turbidite bench, there is a pronounced lineation (also identified by the white arrows in Figure 5.2) not identified by either Ibach (1981) or Embley and Wilson (1992). Review of the raw Sea Beam data suggests that this lineament is a real feature in the seafloor and not an artifact of non-overlapping swaths like the linear data gap just above the upper white arrow in figure 5.2. There is also a similar lineament along the south side, and parallel to, the Blanco Ridge between 127° 40'W and 127° 20'W (white arrows, Figure 5.3). The lineation in the bench could be an expression of a dip-slip fault forming in response to uplift of the bench, or as a result of slip partitioning along the transform. Also, the lineation could be an *en échelon* strike-slip fault that helps accommodate slip over the entire transform fault zone. The nature of these features will be addressed in later sections

North of the Blanco Ridge, between 128°05'W and 127°12'W, the Cascadia Deep-Sea Channel (dotted line, Figure 5.1) parallels the Blanco Ridge and cuts into flat-lying turbidites (Ibach, 1981; Embley, 1985), before turning southwest to flow between the Cascadia Depression back-tilted fault blocks (deCharon, 1988) and the BR (dotted line in Figure 5.1). Embley (1985) has described a secondary channel system (identified

by the southward pointing v-shaped drainage pattern north of the BR) that drains in to the Cascadia Channel. Erosion of these channels may result from slumps and turbidity currents from the sediment bench on the ridge's north side, and as a result of backcutting .from deepening of the Cascadia Channel base level.

The Blanco Ridge is bounded to the east and west by two pull-apart basins, the Gorda and Cascadia Depressions, respectively (Embley and Wilson, 1992). The Cascadia Depression (CD) is bounded on either side by a series of inward-facing back-tilted blocks which are covered by a thick turbidite sequence (Griggs and Kulm, 1973). The CD normal faults are oriented about 10° to 15° from orthogonal to strike of the southern (BR) and northern bounding transform faults. The CD normal faults and back-tilted blocks also appear to be rotated counterclockwise relative to the BR and the observed structure just to the north in the Juan de Fuca plate. The Cascadia Channel thalweg drops 130 m as it enters the CD, which was interpreted by Griggs and Kulm (1973) to be a result of CD subsidence at a rate of 1.8 cm $yr^{-1}$ over the last 6.6 ka. Seismic reflection profiles suggest there is up to 500 m of sediment in the CD, with a small 60 m relief ridge in the center of the basin flanked by small (5-10 m relief) back-tilted blocks fault blocks that mirror the large-scale structures surrounding the basin (deCharon, 1988). Also, acoustic opaque zones in the seismic reflection profiles have been cited as evidence for igneous intrusion within the basin fill (Embley et al., 1987). The point at which the active strike-slip fault from the BR enters the CD seems to be represented as a small linear trough along the southern edge of the Cascadia Channel (Figure 5.2).

To the east, the Blanco Ridge merges with the northern edge of the Gorda Depression (GD). Here too the active fault trace, as it enters the northwestern edge of the basin (Figure 5.3), seems to be delineated by a linear trough. Based on its rhomb-graben morphology, Embley and Wilson (1992) conclude that the GD was formed by extension

between two strike-slip fault strands; the BR to the north and a strike-slip fault strand along its southern border extending to the Gorda Ridge. Sea Marc II side scan data suggests the presence of lava flows emanating from fissures on the floor of the GD (Clague and Holmes, 1987), however dredge samples across the basin provided no fresh basalts. Fault blocks identified from bathymetry within the Gorda Depression appear to be rotated even more counter-clockwise (~20° - 25°) to the trend of the BR than those within the Cascadia Depression. The GD is bounded by longer strike-slip fault segments than is the CD, which suggests the GD comprises a more diffuse zone of oblique faulting. As a result, the GD fault blocks may undergo a significant component of strike-slip motion, and are thus not labeled as only normal faults.

Magnetic anomaly data indicate the Cascadia Depression and Blanco Ridge strike-slip fault formed as a result of a clockwise change in Juan de Fuca - Pacific plate motion at about 5 Ma (Wilson et al., 1984; Wilson, 1993). The Cascadia Depression may be a remnant of a rift segment that died as a result of a southward propagation event about 5 Ma (Embley and Wilson, 1992). The Gorda Depression may have originated in a similar way about 1- 2 Ma. Embley and Wilson (1992) speculate that a component of extension or compression across the BTFZ is resisting the development of a single through-going transform fault. Ibach (1981) proposed that there is compression across the Blanco Ridge as evidenced by the uplifted turbidite bench. Since the best seismological evidence at that time indicated the Blanco Ridge was undergoing pure strike-slip faulting (Chandra 1974), Embley and Wilson (1992) suggested the bench uplift was a result of serpentinite diapirism. Further, they suggested that between extension and compression along the Blanco Ridge, extension seemed more likely. The obliquity in the strikes of the BR and Mendocino Transform would tend to produce compression across the Mendocino, and extension across the Blanco Ridge.

Figure 5.1 shows the approximate ages of the Juan de Fuca and Pacific plates, estimated from magnetic anomalies by Wilson (1993), along adjoining sections of the transform. Crust of the Pacific plate is considerably younger (2.75 - 7.0 Ma) than that of the Juan de Fuca plate from the Gorda Ridge west to 127° 30'W. West of 127° 30'W the two plates are similar in age, with the Juan de Fuca plate ~1.5 Ma younger than the Pacific near the Cascadia Depression. This relative age difference could affect the relative buoyancy of the two plates and hence the style of faulting along the transform. The older plate may tend to subside relative to the younger plate during strike-slip faulting, resulting in a component of dip-slip motion during a given earthquake. It is interesting to note that the pull-apart basins are located where the relative age differences between the Juan de Fuca and Pacific plates becomes significantly > 2 m.y., suggesting the subsidence of the older plate plays a role in the stability and development of these pull-apart basins.

## 5.4 T-wave Locations, Focal Mechanisms, and Slip Vector Information

Figures 5.4 and 5.5 show bathymetry, earthquake focal mechanisms, and epicenters of 43 earthquakes ($3.8 \leq M \leq 6.5$) that occurred along the Blanco Ridge between August, 1992 to February, 1997. The earthquakes were located by the NOAA T-phase Project using acoustic earthquake data from the Navy's SOSUS hydrophone arrays. The SOSUS locations, location error, and magnitudes, and seismic locations, magnitudes, and CMT information are summarized in Tables 5.1 and 5.2. The earthquake locations estimated by hand-selecting T-wave arrival times from hydrophone data generally locate close to mapped active faults along the Blanco Ridge, and in general differ from NEIC locations by between 4 and 71 km to the south-southwest (Table 5.1). Using hydrophone T-wave arrivals results in a locational error (covariance matrix

Figure 5.4. Diagram shows recent earthquakes ($4.1 \leq M_w \leq 6.5$), plotted on top of bathymetry of the eastern BTFZ, that occurred from 1992-1994. Earthquake focal mechanisms were estimated by the Oregon State University seismic laboratory through moment-tensor inversion of regional broadband waveform data. Earthquakes were located by the NOAA T-phase Project using acoustic earthquake data from the Navy's SOSUS hydrophone arrays. Focal mechanisms represent lower-hemisphere equal area projections, with the compressional quadrants shaded. Diameter of mechanisms is proportional to the earthquake's moment magnitude White circles are aftershocks from the 10/27/94 $M_w$=6.5 (event 12) that occurred within one day of the mainshock. The earthquake locations estimated from hydrophone data generally locate close to mapped active faults along the Blanco Ridge, and differ from NEIC locations by 10 to 35 km to the south-southwest. Location and fault parameter information are listed in Tables 5.1 and 5.2.

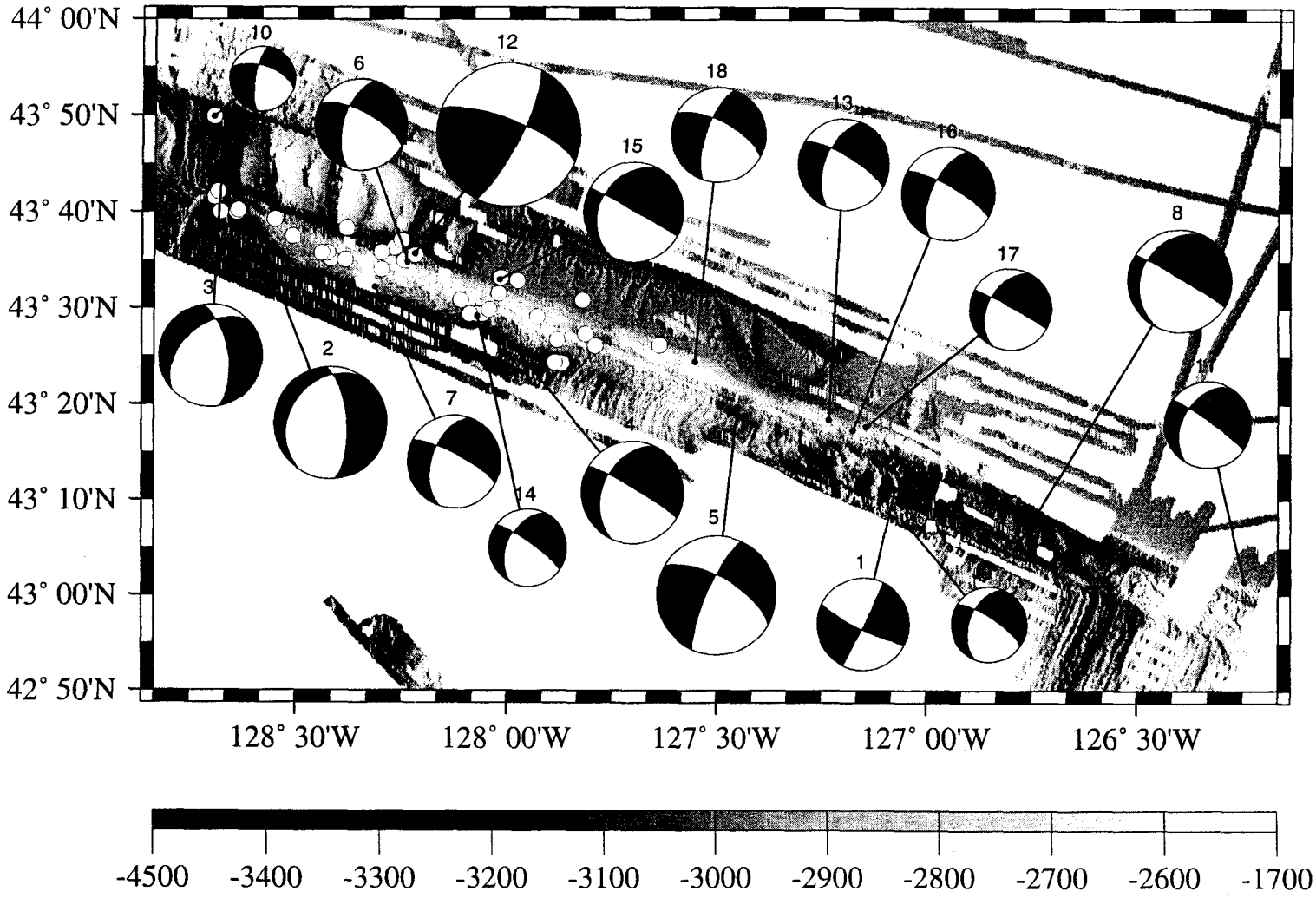
44° 00'N
43° 50'N
43° 40'N
43° 30'N
43° 20'N
43° 10'N
43° 00'N
42° 50'N
128° 30'W
128° 00'W
127° 30'W
127° 00'W
126° 30'W
10
6
12
18
13
16
15
8
17
3
2
7
4
14
5
1
-4500
-3400
-3300
-3200
-3100
-3000
-2900
-2800
-2700
-2600
-1700

Figure 5.4

Figure 5.5. Diagram showing recent earthquakes ($3.8 \leq M_w \leq 5.5$), plotted on top of bathymetry of the eastern BTFZ, that occurred from 1995-1997. Mechanism and location information same as in Figure 5.4.

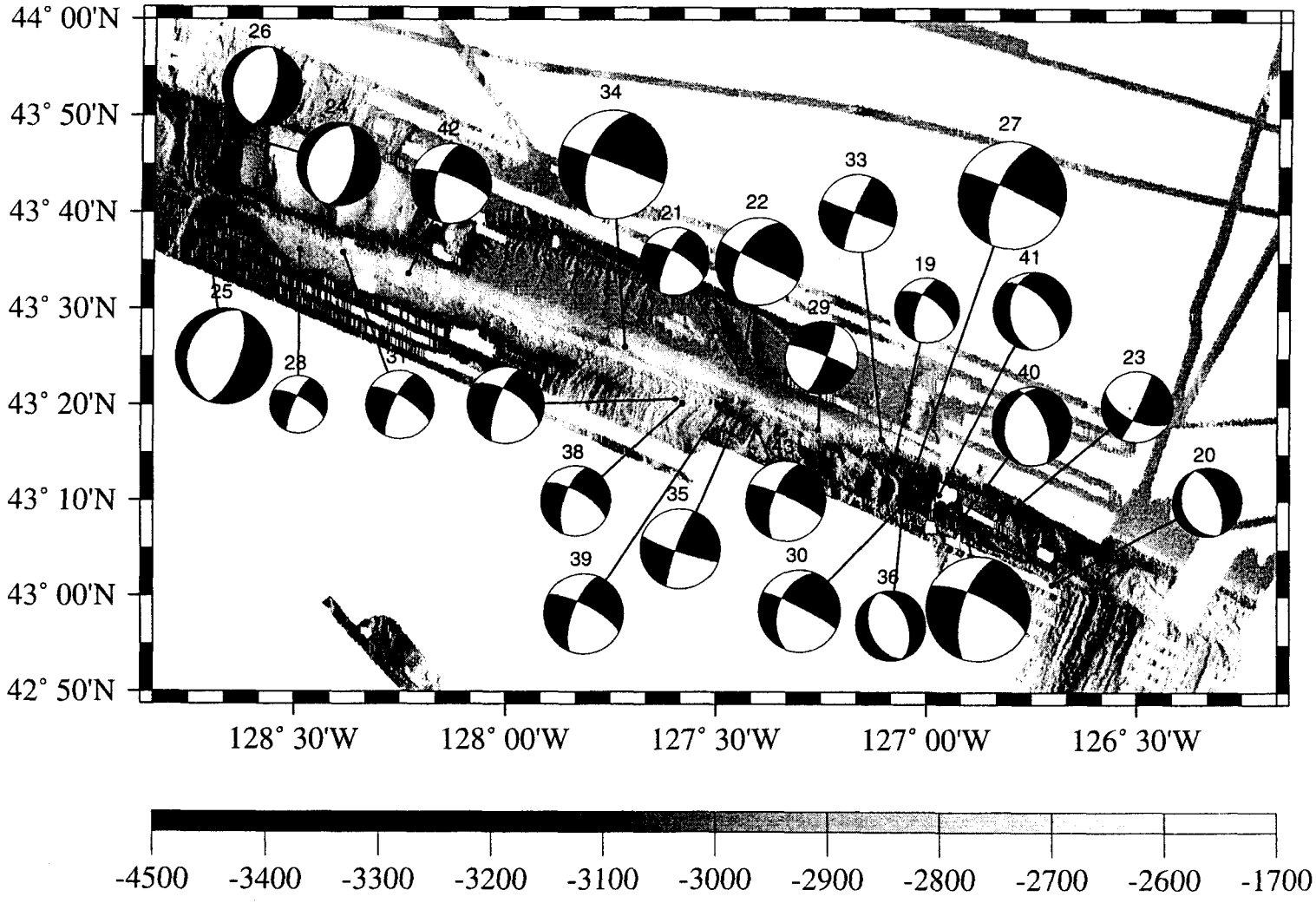
44° 00'N
43° 50'N
43° 40'N
43° 30'N
43° 20'N
43° 10'N
43° 00'N
42° 50'N
128° 30'W
128° 00'W
127° 30'W
127° 00'W
126° 30'W
26
24
42
34
21
22
33
27
19
41
25
29
28
31
40
23
38
35
20
39
30
36
-4500
-3400
-3300
-3200
-3100
-3000
-2900
-2800
-2700
-2600
-1700

Figure 5.5

**TABLE 5.1: Earthquake Origin Times, Locations, and Magnitudes**

| Event | Date | Seismic | | | | | SOSUS | | | |
|---|---|---|---|---|---|---|---|---|---|---|
| | | OT | Lat(°) | Lon(°) | h(km) | Mag | OT | Lat(°) | Lon(°) | Mag(dB) |
| 1 | 080492 | 142741.2 | 43.468 | -127.014 | 015 | b4.9 | 142713 | 43.185 | -127.074 | 229.1 |
| 2 | 082192 | 010218.4 | 43.930 | -128.344 | 015 | b5.5 | 010202 | 43.791 | -128.682 | 227.5 |
| 3 | 111792 | 203720.0 | 44.096 | -128.543 | 006 | w4.8 | 203646 | 43.772 | -128.674 | 228.2 |
| 4 | 050993 | 221649.0 | 43.717 | -128.120 | 006 | w5.0 | 221604 | 43.450 | -128.003 | 228.4 |
| 5 | 011994 | 011626.0 | 43.630 | -128.150 | 009 | w5.7 | 011600 | 43.328 | -127.450 | 230.6 |
| 6 | 061494 | 020415.0 | 43.825 | -128.293 | 006 | w4.9 | 020351 | 43.580 | -128.237 | 228.7 |
| 7 | 063094 | 073045.0 | 43.745 | -127.984 | 006 | b4.3 | 073015 | 43.537 | -128.314 | 223.2 |
| 8 | 071394 | 175246.0 | 43.450 | -126.648 | 006 | w5.2 | 175217 | 43.085 | -126.786 | 224.9 |
| 9 | 072294 | 224415.0 | 43.320 | -126.846 | 006 | w4.4 | 224355 | 43.121 | -127.040 | 225.5 |
| 10 | 081294 | 112619.0 | 43.877 | -126.397 | 009 | w4.1 | 112506 | 43.832 | -128.695 | 222.7 |
| 11 | 102794 | 043827.0 | 43.216 | -126.698 | 004 | w4.7 | 043840 | 43.025 | -126.248 | 228.6 |
| 12 | 102794 | 174556.0 | 43.630 | -127.340 | 015 | w6.5 | 174511 | 43.595 | -128.219 | 226.3 |
| 13 | 103094 | 022325.0 | 43.448 | -127.417 | 009 | w4.9 | 022313 | 43.306 | -127.234 | 225.4 |
| 14 | 103094 | 205414.0 | 43.647 | -127.194 | 006 | w4.4 | 205356 | 43.486 | -128.072 | 224.3 |
| 15 | 110294 | 204836.0 | 43.799 | -127.854 | 004 | w5.1 | 204815 | 43.550 | -128.018 | 227.5 |
| 16 | 110694 | 040442.0 | 43.675 | -127.464 | 006 | w4.9 | 040430 | 43.288 | -127.174 | 225.2 |
| 17 | 110794 | 150251.0 | 43.557 | -127.107 | 009 | w4.6 | 150235 | 43.294 | -127.143 | 226.6 |
| 18 | 112294 | 212322.0 | 43.483 | -127.687 | 006 | w5.0 | 212310 | 43.406 | -127.553 | 228.1 |
| 19 | 032895 | 034345.0 | 43.372 | -127.053 | 006 | w4.0 | 034333 | 43.233 | -127.077 | 223.5 |
| 20 | 050495 | 061852.0 | 43.189 | -126.687 | 006 | w4.2 | 061850 | 43.022 | -126.701 | 211.8 |
| 21 | 051295 | 235046.0 | 43.389 | -127.255 | 006 | w4.1 | 235036 | 43.392 | -127.442 | 226.1 |
| 22 | 051395 | 060349.0 | 43.534 | -127.171 | 006 | w4.7 | 060336 | 43.389 | -127.442 | 229.9 |
| 23 | 080395 | 054159.0 | 43.177 | -126.709 | 006 | w4.2 | 054137 | 43.160 | -126.782 | 223.6 |
| 24 | 090295 | 094135.0 | 43.764 | -128.499 | 009 | w4.6 | 094145 | 43.812 | -128.693 | 218.3 |
| 25 | 092595 | 075824.0 | 43.752 | -128.515 | 009 | w5.0 | 075808 | 43.812 | -128.746 | 222.5 |
| 26 | 092595 | 080149.0 | 43.752 | -128.515 | 009 | w4.5 | 080126 | 43.840 | -128.709 | 212.7 |
| 27 | 092695 | 013915.0 | 43.319 | -127.160 | 006 | w5.4 | 013833 | 43.151 | -127.061 | 222.7 |
| 28 | 101595 | 064952.0 | 43.668 | -128.540 | 006 | w3.8 | 064949 | 43.603 | -128.491 | 217.6 |
| 29 | 101995 | 145957.0 | 43.312 | -127.277 | 010 | w4.3 | 150058 | 43.292 | -127.257 | 221.4 |
| 30 | 122495 | 025122.0 | 43.270 | -127.043 | 004 | w4.6 | 025058 | 43.163 | -127.053 | 223.7 |
| 31 | 020696 | 053200.0 | 43.689 | -128.369 | 004 | w4.2 | 053152 | 43.598 | -128.388 | 226.7 |
| 32 | 022096 | 005210.0 | 43.212 | -127.144 | 004 | w5.3 | 005147 | 43.143 | -126.907 | 228.8 |
| 33 | 022096 | 012111.0 | 43.218 | -127.162 | 006 | w4.4 | 012105 | 43.275 | -127.107 | 227.6 |
| 34 | 041596 | 122924.0 | 43.474 | -127.711 | 004 | w5.4 | 122917 | 43.434 | -127.717 | 230.1 |
| 35 | 051896 | 191401.0 | 43.390 | -127.633 | 004 | w4.5 | 191352 | 43.336 | -127.434 | 227.1 |
| 36 | 071796 | 223615.0 | 43.143 | -127.182 | 006 | w4.2 | 223611 | 43.161 | -127.054 | 221.2 |
| 37 | 101696 | | | | 006 | w4.4 | 125033 | 43.344 | -127.596 | 222.1 |
| 38 | 101696 | | | | 009 | w4.2 | 130740 | 43.337 | -127.580 | 218.1 |
| 39 | 110496 | | | | 006 | w5.5 | 225405 | 43.337 | -127.479 | 228.7 |
| 40 | 111996 | | | | 004 | w4.5 | 221959 | 43.139 | -126.912 | 222.2 |
| 41 | 112496 | | | | 006 | w4.4 | 182228 | 43.179 | -126.969 | 224.1 |
| 42 | 011397 | 163252.0 | 43.537 | -128.181 | 004 | w4.5 | 163250 | 43.561 | -128.232 | 225.4 |
| 43 | 022097 | | | | 006 | w4.5 | 110344 | 43.287 | -127.398 | 227.2 |

**TABLE 5.2: SOSUS Location Errors, First Nodal Planes, P- T-axes, SlipVectors**

| Event | No Sta | Location Error (ΔLt°) | (ΔLn°) | (ΔOT) | First Nodal Plane φ(°) | δ(°) | λ(°) | P-axis Az(°) | Pl(°) | T-axis Az(°) | Pl(°) | SV Az(°) |
|---|---|---|---|---|---|---|---|---|---|---|---|---|
| 1 | 3 | 0.00 | 0.00 | 00.0 | 116 | 080 | -178 | 340 | 009 | 194 | 080 | 295.8 |
| 2 | 4 | 0.01 | 0.02 | 01.4 | 214 | 028 | -055 | 238 | 064 | 099 | 021 | 154.4 |
| 3 | 4 | 0.05 | 0.06 | 05.0 | 351 | 063 | -124 | 213 | 058 | 104 | 012 | 128.7 |
| 4 | 4 | 0.02 | 0.01 | 01.8 | 301 | 084 | -131 | 175 | 037 | 062 | 027 | 115.1 |
| 5 | 4 | 0.07 | 0.07 | 06.3 | 300 | 065 | -166 | 160 | 027 | 254 | 009 | 114.6 |
| 6 | 4 | 0.09 | 0.18 | 08.1 | 299 | 068 | -146 | 160 | 039 | 065 | 006 | 118.2 |
| 7 | 4 | 0.02 | 0.04 | 01.5 | 298 | 078 | -140 | 166 | 036 | 062 | 018 | 126.9 |
| 8 | 3 | 0.00 | 0.00 | 00.0 | 301 | 087 | -116 | 186 | 043 | 053 | 036 | 115.7 |
| 9 | 3 | 0.00 | 0.00 | 00.0 | 304 | 076 | -135 | 172 | 041 | 066 | 018 | 138.0 |
| 10 | 3 | 0.00 | 0.00 | 00.0 | 290 | 058 | -159 | 146 | 036 | 242 | 009 | 115.8 |
| 11 | 4 | 0.07 | 0.06 | 04.5 | 306 | 084 | -132 | 180 | 036 | 069 | 027 | 121.6 |
| 12 | 4 | 0.08 | 0.14 | 08.8 | 292 | 073 | 166 | 159 | 002 | 252 | 022 | 109.9 |
| 13 | 4 | 0.03 | 0.02 | 03.0 | 301 | 075 | -145 | 166 | 035 | 067 | 012 | 112.3 |
| 14 | 4 | 0.04 | 0.04 | 02.7 | 306 | 079 | -136 | 176 | 038 | 069 | 021 | 118.7 |
| 15 | 4 | 0.06 | 0.08 | 05.4 | 299 | 089 | -121 | 182 | 038 | 056 | 037 | 118.9 |
| 16 | 4 | 0.001 | 0.001 | 00.01 | 300 | 078 | -150 | 165 | 030 | 069 | 011 | 113.8 |
| 17 | 4 | 0.001 | 0.001 | 00.01 | 299 | 087 | -134 | 173 | 033 | 063 | 028 | 118.9 |
| 18 | 6 | 0.02 | 0.04 | 03.4 | 298 | 067 | -157 | 158 | 032 | 249 | 001 | 126.4 |
| 19 | 6 | 0.04 | 0.05 | 06.3 | 304 | 061 | -150 | 160 | 041 | 252 | 002 | 160.0 |
| 20 | 4 | 0.03 | 0.03 | 05.7 | 339 | 062 | -091 | 247 | 073 | 070 | 017 | 075.4 |
| 21 | 4 | 0.01 | 0.02 | 01.8 | 301 | 071 | -159 | 163 | 028 | 073 | 000 | 114.9 |
| 22 | 3 | 0.00 | 0.00 | 00.0 | 117 | 088 | 141 | 169 | 024 | 065 | 028 | 296.5 |
| 23 | 3 | 0.00 | 0.00 | 00.0 | 117 | 058 | -176 | 336 | 024 | 075 | 019 | 297.6 |
| 24 | 3 | 0.00 | 0.00 | 00.0 | 012 | 062 | -096 | 269 | 072 | 106 | 017 | 068.3 |
| 25 | 4 | 0.003 | 0.004 | 00.2 | 019 | 064 | -090 | 289 | 071 | 110 | 019 | 098.6 |
| 26 | 4 | 0.03 | 0.02 | 01.4 | 014 | 062 | -088 | 289 | 073 | 103 | 017 | 170.4 |
| 27 | 4 | 0.01 | 0.01 | 00.5 | 295 | 084 | -155 | 161 | 022 | 066 | 013 | 113.2 |
| 28 | 4 | 0.07 | 0.05 | 03.2 | 299 | 070 | -165 | 160 | 024 | 252 | 004 | 118.8 |
| 29 | 3 | 0.00 | 0.00 | 00.0 | 291 | 083 | -010 | 155 | 012 | 246 | 002 | 199.8 |
| 30 | 4 | 0.04 | 0.03 | 02.2 | 297 | 083 | -136 | 168 | 035 | 061 | 023 | 123.1 |
| 31 | 4 | 0.04 | 0.03 | 01.8 | 301 | 072 | -162 | 341 | 074 | 105 | 009 | 210.6 |
| 32 | 4 | 0.04 | 0.02 | 01.9 | 296 | 072 | -153 | 159 | 031 | 066 | 005 | 117.8 |
| 33 | 4 | 0.02 | 0.01 | 01.1 | 111 | 089 | 173 | 156 | 004 | 066 | 006 | 290.9 |
| 34 | 6 | 0.02 | 0.02 | 00.9 | 291 | 088 | -143 | 162 | 026 | 059 | 023 | 112.5 |
| 35 | 6 | 0.01 | 0.01 | 00.6 | 109 | 082 | 171 | 155 | 001 | 064 | 012 | 290.2 |
| 36 | 6 | 0.02 | 0.02 | 00.9 | 341 | 050 | -089 | 263 | 085 | 069 | 005 | 188.6 |
| 37 | 6 | 0.01 | 0.01 | 00.6 | 302 | 061 | -157 | 158 | 036 | 252 | 006 | 197.7 |
| 38 | 6 | 0.02 | 0.02 | 00.7 | 300 | 068 | -151 | 160 | 035 | 068 | 003 | 108.7 |
| 39 | 6 | 0.05 | 0.05 | 02.4 | 298 | 073 | -157 | 161 | 028 | 069 | 004 | 124.2 |
| 40 | 5 | 0.01 | 0.03 | 00.9 | 338 | 062 | -108 | 212 | 068 | 082 | 015 | 059.1 |
| 41 | 6 | 0.02 | 0.02 | 00.9 | 316 | 057 | -118 | 174 | 065 | 066 | 008 | 166.1 |
| 42 | 6 | 0.02 | 0.02 | 00.2 | 291 | 076 | -147 | 156 | 034 | 058 | 011 | 120.0 |
| 43 | 6 | 0.06 | 0.07 | 03.5 | 294 | 081 | -153 | 160 | 026 | 064 | 012 | 109.4 |

diagonals) of between 0.01° - 0.2° in latitude and longitude, 0.1 - 8.0 sec in origin time. In Table I where no seismic location is listed, indicates the hydrophone location was used to estimate the CMT solution. The first two mechanisms listed in Table 5.1 were obtained from the NEIC Preliminary Determination of Epicenters catalog (August, 1992). The remaining mechanisms were estimated using moment-tensor inversion of the earthquakes' regional broadband waveforms (Nabelek and Xia, 1995; Braunmiller et al., 1994). The style of faulting shown by each mechanism is consistent with the geologic structure of its location, i.e. normal faulting events occurred within the Cascadia and Gorda pull-apart basins while the strike-slip events occurred along the Blanco Ridge. Thirty-one of the Blanco Ridge strike-slip mechanisms have a component of normal motion, and indicate that the Juan de Fuca plate is the hanging wall relative to the Pacific plate during these events, subsiding along near vertical fault planes. Three events (12, 22, and 35) show a component of reverse motion along the Blanco Ridge, with the Juan de Fuca plate also the hanging wall. Normal faulting events (2, 3, 9, 20, 25, 26, 36, 40, and 41) occurred along transform-oblique structures within the extensional Cascadia and Gorda Depressions, with most extensional-basin events showing a component of strike-slip motion. There are strike-slip events that border, and occur within, these extensional basins (1, 9, 8, 10, 19, 23, 27, 30, and 32), and probably are a result of strike-slip faulting entering the pull-apart basins. Event 11 seems to have occurred as a result of faulting along the (theoretically) inactive part of the fracture zone. Event 11 could have been caused by subsidence due to density contrasts, since its strike-slip mechanism indicates the older Juan de Fuca plate dropped relative to the younger Gorda plate. Overall, the mechanisms seem to indicate that the entire Blanco Ridge is undergoing predominantly strike-slip faulting with a component of normal motion, where the Juan de Fuca plate is the hanging wall and is subsiding relative to the Pacific plate. The strike-slip fault planes

appear to be fairly consistent, with strikes between 290° - 310°, rakes of -116° to -178°, and most dips near vertical, but all >58°.

Also shown in Figure 5.4 are the location of the 10/27/94 $M_w$=6.5 mainshock, and 42 of its aftershocks that occurred over the following 26 hours. The NEIC (Preliminary Determination of Epicenters, October 1994) reports 2 aftershocks during this time period. Since aftershocks roughly delineate the mainshock fault-plane, it appears that about half the Blanco Ridge (~75 km) ruptured during the 10/27/94 ($M_w$ 6.5) earthquake. The 10/27/94 earthquake was the largest BTFZ earthquake in four decades and had an unusually long rupture duration (Braunmiller et al., 1994), not uncommon in transform fault earthquakes (Ihlme and Jordan, 1994). The mainshock is situated in the center of the aftershock distribution, suggesting the rupture may have propagated bilaterally. Also, there seems to be evidence that the earthquake ruptured a discrete fault segment since the aftershocks terminate to the west where the fault entered the Cascadia Depression, and to the east in an area of structural complexity where N-NE trending abyssal ridges intersect the transform fault at 127° 40'W.

The maximum and minimum compressive stress axes and slip vectors of the 43 CMT earthquakes along the eastern BTFZ are shown on Figures 5.6 and 5.7, summarized in Table 5.2, and shown on a rose diagram in Figure 5.8. In Figure 5.6, the P- and T-axes are plotted parallel to their azimuth, with their length corresponding to the cosine of plunge. Thus pure strike-slip earthquakes have horizontal P- and T-axes and plot with unit length of one, while pure normal fault earthquakes have horizontal T-axes with unit length one, and vertical P-axes with zero length. The T-axes within the Cascadia Depression are orthogonal to fault blocks within the basin, while the P-axes are small with variable orientations, indicative of a normal faulting regime with extension parallel to the transform trend. T-axes within the Gorda Depression are orthogonal to structure

Figure 5.6. Orientation of earthquake P- and T-axes along the eastern BTFZ. White bars are P-axes, grey bars are T-axes. Lengths of axes are proportional to the cosine of the plunge, thus horizontal axes have a unit length of one, while vertical axes are zero.

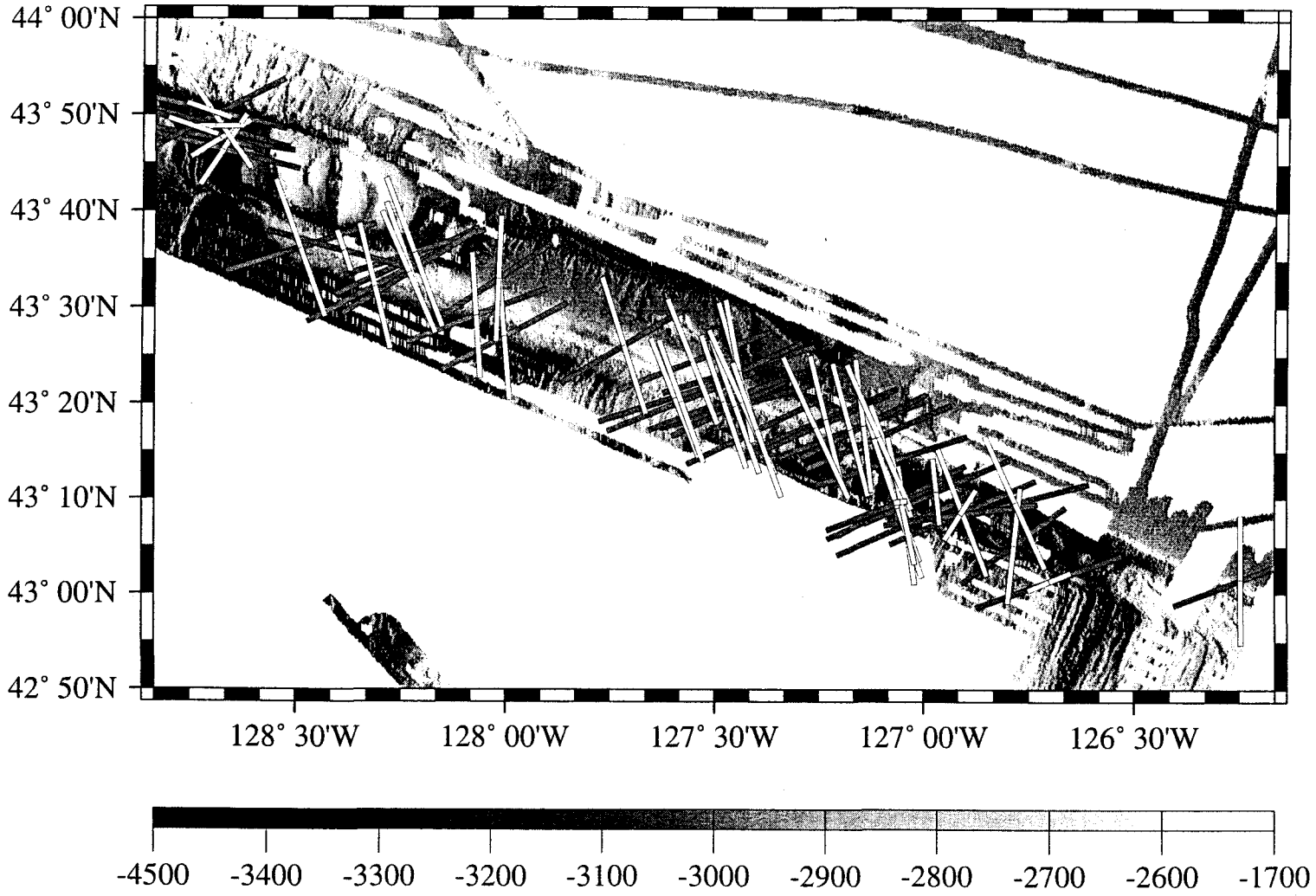
44° 00'N
43° 50'N
43° 40'N
43° 30'N
43° 20'N
43° 10'N
43° 00'N
42° 50'N
128° 30'W
128° 00'W
127° 30'W
127° 00'W
126° 30'W
-4500
-3400
-3300
-3200
-3100
-3000
-2900
-2800
-2700
-2600
-1700

Figure 5.6

Figure 5.7. Orientation of earthquake slip vectors along the eastern BTFZ. Slip vectors were calculated using equation (4.83) from Aki and Richards (1980) to get the x (north), y (east), and z (down) vector components. The vector was then projected to horizontal and plotted with its length proportional to the earthquake's moment magnitude.

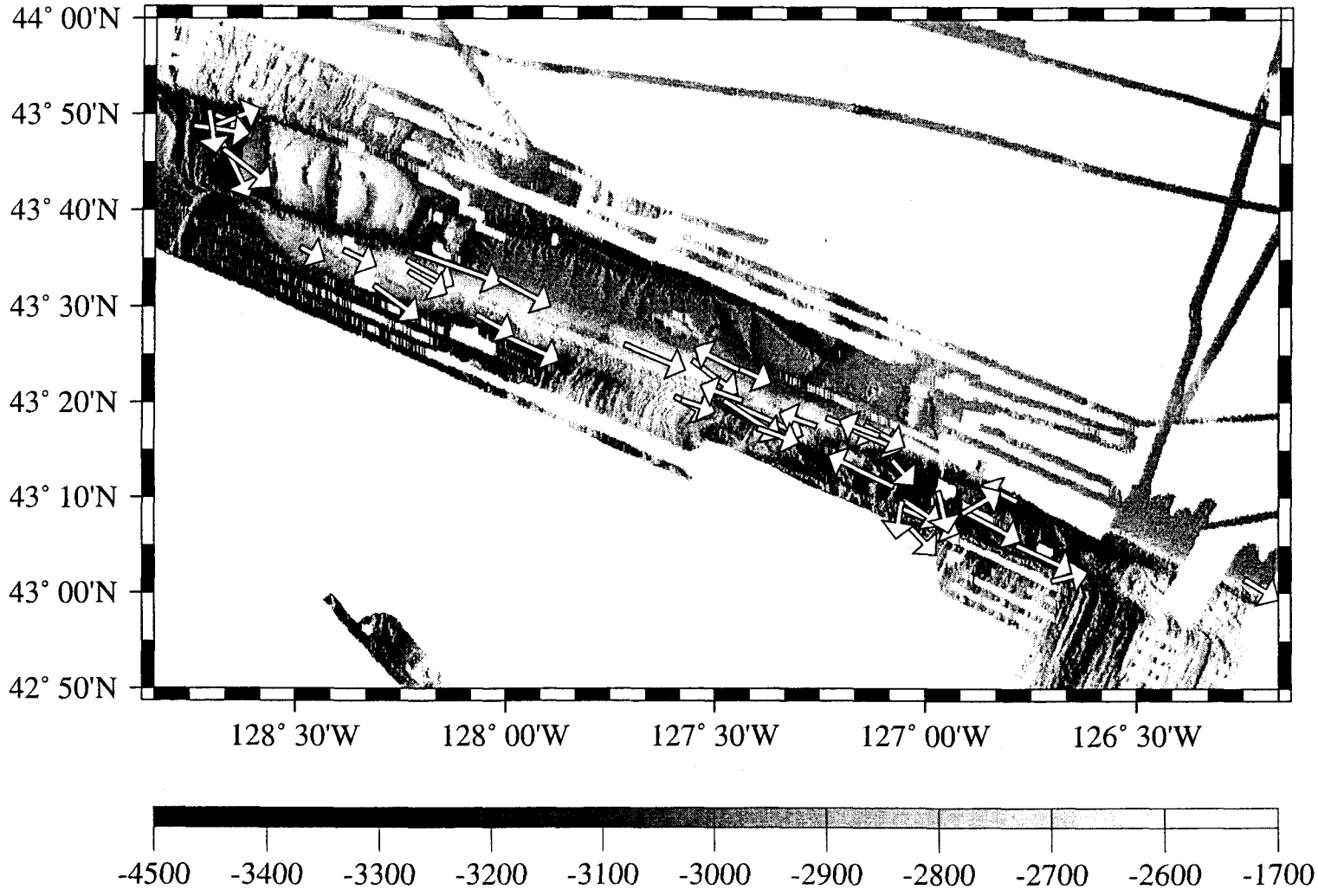
44° 00'N
43° 50'N
43° 40'N
43° 30'N
43° 20'N
43° 10'N
43° 00'N
42° 50'N
128° 30'W
128° 00'W
127° 30'W
127° 00'W
126° 30'W
-4500
-3400
-3300
-3200
-3100
-3000
-2900
-2800
-2700
-2600
-1700

Figure 5.7

within the basin, and indicate NE-SW extension that is oblique to the transform trend. The Blanco Ridge P-axes are predominantly large and have fairly consistent NW-SE trends. Figure 5.8 shows all the P-axis trends relative to the strike of the Blanco Ridge (heavy arrow at 111°). The majority of the P-axes are nearly horizontal and oriented between 39° to 59° to the strike of the BR. Thus the P-axes orientations are near the optimum angle of 45° for the maximum principal stress axis along a fault, suggesting the fault is resistant to shear failure and may exhibit a high shear stress.

Slip vectors were calculated from the nodal plane information listed in Table 5.2 using equation (4.83) from Aki and Richards (1980) to get the x (north), y (east), and z (down) vector components. Each vector was projected onto horizontal with its azimuth representing the original plunge direction, and plotted with its length proportional to earthquake magnitude (Figure 5.7). The slip vectors within the extensional basins indicate a wide range of slip orientation. Some of these vectors are oblique while others parallel the trend of the transform, probably reflecting diffuse dip-slip faulting within the pull-apart basins. The slip vectors from the strike-slip earthquakes generally parallel the trend of the BR (heavy-black arrow at 111° in Figure 5.8). The majority of the large strike-slip vectors following eastern BTFZ transform motion oriented south (0° - 9°) of the BR trend, and north of the direction of relative motion (~ N120°E) between the Juan de Fuca and Pacific plates estimated from Nuvel-1 (Demets et al., 1990).. Thus it seems that slip during individual earthquakes may not necessarily parallel the overall 111° transform trend or predicted relative plate motion. The various vector orientations may represent slip along individual fault strands that comprise the transform fault zone.

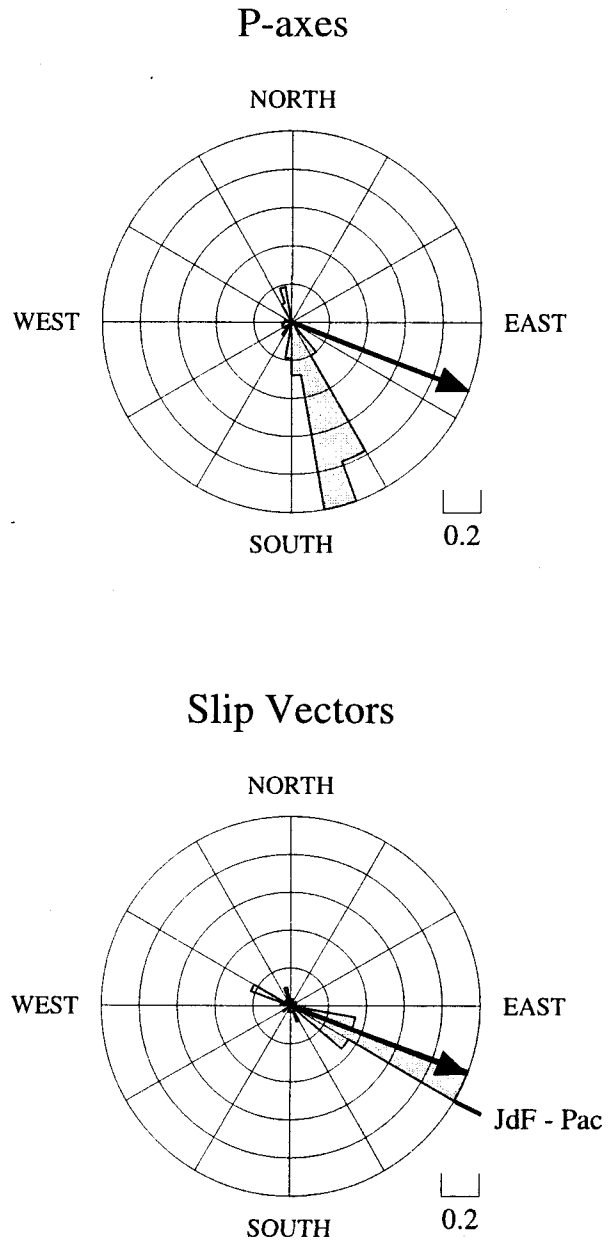


Figure 5.8. Rose diagrams showing orientation of earthquake P-axes (top) and slip vectors (bottom). Heavy black arrows on each diagram represents the BTFZ trend (~111°). In general, P-axes are oriented between 39° to 59° to the strike of the transform. The majority of large horizontal slip vectors following eastern BTFZ transform motion are oriented between the trend of the Blanco Ridge and the Juan de Fuca-Pacific plate relative motion vector (~N120E).

## 5.5 Single Channel Air-Gun Reflection Profiles

Single channel air-gun reflection profiles were collected along the Blanco Ridge in 1969 (Oregon State University Seismic Reflection Laboratory), and in 1985 by U.S.G.S. personnel during a cruise aboard the R/V S.P. Lee. The 1969 survey was the basis for a structure and tectonic study of the BTFZ by Ibach (1981). Ibach (1981) identified a north dipping turbidite sequence (Figure 5.9), along the northern base of the Blanco Ridge at longitude 127° 40'W, that had been uplifted ~ 200 m above the regional depth of the turbidite deposition. These turbidites are most likely spill-over deposits from the Cascadia Channel that overlie Blanco Ridge basement, and thus suggests that the Blanco Ridge and turbidite sequence have been uplifted. The uplifted turbidites produced a prominent bench on the north side of the Blanco Ridge that can be traced from 127° 40'W to 128° 10'W (Ibach, 1981, and white arrows in Figure 5.2), a distance of ~ 40 km along the BR with evidence of uplift. Ibach (1981) also interpreted the reflection profiles as indicating the presence of a south-dipping fault with a component of reverse motion at the base of the Blanco Ridge that was causing the uplift of the ridge and turbidites (Figure 5.9). The 1969 survey also shows that along the south side of the Blanco Ridge, the Pacific plate becomes markedly deeper as it approaches the BR, with the overlying sediments showing stratigraphic thickening and structural deformation adjacent to the BR. Ibach (1981) interpreted this section as a south dipping fault, with evidence of ~ 300 m of uplift of the Blanco Ridge relative to the abyssal plain sediments from an uplifted sediment wedge overlying the BR south base. The bottom of Figure 5.9 again shows Ibach's (1981) interpretation of a south dipping fault along the north BR base. In contrast to the findings of Ibach (1981), the 1969 reflection profiles in Figure 5.9 are interpreted here as indicating north dipping BR basement overlain nonconformably by the turbidites

Figure 5.9. Diagram showing single-channel airgun reflection profiles and interpretations, after Ibach (1981). Top diagram shows north-south profile across the Blanco Ridge (at 127° 40'W), and interpretation (profile D-D' in Figure 5.1). The top profile illustrates the uplifted and faulted nature of the Blanco Ridge as shown by the uplifted turbidite bench. Ibach (1981) interpreted the profile to show a south dipping along the northern Blanco Ridge, which is not necessarily supported by the data. Bottom diagram shows northeast-southwest profile paralleling the Blanco Ridge and interpretation (profile E-E' in Figure 5.1). Profile again illustrates the faulted and uplited nature of the Blanco Ridge, and shows uplifted sediment wedges on both the north and south sides. On the south side of the Blanco Ridge there is evidence for subsidence of the Pacific plate and overlying sediments.

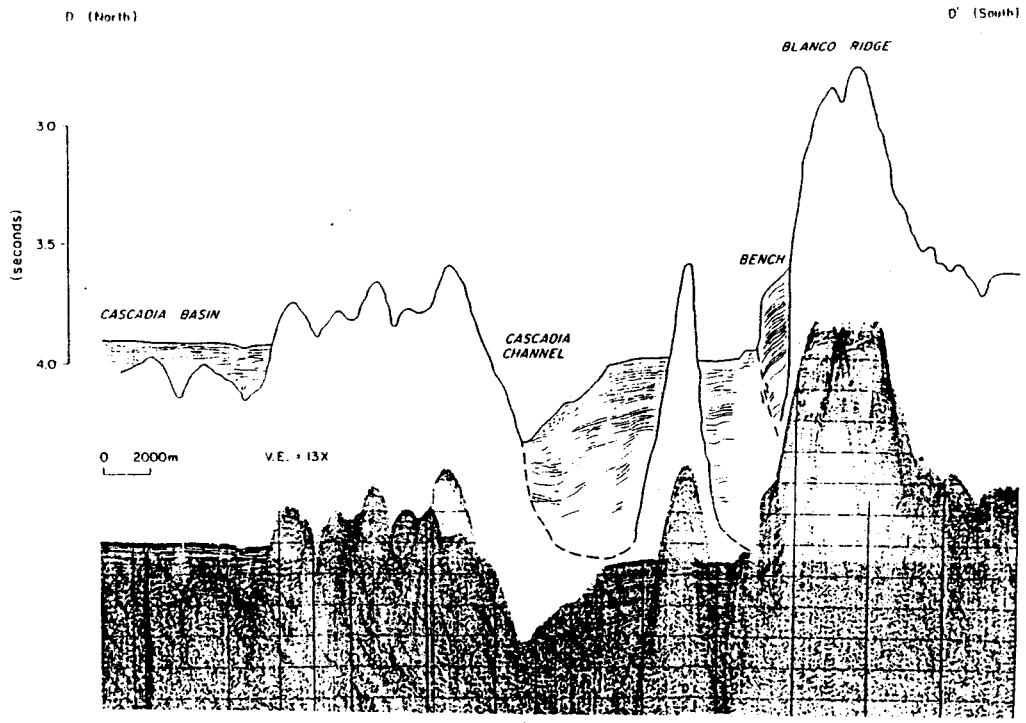
D (North)
D' (South)
BLANCO RIDGE
3.0
3.5
4.0
(seconds)
BENCH
CASCADIA BASIN
CASCADIA CHANNEL
0 2000m
V.E. = 13X

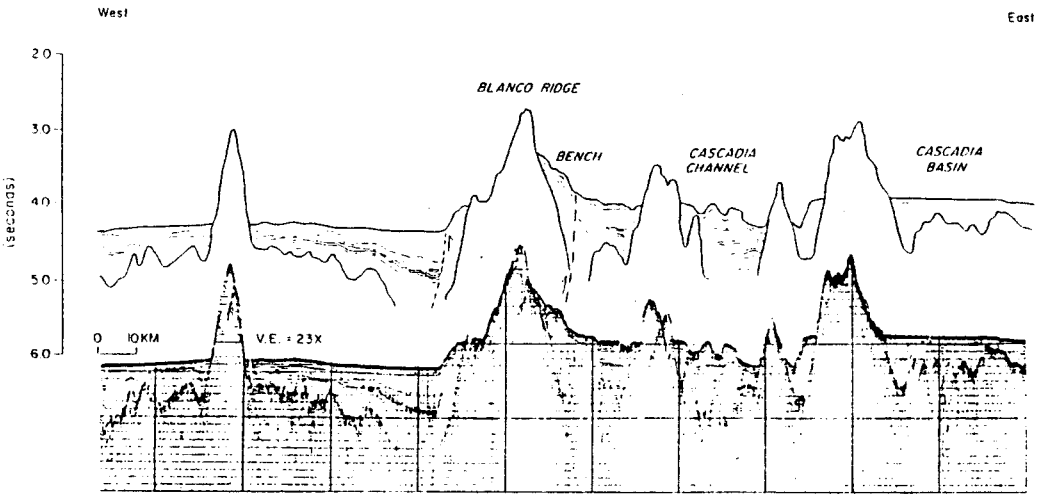
West
East
2.0
3.0
4.0
5.0
6.0
(seconds)
BLANCO RIDGE
BENCH
CASCADIA CHANNEL
CASCADIA BASIN
0 10KM
V.E. = 23X

Figure 5.9

Figure 5.10. Single channel airgun reflection profile collected in 1985 by U.S.G.S. aboard the R/V *S.P. Lee*. Location of profile shown as line F-F' in Figure 5.1, and crosses the ridge at 127° 54'W. The basement of the Blanco Ridge seems to be clearly dipping to the north, illustrated by the set of north dipping reflectors bordering the turbidites, outlined by the arrows in the center of diagram. Draping of the sedimentary sequences over basement and increase in dip of the units as the they approach the fault, suggests uplift of the turbidite sequences is a result of uplift of the underlying Blanco Ridge basement.

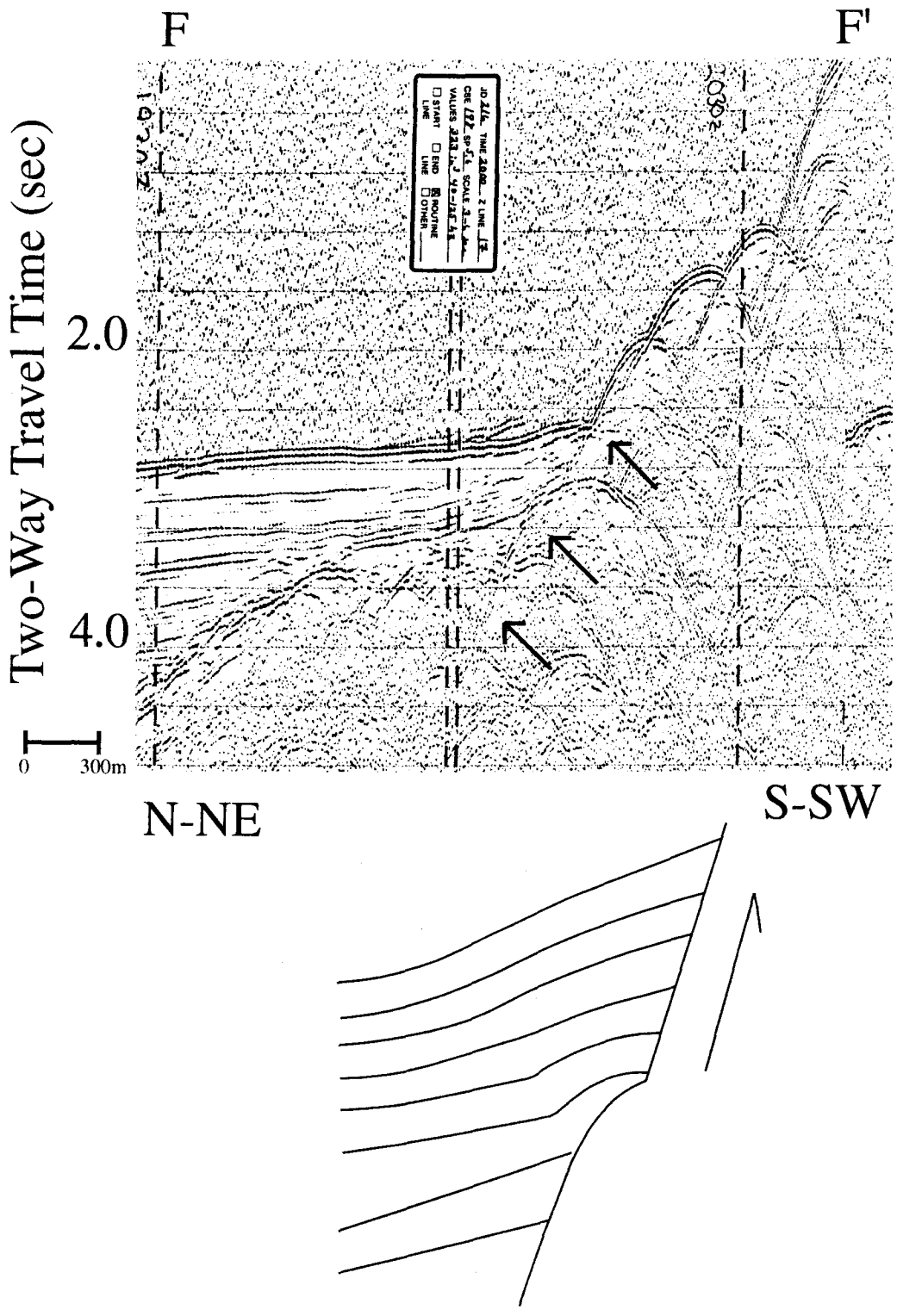


Figure 5.10

with either a vertical or (possibly north dipping) dip-slip fault apparent at the base of the turbidite bench.

The 1985 survey resulted in only one profile that cut across the active transform fault zone, and was perpendicular to the trend of the Blanco Ridge crossing the ridge near 127° 54'W (Figure 5.10). The reflection profile shows the same uplifted turbidite sequences overlying the northern Blanco Ridge base identified by Ibach (1981), although the uplifted turbidite bench is more subdued in this profile. The basement of the Blanco Ridge seems to be clearly dipping to the north, illustrated by the set of north dipping reflectors bordering the turbidites (outlined by the arrows in the center of Figure 5.2. The active transform plate boundary is not readily apparent in this profile. The draping of the sedimentary sequences over the fault, and increase in dip of the units as the they approach the fault, suggests that uplift of the turbidite sequences is a result of uplift of the underlying Blanco Ridge basement.

## 5.6 Submersible and ATV Observations

During late August and early September of 1994, a cruise sponsored by the National Undersea Research Program aboard the R/V *Laney Chouest* resulted in four deployments of the U.S. Navy's Advanced Tethered Vehicle (ATV), and two deployments of the U.S. Navy's DSV *Turtle*, four of which were at sites along the Blanco Ridge (Figures 5.2 and 5.3). The dives on the Blanco Ridge resulted in approximately 67 hours of video, 1000 still photographs, 57 rock samples, and 10 sediment cores. In general, the Blanco Ridge is a strongly tectonized feature exposing a mixture of rock types with both crustal and subcrustal affinities (Koski et al., 1994). The upper slopes are partly mantled by sedimentary breccia and loose rock debris; the lower slope on the north

side is draped with sediment, while the southern lower slope is sediment free. There was abundant evidence of mass wasting and slumping observed on the north facing slopes suggesting that active faulting is concentrated on the north flank of the ridge. Although no active venting was observed along the Blanco Ridge, hydrothermally altered and veined basalt samples were obtained from the ridge flank adjacent to the Gorda Depression. Rock samples obtained from shoaler parts of the ridge to the west of the Gorda Depression include gabbro and basalt with greenschist facies mineral assemblages (Koski et al., 1994).

To obtain the submersible's approximate location, three methods were used: 1) ATV/submersible depth in comparison to bathymetry, 2) ATV/submersible locations relative to GPS ship locations using slant range, and 3) ATV/submersible heading and sonar which gave information on direction to, and steepness of, nearby terrain. Thus vehicle locations on the seafloor are probably good to only about 200 m.

### *5.6.1 Blanco Ridge Geology - Site 1*

Figure 5.11 shows the tracklines, bathymetry, and geologic interpretation of the first ATV dive (Dives 1A and 1B) of the 1994 cruise done along the northwestern wall of the Gorda Depression. Table 5.3 lists the sample locations and petrology of the samples taken along the track. Prior to the field work performed on the *Laney Chouest*, the only samples to have been recovered from the Blanco Ridge were a suite of gabbros, diabases, basalts (greenstones), and greenstone breccias dredged in 1985 from this portion of the ridge adjacent to the Gorda Depression (Hart *et al.*, 1990). All samples found during the 1985 survey had been hydrothermally altered under greenschist conditions, with multistage fragmentation, brecciation, and vein-filling mineral precipitation (> 500°C

Figure 5.11. Seafloor survey site 1 bathymetry (top), submersible tracklines (white and grey lines), sample locations and their petrology, and observed geologic structure. Location of survey site shown on Figure 5.3.

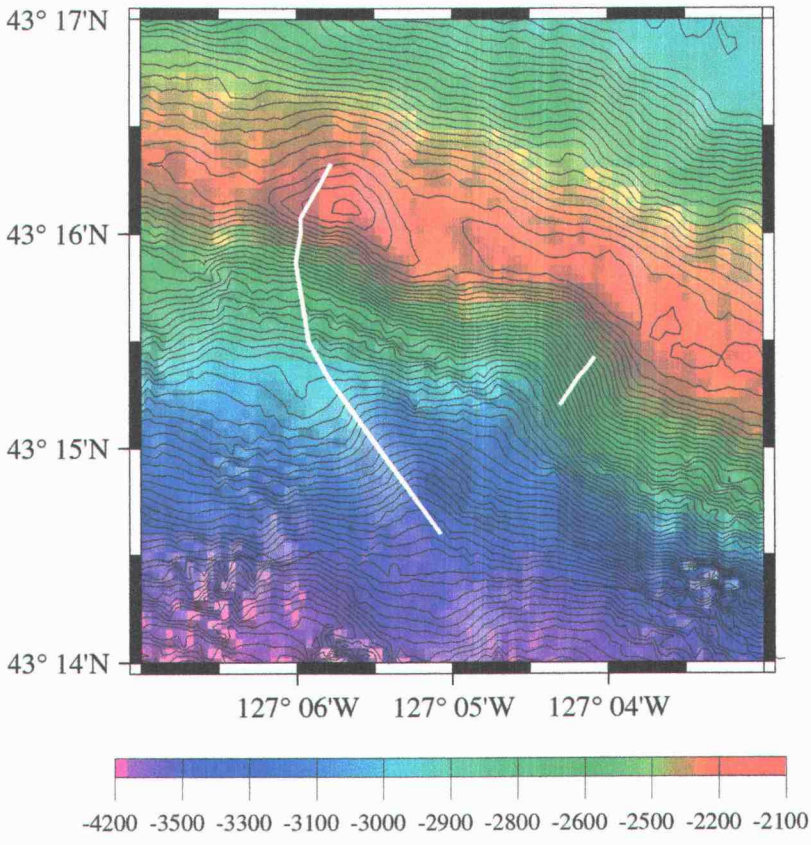
43° 17'N
43° 16'N
43° 15'N
43° 14'N
127° 06'W
127° 05'W
127° 04'W
-4200 -3500 -3300 -3100 -3000 -2900 -2800 -2600 -2500 -2200 -2100

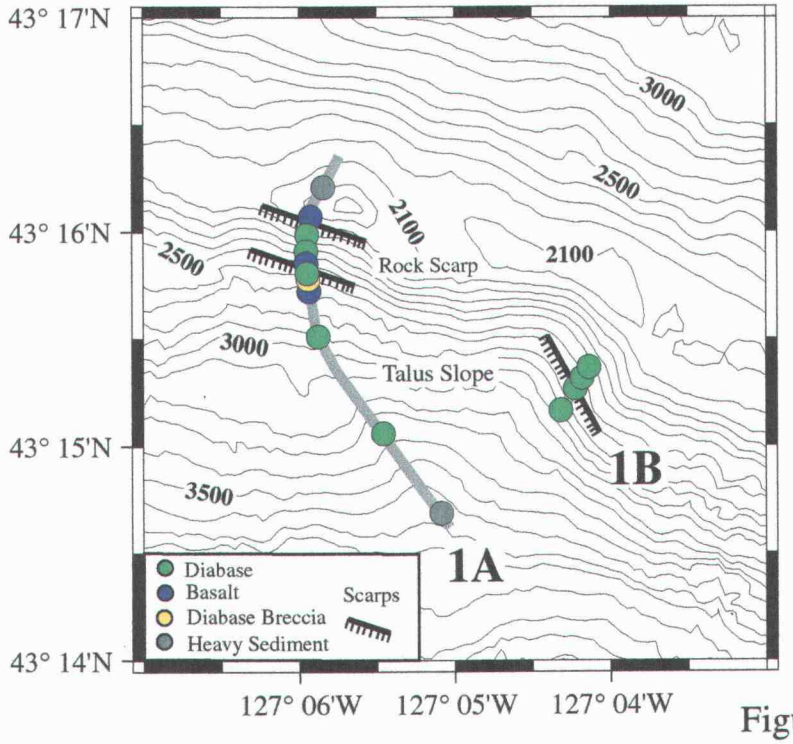
43° 17'N
43° 16'N
43° 15'N
43° 14'N
127° 06'W
127° 05'W
127° 04'W
3000
2500
2100
2500
2100
Rock Scarp
3000
Talus Slope
1B
3500
1A
Diabase
Basalt
Diabase Breccia
Heavy Sediment
Scarps

Figure 5.11

**TABLE 5.3: Dives 1A and 1B: Site 1 Gorda Depression: Sample Locations, Depths, and Petrologic Description - 08/27/94**

| Sample | Time UTM | Location Lat(°,') | Lon(°,') | Depth (meters) | Descrip. | Geologic Setting |
|---|---|---|---|---|---|---|
| | Dive 1A: Gorda Depression | | | | | |
| 1 | 23:20 | 43 15.04 | -127 05.02 | 3125 | Diabase | Talus block from Gorda Dp, BR base |
| 2 | 00:43 | 43 15.55 | -127 05.90 | 2954 | Diabase | Talus block moderate south slope BR |
| 3 | 01:07 | 43 15.71 | -127 05.95 | 2884 | Basalt | Block from talus pile, light sediment |
| 4 | 01:22 | 43 15.75 | -127 05.96 | 2841 | Diabase | Talus block, moderate slope |
| 5 | 01:55 | 43 15.76 | -127 05.96 | 2769 | Dia. Brec. | Talus block on steep slope |
| 6 | 02:17 | 43 15.77 | -127 05.96 | 2640 | Diabase | Talus block at base of steep scarp |
| 7 | 02:31 | 43 15.77 | -127 05.96 | 2613 | Diabase | Talus block up steep scarp |
| 8 | 02:48 | 43 15.82 | -127 05.97 | 2540 | Basalt | Debris from base of steep outcrop |
| 9 | 03:01 | 43 15.89 | -127 05.98 | 2485 | Diabase | In situ block from steep scarp |
| 10 | 03:13 | 43 15.91 | -127 05.98 | 2470 | Diabase | In situ block from steep scarp |
| 11 | 03:51 | 43 15.93 | -127 05.98 | 2265 | Diabase | Talus block along steep scarp |
| 12 | 04:00 | 43 15.95 | -127 05.98 | 2241 | Diabase | In situ block from steep scarp |
| 13 | 04:12 | 43 15.96 | -127 05.98 | 2213 | Diabase | In situ block from sheared scarp face |
| 14 | 04:22 | 43 15.97 | -127 05.98 | 2183 | Diabase | In situ block from sheared scarp face |
| 15 | 04:36 | 43 16.08 | -127 05.96 | 2155 | Basalt | Talus from debris flow on scarp |
| 16 | 05:03 | 43 16.22 | -127 05.85 | 2147 | Lost | Pillow shape sample, ridge summit |
| ---------- Transit to new survey site downslope Blanco Ridge ---------- | | | | | | |
| | Dive 1B: Gorda Depression | | | | | |
| 17 | 14:38 | 43 15.13 | -127 04.32 | 3168 | Diabase | Talus block from flow on steep slope |
| 18 | 15:15 | 43 15.21 | -127 04.25 | 2997 | Diabase | In situ block, fractured scarp face |
| 19 | 15:38 | 43 15.31 | -127 04.22 | 2894 | Diabase | In situ block, fractured scarp face |
| 20 | 16:05 | 43 15.40 | -127 04.12 | 2817 | Diabase | In situ block, fractured scarp face |

sulfides, 350° - 500° C carbonates and zeolites, < 200°C quartz-chert) accompanying hydrothermal activity.

The ATV Dive 1A at site 1 started near the base of the Blanco Ridge (depth = 3548 m) along the northwestern wall of the Gorda Depression, and progressed up to the ridge summit (depth = 2147m). The base of the ridge within the Gorda Depression itself is heavily sedimented, but changed to a talus slope of basalt and diabase breccias after ~600 m climb up from the basin (Figure 5.11 and Table 5.3). The ATV track then progressed northwestward climbing another ~300 m (D = 2640 m) until reaching a steep (~60°) scarp face which was an outcrop of highly jointed and fractured diabase with very-light sediment cover. The diabase appeared to have originated from fracture-bounded dikes within the scarp. Basalt was present in places, but when sampled, appeared to be talus blocks lying on the scarp rather than from an outcrop of the scarp itself. The steep, massive, highly-fractured nature of the scarp face suggests that it is an expression of the active transtensional strike-slip fault boundary of the Gorda Depression pull-apart basin. The scarp continued for ~500 m (D = 2155 m), changing abruptly to a more gentle southwest dipping sediment-covered slope. The slope was sediment covered to the Blanco Ridge. No outcrops were apparent in the sediment, but an angular basalt cobble was sampled near the top of the ridge (D = 2147 m). Ten hours later, a short ATV survey (Dive 1B) was conducted about 2 km to the east, once again along the south-facing Blanco Ridge wall. As before, a steep highly-fractured scarp face composed of diabase was encountered. Veins of white material were observed (and sampled) within the brecciated diabase. Petrographic analysis showed two generations of veining; the first veins are narrow and composed of fibrous amphibole. The second are larger, more extensive, and lower temperature carbonate veins.

*5.6.2 Site 2*

Figure 5.12 shows the trackline, bathymetry, and geologic interpretation of ATV dives at the second site along the south-central portion of the Blanco Ridge. The sample locations, depths, and petrology are summarized in Table 5.4. The dive was broken into two portions. Dive 2A covered the north-northeast trending abyssal hills south of the active transform fault trace, and Dive 2B targeted the Blanco Ridge. The Blanco Ridge portion of the dive was selected at this particular location because of a possible small (< 1 km) step in the fault trace apparent from the bathymetry (Figure 5.12).

ATV Dive 2A began at a depth of 2546 m within a heavily sedimented basin. The ATV kept a heading of ~315°, thus traversing perpendicular to the trend of the ridge-forming abyssal hills. The northeast-trending abyssal hills form a series of *én echelon* ridges that bend to the east as they approach the transform fault (Figure 5.1). This bending or folding of the ridges is probably a result of drag due to resistance of motion along the strike-slip fault. The dive crossed three ridges. At the base of each were basalt talus fields that changed to massive basalt scarps (sloping southeast ~ 45°) farther upslope. The top of each ridge, like the basins between them, were heavily sedimented with no outcrops observable. The ridges reached depths between 2400 - 2425 m, or about 100 - 150 m above the basins. The basalts sampled at each basal scarp were highly fractured pillows composed of slightly altered porphyritic basalts with phenocrysts of plagioclase and olivine, and some carbonate veining. The scarps are interpreted here as recently active faults since they have little sediment cover and cut the youngest seafloor sediment. The faults are probably reactivated normal faults present in the Pacific plate crust from relict Gorda Ridge spreading fabric that slip in conjunction with motion along the transform fault. It is not possible to directly estimate the sense of motion on these faults since the dive data are inconclusive, and there is no seismic-reflection data

Figure 5.12. Seafloor survey site 2 bathymetry (top), submersible tracklines (white and grey lines), sample locations and their petrology, and observed geologic structure. Location of survey site shown on Figure 5.3.

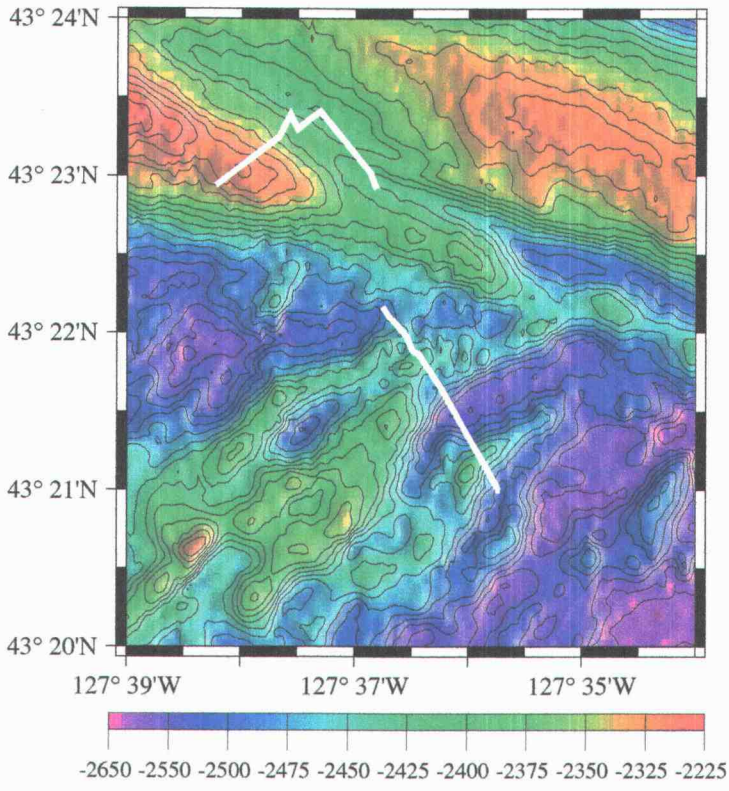
43° 24'N
43° 23'N
43° 22'N
43° 21'N
43° 20'N
127° 39'W
127° 37'W
127° 35'W
-2650 -2550 -2500 -2475 -2450 -2425 -2400 -2375 -2350 -2325 -2225

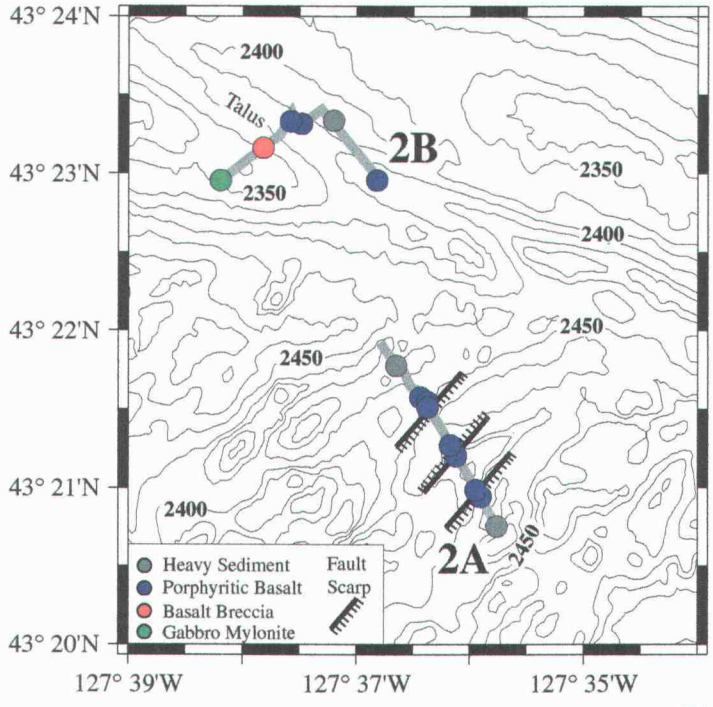
43° 24'N
43° 23'N
43° 22'N
43° 21'N
43° 20'N
127° 39'W
127° 37'W
127° 35'W
2400
Talus
2350
2B
2350
2400
2450
2450
2400
2A
2450
Heavy Sediment
Porphyritic Basalt
Basalt Breccia
Gabbro Mylonite
Fault
Scarp

Figure 5.12

**TABLE 5.4 Dives 2A and 2B: Site 2 Abyssal Hills and East Blanco Ridge Sample Locations, Depths, and Petrologic Description - 08/30/94**

| Sample | Time UTM | Location Lat(°,') | Lon(°,') | Depth (meters) | Description | Geologic Setting |
|---|---|---|---|---|---|---|
| | Dive 2A: Abyssal Hills South of Blanco Ridge | | | | | |
| 1 | 22:03 | 43 20.85 | -127 36.01 | 2546 | Porphy. Basalt | Talus block from slope base |
| 2 | 22:17 | 43 20.95 | -127 36.05 | 2470 | Porphy. Basalt | In situ block, fractured scarp face |
| 3 | 01:20 | 43 21.13 | -127 36.24 | 2543 | Porphy. Basalt | Pillow basalt, fractured scarp face |
| 4 | 02:45 | 43 21.22 | -127 36.30 | 2482 | Porphy. Basalt | In situ block, fractured scarp face |
| 5 | 02:49 | 43 21.48 | -127 36.45 | 2482 | Porphy. Basalt | In situ block, fault scarp face |
| 6 | 03:15 | 43 21.50 | -127 36.49 | 2445 | Porphy. Basalt | In situ block, top of fault scarp |
| 7 | 03:38 | 43 21.55 | -127 36.52 | 2423 | Porphy. Basalt | Pillow basalt, top of fault scarp |
| ---------- Transit north to new survey site, base of Blanco Ridge ---------- | | | | | | |
| | Dive 2B: East Blanco Ridge | | | | | |
| 8 | 18:54 | 43 22.94 | -127 36.82 | 2377 | Porphy. Basalt | Talus block, Blanco Ridge base |
| 9 | 22:33 | 43 23.30 | -127 37.50 | 2375 | Porphy. Basalt | Talus block, Blanco Ridge base |
| 10 | 22:45 | 43 23.29 | -127 37.56 | 2375 | Porphy. Basalt | Talus block, Blanco Ridge base |
| 11 | 23:33 | 43 23.20 | -127 37.66 | 2363 | Basalt Breccia | Rock fragment near BR summit |
| 12 | 01:23 | 43 22.94 | -127 38.22 | 2302 | Gabbro Mylo. | Rock fragment from BR summit |

available from this locale. However, since the abyssal ridges bend more easterly near the transform fault, these may be old Pacific-plate normal faults occurring in response to uplift along the Blanco Ridge.

Dive 2B began in a saddle (depth ~2400 m) between two small segments of the Blanco Ridge (Figure 5.12). The dive tracked oblique to the saddle, heading ~315°, before changing course to ~225° to climb up the north face to the summit of the southwestern ridge segment. The saddle was heavily sedimented and showed no indication of a basement outcrop. The base of the southwest ridge segment (depth ~2377) had an extensive apron of porphyritic basalt talus blocks ranging in size from ~10 to 20 cm. As at the abyssal hills to the south, the basalts had large phenocrysts of plagioclase and olivine with some carbonate veining. The talus continued upslope to a depth of 2315 m (~ 62 m), whereupon the ridge became covered with a basalt gravel pavement with little or no sediment cover. Locally, outcrops of porphyritic basalt were observed (and sampled) protruding through the pavement. At depths of 2360 and 2300 m along the northern ridge face, out of place rock fragments of a basalt breccia and a recrystallized mylonite block were sampled, respectively. The mylonite is a fine-grained, foliated, and recrystallized gabbro with late-stage chlorite veins that cut across the foliation. This was the only mylonite to be found among the petrologic samples collected during the 1994 dive series. The north face of this ridge segment remained covered with gravel-sized pavement until the ridge crest (depth = 2290 m), where the sediment cover became heavy once again.

*5.6.3 Site 3*

Figure 5.13 shows the trackline, bathymetry, and geologic interpretation of ATV dives 3A and 3B at site 3 along a north central portion of the Blanco Ridge. The sample

locations, depths, and petrology are summarized in Table 5.5 The dive track was chosen here because it traverses the north side of the ridge along an apparent slump scar that cuts the ridge. Thus this track resulted in a good compositional view of the Blanco Ridge from base to summit. The slump block appears to be the NW-SE trending linear ridge northeast of the slump scar (marked with an "S" Figure 5.1). The distance between the scar and debris suggests that the slump scar is on the Pacific plate, the block is on the Juan de Fuca plate, and the two have been moved apart by motion along the transform. The horizontal distance between the western edge of the slump scar and block is ~ 25 km, and with a long term plate motion rate of ~ 5.5 cm/yr across the BTFZ, suggests that the slump occurred ~ 454 ka. This age helps to explain the large amount of sediment that covers the slump scar basin. Also, it would then appear that the ATV track line up the steep scarp face traversed Pacific plate crust.

Dive 3A began within thick sediment cover at base of the Blanco Ridge (depth of 2961 m). The ATV heading of 180° - 190° took the vehicle over a low ridge formed at the edge of the slump scar, then into the basin scoured at base of the scar. This low ridge is the surface expression of the BR parallel lineation identified from bathymetry in Figure 5.1. We speculate that the lineation may be a dip-slip fault that has exhibited displacement since, and perhaps prior to, the time of the slump. Hence the formation of a ridge at the base of the slump scar. Unfortunately, sediment cover was thick throughout this section of the dive, and no outcrops or rock fragments were observed. At the base of the headwall of the scar (depth = 2939 m), porphyritic basalt, diabase, and gabbro (heterolithic) breccia were sampled from a steep, heavily sedimented scarp face that continued to a depth of 2436 m (~500 m), where the ridge became a near-vertical rock scarp. The scarp face is a massive wall of highly fractured gabbro. Diabase and basalt talus blocks were sampled from two locations on the scarp face, but the two samples

Figure 5.13. Seafloor survey site 3 bathymetry (top), submersible tracklines (white and grey lines), sample locations and their petrology, and observed geologic structure. Location of survey site shown on Figure 5.2.

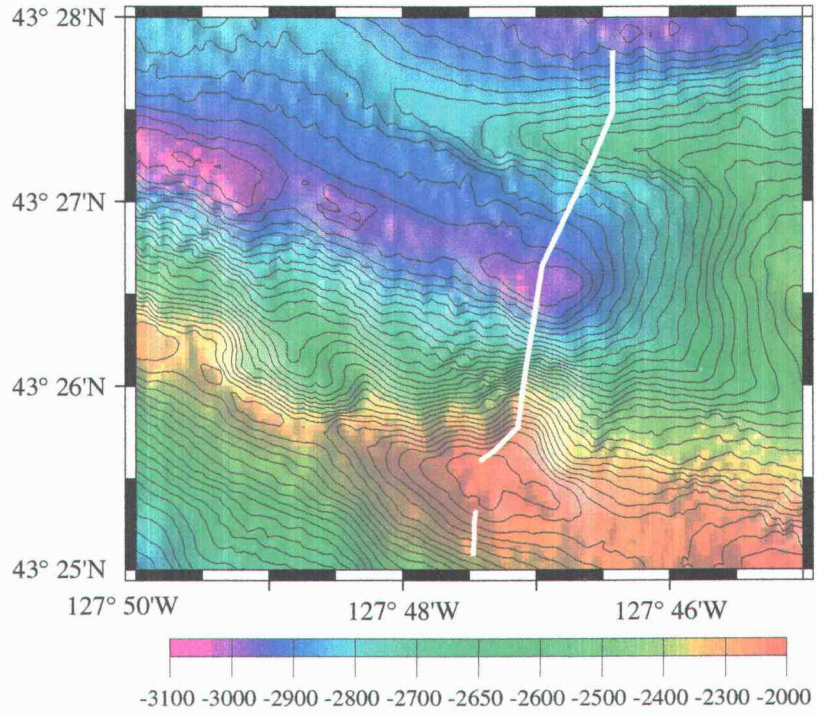
43° 28'N
43° 27'N
43° 26'N
43° 25'N
127° 50'W
127° 48'W
127° 46'W
-3100 -3000 -2900 -2800 -2700 -2650 -2600 -2500 -2400 -2300 -2000

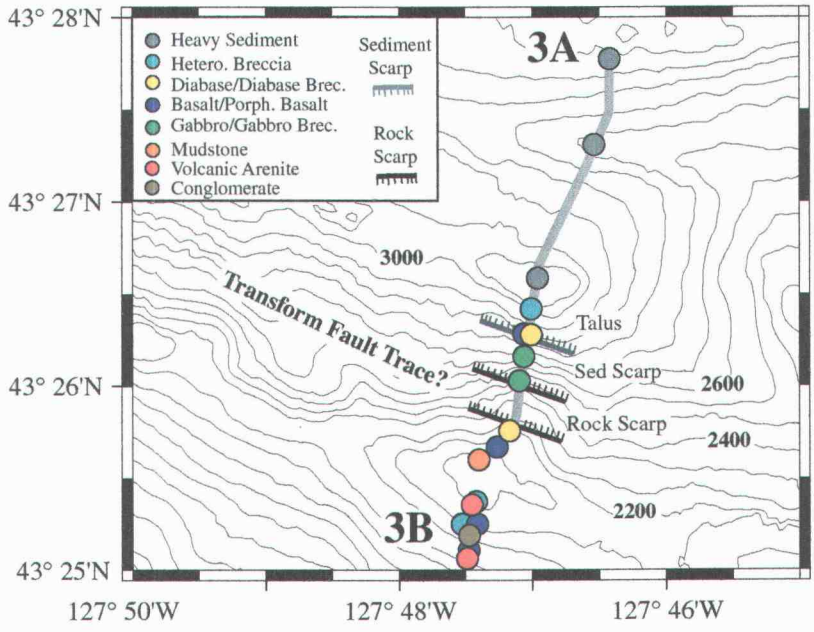
Heavy Sediment
Hetero. Breccia
Diabase/Diabase Brec.
Basalt/Porph. Basalt
Gabbro/Gabbro Brec.
Mudstone
Volcanic Arenite
Conglomerate
Sediment Scarp
Rock Scarp
3A
3B
3000
2600
2400
2200
Transform Fault Trace?
Talus
Sed Scarp
Rock Scarp
43° 28'N
43° 27'N
43° 26'N
43° 25'N
127° 50'W
127° 48'W
127° 46'W

Figure 5.13

**TABLE 5.5 Dives 3A and 3B: Site 3 central Blanco Ridge. Sample Locations, Depths, and Petrologic Description - 09/01/94**

| Sample | Time UTM | Location Lat(°,') | Lon(°,') | Depth (meters) | Description | Geologic Setting |
|---|---|---|---|---|---|---|
| | Dive 3A Slump Scar - north flank Blanco Ridge | | | | | |
| 1 | 22:04 | 43 26.55 | -127 47.01 | 2939 | Hetero. Breccia | Talus debris base of BR |
| 2 | 01:00 | 43 26.39 | -127 47.01 | 2927 | Diabase Breccia | Rock fragment off sed. scarp |
| 3 | 01:04 | 43 26.38 | -127 47.01 | 2927 | Basalt | Rock fragment off sed. scarp |
| 4 | 01:25 | 43 26.34 | -127 47.02 | 2866 | Hetero. Breccia | Talus block, steep sed. scarp |
| 5 | 02:43 | 43 26.21 | -127 47.10 | 2686 | Gabbro Breccia | Talus block, steep sed. scarp |
| 6 | 03:16 | 43 26.02 | -127 47.11 | 2436 | Gabbro | In situ block, vertical scarp face |
| 7 | 03:42 | 43 25.84 | -127 47.12 | 2334 | Diabase | Talus block from debris flow |
| 8 | 03:56 | 43 25.75 | -127 47.26 | 2299 | Basalt | Rock fragment, flank of BR |
| 9 | 04:46 | 43 25.62 | -127 47.41 | 2110 | Mudstone | In situ block from BR summit |
| ---------- Transit south to new survey site, south flank of Blanco Ridge ---------- | | | | | | |
| | Dive 3B south flank Blanco Ridge | | | | | |
| 9 | 07:43 | 43 25.08 | -127 47.47 | 2302 | Volcanic Arenite | Rock fragment, south BR slope |
| 10 | 07:56 | 43 25.10 | -127 47.48 | 2290 | Porphy. Basalt | Talus block, south slope BR |
| 11 | 08:07 | 43 25.21 | -127 47.47 | 2375 | Conglomerate | Talus block, south slope BR |
| 12 | 08:42 | 43 25.26 | -127 47.47 | 2220 | Basalt Breccia | Talus block, south slope BR |
| 13 | 09:11 | 43 25.26 | -127 47.46 | 2159 | Porphy. Basalt | Rock fragment near BR summit |
| 14 | 09:30 | 43 25.39 | -127 47.46 | 2128 | Volcanic Arenite | Rock fragment near BR summit |
| 15 | 09:41 | 43 25.45 | -127 47.45 | 2128 | Basalt Breccia | Large block at BR summit |

clearly collected from outcrops along the scarp face were gabbro and gabbro breccia. The gabbro shows quartz and carbonate veining that took place prior to brecciation. No slickensides or other micro-structural features were observed so it is not clear whether the scarp seen here is the slide slope or the active transform trace. The steep scarp is present up to a depth of 2360 m (~ 80 m high). Once the crest of the scarp was reached, the ridge slope shallowed considerably (still dipping N-NE) and became mantled by light sediment cover and a gravel pavement to the Blanco Ridge summit. Fragmented blocks of basalt and diabase were sampled in this region, likely reflecting basement composition beneath the sediment. The Blanco Ridge summit was reached at a depth of 2110 m, and a mudstone was sampled.

The ATV was then moved south to make Dive 3B; a brief traverse up the south side of the Blanco Ridge (Figure 5.13). Starting at a depth of 2302 m, a volcanic arenite cobble was collected from a light sediment/gravel pavement seafloor dipping steeply to the south. As the ATV progressed upslope, porphyritic basalt and basalt breccia blocks were sampled as random fragments within the gravel pavement, again likely reflecting basement composition along this section of the ridge. Farther upslope samples of conglomerate (at a depth of 2277 m) and volcanic arenite (at a depth of 2128 m) were collected along the south face. The conglomerate is composed of rounded calcarious-mudstone clasts within a matrix containing planktonic foraminifera, while the arenite is composed of basalt fragments and palagonite clasts (Alicia Davis, Pers. Com.). Both the conglomerate and arenite were probably formed locally. The conglomerate and arenite samples were taken from what appeared to be a debris flow originating at the ridge summit. The gravel pavement and light sediment cover continued along the south face of the ridge until the dive was terminated near the summit at a depth of 2128 m.

*5.6.4 Site 4*

The bathymetry, trackline, and geologic interpretation of the submersible Dive 4 at site 4 using the U.S. Navy DSRV *Turtle* is shown in Figure 5.14. The approximate sample location, depths, and petrology are summarized in Table 5.6 This location was selected to provide a view of the geologic section along the south-facing ridge scarp, and because it is the shoalest portion of the Blanco Ridge. Because the submersible could not be tracked precisely, a constant effort was maintained throughout the dive to traverse the steepest slope so as to ensure the Blanco Ridge summit was reached. The dive began at a depth of 2349 m along the steeply dipping south face of the Blanco Ridge. The ridge here has a surface of gravel pavement with little or no sediment cover. The first sample, collected when the submersible initially reached the seafloor, was a brecciated gabbro block (~ 10 cm) from a pile of talus along the ridge slope. The ridge surface remained a gravel pavement with ubiquitous talus blocks as the sub climbed upslope to a depth of 2281 m where another gabbro talus block was sampled. This gabbro had oriented, plagioclase-rich zones suggestive of a cumulate origin. The submersible climbed to the break of slope at the ridge summit (depth of 2138 m), and obtained another gabbro talus block sample. The gabbro was undeformed, showing no signs of brecciation. The sub changed to a heading of 090° to remain along the ridge peak, and crossed a set of large fractures oriented approximately parallel to the strike of the transform (depth = 2141 m). Within these fractures a sample of brecciated cumulate gabbro was obtained. This deformed gabbro was characterized by variably rounded clasts within a granulated matrix. The submersible continued on an east-southeast heading along the ridge peak, following the sonar returns towards the steepest slope. The ridge surface remained a gravel pavement with little or no sediment, with widely distributed talus blocks (~ 10 - 100 cm in size). Along this portion of the ridge summit, there were many crabs, starfish,

Figure 5.14. Seafloor survey site 4 bathymetry (top), submersible tracklines (white and grey lines), sample locations and their petrology, and observed geologic structure. Location of survey site shown on Figure 5.2.

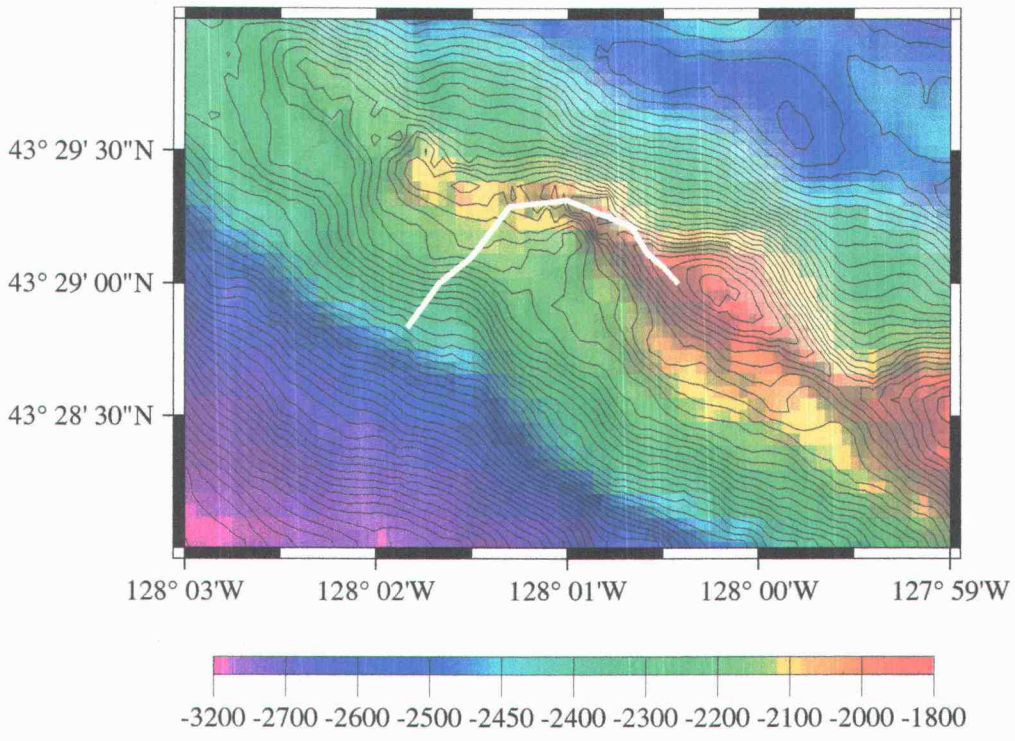
43° 29' 30"N
43° 29' 00"N
43° 28' 30"N
128° 03'W
128° 02'W
128° 01'W
128° 00'W
127° 59'W
-3200 -2700 -2600 -2500 -2450 -2400 -2300 -2200 -2100 -2000 -1800

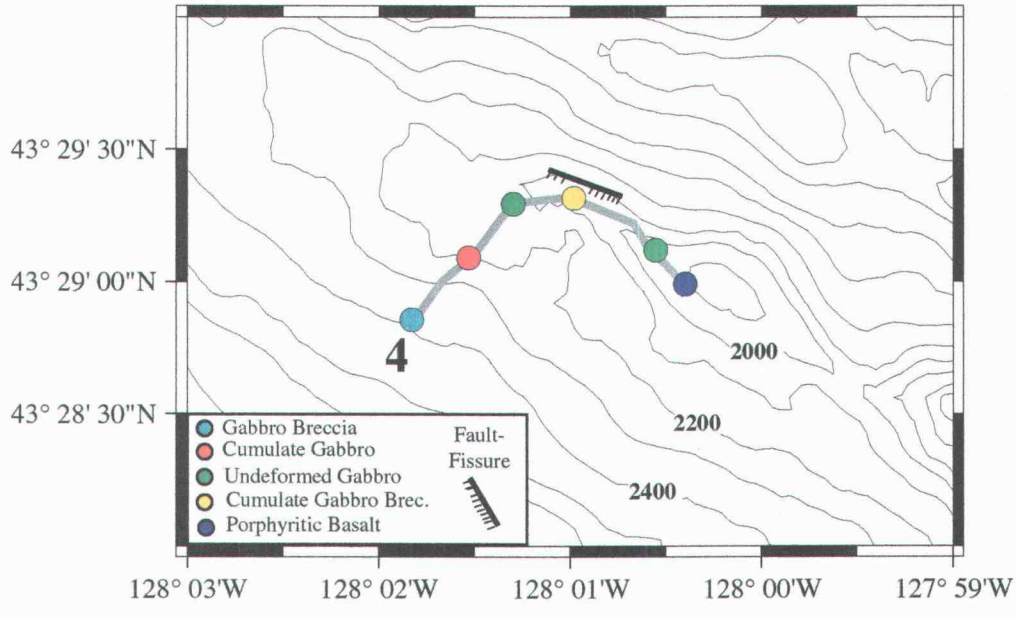
43° 29' 30"N
43° 29' 00"N
43° 28' 30"N
4
2000
2200
2400
Gabbro Breccia
Cumulate Gabbro
Undeformed Gabbro
Cumulate Gabbro Brec.
Porphyritic Basalt
Fault-
Fissure
128° 03'W
128° 02'W
128° 01'W
128° 00'W
127° 59'W

Figure 5.14

**TABLE 5.6 Dive 4: Site 4 Blanco Ridge South Flank and Summit Sample Locations, Depths, and Petrologic Description - 08/31/94**

| Sample | Time UTM | Location Lat(°,') Lon(°,') | Depth (meters) | Description | Geologic Setting |
|---|---|---|---|---|---|
| | Dive 4: Blanco Ridge South Flank | | | | |
| 1 | 11:55 | 43 28.9 -128 01.9 | 2349 | Brecciated Gabbro | South base of BR talus |
| 2 | 12:52 | 43 29.1 -128 01.5 | 2281 | Cumulate Gabbro | Talus along BR south face |
| 3 | 13:44 | 43 29.3 -128 01.4 | 2138 | Undeformed Gabbro | Talus from ridge top |
| 4 | 14:05 | 43 29.4 -128 01.0 | 2141 | Cumulate Gab. Brec. | In situ block within parallel fractures along ridge peak |
| 5 | 15:25 | 43 29.1 -128 00.7 | 2050 | Undeformed Gabbro | Talus at ridge summit |
| 6 | 16:02 | 43 28.9 -128 00.5 | 1972 | Porphyritic Basalt | Talus block from BR summit |

clams, and rays. Further along the southeast track, another undeformed gabbro was sampled (depth = 2050 m) from an outcrop along the ridge summit. The dive ended along the top of the Blanco Ridge at a depth 1972 m (Figure 5.14), where a porphyritic basalt block was sampled from a small talus pile on top of the gravel pavement. The dive ended a few hundred meters southwest of the shaolest point of the ridge (depth ~ 1870m). So the basalt talus block was likely derived, through fracturing and seismic shaking, from an outcrop near the ridge summit.

## 5.7 Sea-Surface Gravity and Magnetics

A sea-surface magnetic and gravity profile collected in 1988 across the Blanco Ridge was obtained from the National Geophysical Data Center (Figure 5.15). The profile crosses the ridge at 128° 10'W, and is roughly orthogonal to the strike of the transform. The profile also happens to cross the Blanco Ridge where the beginning of magnetic isochron 3 is juxtaposed in both the Juan de Fuca and Pacific plates. Thus the plate ages (~ 4.2 Ma) and magnetic polarity should roughly be equal at this longitude on either side of the transform. The dashed line on the profiles in Figure 5.15 represents the location of the transform fault trace estimated from bathymetry and seafloor mapping efforts. The magnetic profile (representing total field minus reference) over the Blanco Ridge shows a distinct boundary across the fault zone, with magnetization increasing on the south (Pacific plate) side. This profile might be generated by greater relative basement uplift of the Blanco Ridge on the Pacific plate side, with the magnetic lows at the BR north and south flanks caused by the thick (> 2 km) turbidite sequences. A magnetic anomaly map (total field minus reference) compiled by Riddihough (1984) shows a 200 nT anomaly at the BR as well, and also indicates that the anomaly is parallel to the BR south flank.

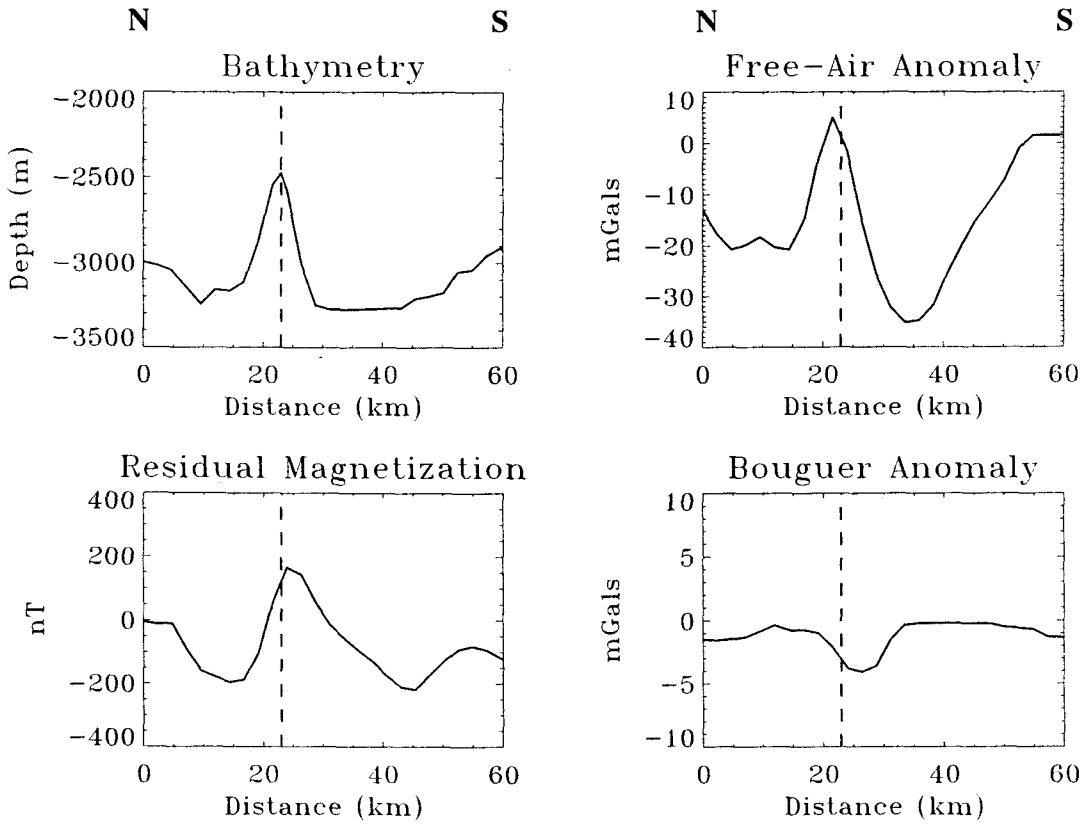


Figure 5.15. North-south profile of bathymetry (top left), free-air sea-surface gravity (top right), magnetic profile (bottom left), and Bouguer anomaly (bottom right) across the Blanco Ridge. Location of profiles shown as line G-G' in Figure 5.1. Data from profile collected by the National Oceanic and Atmospheric Administration in 1988. Dashed line in each profile represents the location of the active transform fault estimated from bathymetry and seafloor mapping efforts. Magnetic profile represents observed total field minus 1985 International Geomagnetic Reference Field. Bouguer anomaly estimated free-air by removing bathymetric and water column effects.

The free-air and Bouguer anomalies are also shown in Figure 5.15. The sea-surface free-air gravity data along this profile was compiled from NGDC. The free-air anomaly indicates a high over the ridge and a pronounced low along the BR south flank. A free-air anomaly map compiled by Riddihough et al. (1982) shows the same anomaly shape, and indicates that the high and low anomalies parallel the ridge crest and ridge south flank, respectively. The Bouguer anomaly was then estimated from free-air gravity by removing the effects of bathymetry and the water column along the profile. Densities of 2.7 gm-cm$^{-3}$ (basalt) and 1.03 gm-cm$^{-3}$ (water) were used. Since the ocean plate ages on either side of the transform at this longitude are roughly equal, gravity calculations were not corrected for lithospheric density contrasts across the fault. The estimated Bouguer anomaly indicates a relatively greater negative anomaly (mass deficit) under the south side of the BR, and smaller negative anomalies along the north and south BR flanks. The negative anomalies on the flanks are probably due to the thick, less dense turbidite sequences. The larger negative anomaly under the ridge is possibly due to a narrow (~ 5 km) low-density zone beneath the BR, which seems to be centered along the Pacific plate (south) side of the transform. A forward model of the free-air anomaly was estimated using a simple two-dimensional crustal model. The model indicates that, assuming a 10 km thick crust (constrained by earthquake focal depths), the gravity anomaly could be produced by 1.5 km thick ($\rho$ = 2.45 gm-cm$^{-3}$) sediment wedges along the BR flanks, and a 5 km wide, 3 km thick, and 2 km deep low-density ($\rho$ = 2.2 gm-cm$^{3}$) body beneath the BR itself. However, the model is certainly non-unique.

## 5.8 Summary and Conclusions

The acoustic locations, fault-parameter information, and slip vector estimates of 43 earthquakes ($M_w > 4$) that occurred along the eastern BTFZ over the last 5 years reveal that the Blanco Ridge is a high-angle, right-lateral strike-slip fault with the Juan de Fuca plate as the hanging wall. The majority of the strike-slip mechanisms indicate a small normal component of slip along the transform, while three events (12, 22, and 35) show a slight reverse component. The majority of the focal mechanism P-axes are nearly horizontal and oriented between 39°-59° to the strike of the BR. Thus the P-axes orientations are near the optimum angle of 45° for the maximum principal stress axis along a fault, suggesting the fault is resistant to shear failure and may exhibit a high shear stress. In comparison, borehole breakout and earthquake focal mechanism information suggest that the maximum principal stress axis along the San Andreas Fault (SAF) are oriented normal to the fault trace (Oppenheimer et al., 1988; Mount and Suppe, 1992). The orthogonal maximum principal stress axes and low observed heat flow along the SAF, led Mount and Suppe (1992) to suggest the entire fault has a low resolved shear stress, or is "weak". Events 4, 14, and 15 cluster at longitude 128° 00'W, and have P-axes oriented closer to normal (175° - 182°) to the BR trend than the other earthquake P-axes, possibly meaning these events reflect a relatively weaker zone along the fault. An estimate of Blanco Ridge earthquake stress drops and direct measurements of seafloor heatflow across the ridge would help to constrain more definitively the level of shear stress along the BR fault .

The clockwise change in Juan de Fuca plate motion that occurred 5 Ma (Wilson, 1993) would tend to cause oblique (NW-SE) compression along the eastern BTFZ. This eastern BTFZ compression orientation is consistent with focal mechanism $\sigma_1$ orientations

presented. A recent study by Pockalny et al. (1997) suggests that the median ridge along the active Clipperton Transform trace is a result of compression due to a series of changes in spreading direction along the East Pacific Rise. Evidence for the compressional origin of the Clipperton Transform Ridge exists in the similarity in appearance of the ridge and and trough (that formed in the Cocos plate) to the flexure of an elastic plate with an endload. It is possible that the Blanco Ridge was formed by uplift in part due to compression across the transform. Indeed, the observed strike-slip mechanisms require oblique maximum compression, and the majority of the earthquake strike-slip vectors are oriented southeast (0° - 9°) of the BR trend. Also, the free-air anomaly profile (upper right Figure 5.15) looks similar to a profile of the deflection of a plate (Pacific) under an endload. Furthermore, assuming a 75 km displacement along the BR and a crustal thickness of 10 km, even a small earthquake dip-slip component (> 8°) is sufficient to expose lower oceanic crustal rocks. It is possible that the component of compression across the eastern BTFZ is resulting in some underthrusting of the Pacific beneath the Juan de Fuca plate. However, it would seem that this compression across the transform would manifest itself in earthquake focal mechanisms with predominantly reverse slip components, rather than the observed dominant normal component. Also, there is not a large age contrast between the two plates that could enhance underthrusting of the Pacific plate, with the Pacific being the same age or younger than the Juan de Fuca for all of the Blanco Ridge east of 128° 20'W.

Brecciated and undeformed basalt, diabase, and gabbro samples were collected at the four submersible survey sites along the Blanco Ridge. Samples collected during the surveys suggest that the Blanco Ridge is comprised of an ocean crustal sequence that has been uplifted and highly fractured. The petrologic samples also appear to show an increase in elevation of the crustal section from east to west along the Blanco Ridge, with

gabbros exposed at a shallower point farther west along the southern (Pacific plate side) of the Blanco Ridge flank. Supporting evidence for BR uplift exists in the presence of sedimentary rocks found at the BR summit, seismic reflection profiles across the BR showing uplift of turbidite sequences along the north and south ridge base, and gravity and magnetics profiles that indicate possible basement uplift and a low-density zone centered on the ridge's Pacific plate side. The existence of a negative Bouguer anomaly over the BR suggests it is not an uncompensated stress-supported feature, but possibly compensated in an Airy fashion by an overthickened crust or a low density body (e.g., serpentinized-peridotite diapir).

The geology and geophysical data presented suggest several possibilities for Blanco Ridge formation. The formation mechanism preferred here is first, uplift achieved partially through strike-slip motion (with a small dip-slip component). Second, the strike-slip faulting may have allowed seawater penetration along the fault into the lower crust and upper mantle, which then enhanced formation and intrusion of a mantle-derived serpentinized-peridotite diapir into the shallow ocean crust causing further uplift along the fault. This is similar to a model proposed by Hekinian et al. (1992) for the Garret Transform . Formation of the diapir involves expansion of the mantle underlying the fracture zone by alteration of peridotite through deep hydrothermal circulation along the transform fault (Bonatti, 1976; 1978). Discrete diapirs along the transform fault might explain the morphology of the Blanco Ridge which appears as a series of lozenge-shaped highs. Although no serpentinized-peridotite was found during these surveys (which may be a sample-density problem), it is a convenient mechanism to account for uplift within a narrow zone along a strike-slip fault where no ridge forming flexural features in the lithosphere are seismogenic.

A model for the composition, structure, and deformation of the Blanco Ridge is now proposed (Figure 5.16) based on the observations presented. The two cross-sections in Figure 5.16 are based on interpretation of the seafloor surveys done at sites 3 and 4, but also represent a synthesis of all data presented. The location of the active fault forming the transform plate boundary is constrained to be along the center of the Blanco Ridge by (1) the lineation at the ridge summit outlined in Figure 5.2, and (2) the mapping of faults and fissures and the ridge summit at sites 3 and 4. The transform fault may form the long, linear basin (notch) along the summit of the Blanco Ridge through brecciation of material along the fault and subsequent removal by ocean currents or mechanical weathering.

The Blanco Ridge shallows to the west, and based on the observations at sites 3 and 4, the deep ocean crustal rocks appear to shoal to the west as well (Figure 5.16). This may mean that a serpentinized-peridotite diapir, if it exists, also becomes progressively more shallow westward along the ridge. This may be a result of penetration of the serpentinized peridotite into the shallow portions of the crust, and/or the component of tectonic uplift. The result would be to force the deep oceanic-crustal rocks, at least on the Pacific plate side, closer to the seafloor surface before the ridge ends at the south end of Cascadia Depression. This is seemingly supported by the finding of diabase and basalt sections overlying a gabbro section in the Pacific crust at site 3, while predominantly gabbros (and one basalt sample at the summit) were found along the south (Pacific) side of the ridge at site 4 (Figures 5.12 and 5.16). The younger Juan de Fuca plate may have a full ocean crust section at these sites. In contrast, the cross section of Blanco Ridge crust at site 1 has basalt and diabase exposed along the scarp face, but no deeper crustal rocks. It could be that ridge uplift is reduced here since the normal faulting regime (and elevated

Figure 5.16 Proposed model for the composition, structure, and deformation history of the Blanco Ridge. Cross sections are meant to reflect interpretation of seafloor surveys from site 3 (right) and site 4 (left), but are a synthesis of all data presented here. The less dense serpentinized-peridotite, formed through alteration of mantle material by deep hydrothermal circulation, causes uplift of ocean crust immediately adjacent to the active transform trace.

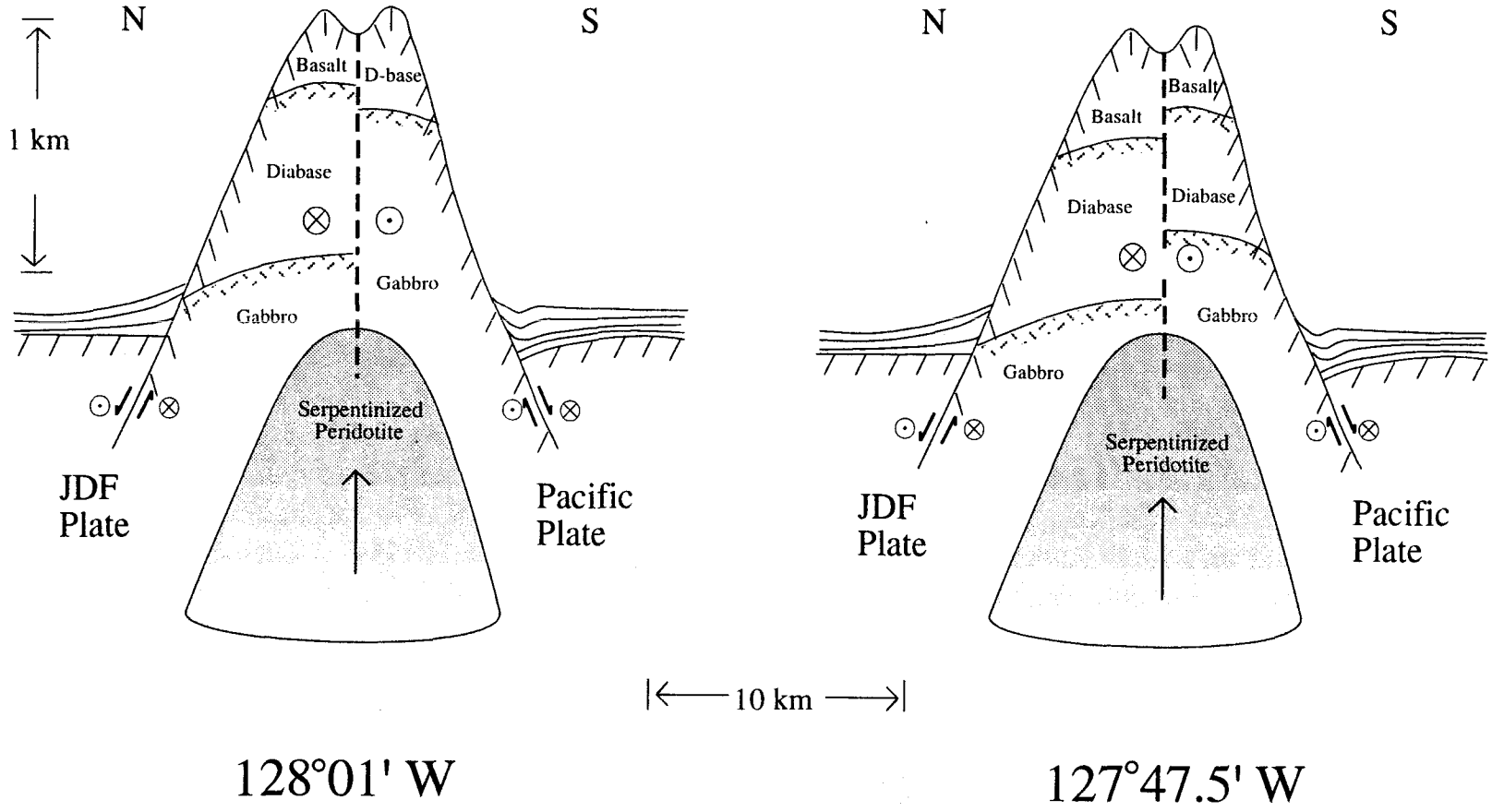
N
S
1 km
Basalt
D-base
Diabase
Gabbro
Gabbro
Serpentinized
Peridotite
JDF
Plate
Pacific
Plate
N
S
Basalt
Basalt
Diabase
Diabase
Gabbro
Gabbro
Serpentinized
Peridotite
JDF
Plate
Pacific
Plate
10 km
128°01' W
127°47.5' W

Figure 5.16

crustal isotherms) of the Gorda Depression may inhibit the growth of a serpentinite diapir.

NW-SE lineations along the base of the Blanco Ridge, just to the north and south of the ridge (small downward arrows in figgure 5.16; white arrows in Figure 5.1), are interpreted here as strike-slip faults with a normal slip component (dip-slip faults at base of ridge in Figure 5.16), which is consistent with the focal mechanism data.. The faults may have initiated in the Juan de Fuca and Pacific plates as diapiric normal faults in response to the Blanco Ridge serpentinite uplift, but because of regional right-lateral shear, they became elongate and exhibit predominantly strike-slip motion. The NE-SW trending abyssal ridges south of the Blanco Ridge appear to bend more easterly near the transform fault. Thus they may be normal faults reactivated from a spreading fabric within the Pacific plate. These normal faults are slipping in response to uplift along the Blanco Ridge, and bending due to strike-slip motion along the transform.

Oblique compression along the eastern BTFZ is not necessarily at odds with the Blanco Ridge model presented. Regional oblique compression is required to produce the observed strike-slip earthquakes, and could still allow for a small component of normal slip along the transform and an environment of diapiric uplift along the Blanco Ridge. Furthermore, the small and ephemeral nature of the focal mechanism dip-slip component suggests that the buoyancy effects due to the serpentinite intrusion are relatively equal on both the Juan de Fuca and Pacific plate sides of the transform, with the possibility that the Pacific plate side is slightly more buoyant as evidenced by the majority of mechanisms which indicate Juan de Fuca plate subsidence. But in general, the diapiric buoyancy effects may be offsetting any significant differential subsidence due to crustal age contrasts.

The presence of mylonitized gabbro along the BTFZ (collected at the BR summit at site 2) provides evidence for shear deformation occurring to at least layer 3 depth above the Moho. Mylonites form due to extreme shear, at greenschist temperatures and pressures, under quasi-plastic flow in the crustal transition zone between brittle and plastic deformation (Sibson, 1986). In the case of oceanic crust, the brittle-plastic transition would be controlled by the depth of olivine plasticity (750-900°C), and thus the brittle seismogenic layer might include the upper mantle (Yeats et al., 1997). But no evidence for upper mantle shear deformation was found in the samples collected.

The presence of conglomerate, mudstone, and volcanic arenite at the top of the ridge (site 3) is intriguing. One possibility is that they are the remains of turbidites that were originally deposited along the base of the Blanco Ridge within the Cascadia Deep-Sea Channel. The Cascadia Channel runs along the north base of the Blanco Ridge, so speculatively the turbidites could have been deposited along the BR north base (possibly even within the abandoned meander at 127° 20'W, Figure 5.1), and subsequently uplifted and transported westward by transform motion once emplaced on the Pacific plate. Another possibility is that the sedimentary rocks were formed at a time when this section of Blanco Ridge was uplifted to near sea level, a process that has been documented at other fracture zones (Romanche F.Z., Honnorez et al. 1991; Mendocino F.Z. Fisk et al., 1995). The exact mechanism for emplacement of sedimentary units at the top of the Blanco Ridge is not clear at this point, but might be addressed better with a more thorough analysis of the sedimentary rocks.

The eastern BTFZ is a tectonic environment dominated by a high shear stress, strike-slip fault experiencing a small component of uplift, probably due to a serpentinite diapir, resulting in the formation of a transform-parallel ridge and the uplift of an oceanic crustal section. Obduction of transform ridges may be one mechanism by which

ophiolites are preserved. Thus the mechanism of formation for transform ridges is an important question for many fields of study, and one which could be better constrained for the Blanco Ridge with drilling, deep-tow magnetics and gravity, and heat flow observations that would help further document the crustal composition, isotherm depth, *in situ* stress regimes, and coupling strength along the transform.

## 5.9 Acknowledgments

The authors wish to thank Bill Normark and Chris Gutmacher for the 1985 U.S.G.S. Airgun profiles, Alice Davis and Jane Reid for the petrologic information, Vern Kulm for providing the 1969 Oregon State University seismic reflection data, Virginia Smith and Stephanie Ross for excellent at-sea support, and Matt Fowler and Paul Johnson for assistance with graphics. Also, the authors wish to thank the officers and crew of the R/V *Laney Chouest* and the U.S. Navy Deep Submergence Unit/Advanced Tethered Vehicle for expertise at sea without which this study could not have been conducted. This research was supported by the NOAA VENTS Program.

## 5.10 References

Aki, K. and P.G. Richards. 1980. *Quantitative Seismology, Theory and Methods.* New York: W.H. Freeman and Company.

Batiza, R., and D. Vanko. 1983. Volcanic Development of Small Oceanic Central Volcanoes on the Flanks of the East Pacific Rise Inferred from Narrow Beam Echo Sounder Surveys. *Marine Geology*, 54:53-90.

Bergman, E.A. and S.C. Solomon. 1988. Transform Fault Earthquakes in the North Atlantic: Source Mechanism and Depth of Faulting. *J. Geophys. Res.*, 93:9027-9057.

Bonatti, E., 1976. Serpentinite Intrusions in the Oceanic Crust. *Earth Plan. Sci. Letts.*, 32:107-113.

Bonatti, E.. 1978. Vertical Tectonism in Oceanic Fracture Zones. *Earth Planet. Sci. Lett.*, 78:420-426.

Braunmiller, J., B. Leitner, and J. Nabelek. 1994. Monitoring Seismic Activity along the Blanco Fracture Zone with Regional Broad-Band Data, *Eos*, Trans. Amer. Geophys. Un., 75:476.

Clague, D.A. and M.L. Holmes. 1987. Geology, Petrology, and Mineral Potential of the Gorda Ridge, in *Geology and Resource Potential of the Continental Margin of Western North America and Adjacent Ocean Basins - Beaufort Sea to Baja California*, D.W. Sholl, A. Grantz, and J.G. Vedder (eds.), Circum-Pacific Council for Energy and Mineral Resources Earth Science Series, 6:563 - 580.

Craig, C.H., and D. MacKenzie. 1986. The Existence of a Thin, Low Viscosity Layer Beneath the Lithosphere. *Earth Planet Sci Lett.*, 78:420-426.

deCharon, A.V. 1988. Structure and Tectonics of the Cascadia Segment, Central Blanco Transform Fault Zone, M.S. Thesis, Oregon State University, Corvallis , Oregon.

DeMets, C., R.G. Gordon, D.F. Argus, and S. Stein. 1990. Current Plate Motions. *Geophys. J. Int.*, 101:425-478.

Dziak, R.P., C.G. Fox, and R.W. Embley. 1991. Relationship Between the Seismicity and Geologic Structure of the Blanco Transform Fault Zone. *Mar. Geophys. Res.*, 13:203-208.

Dziak, R.P., C.G. Fox, R.W. Embley, J.L. Lupton, G.C. Johnson, W.W. Chadwick, R.A. Koski. 1996. Detection of and Response to a Probable Volcanogenic T-wave Event Swarm on the Western Blanco Transform Fault Zone. *Geophys. Res. Lett.*, 23:873-876.

Embley, R.W. 1985. A Locally Formed Deep-Ocean Canyon System Along the Blanco Transform. *Geo-Marine Letts.*, 5:99-104.

Embley, R.W., L.D. Kulm, G. Massoth, D. Abbott, and M. Holmes. 1987. Morphology, Structure, and Resource Potential of the Blanco Transform Fault Zone. In *Geology and Resource Potential of the Continental Margin of Western North America and Adjacent Ocean Basins - Beaufort Sea to Baja California*, D.W. Sholl, A. Grantz, and J.G. Vedder (eds.), Circum-Pacific Council for Energy and Mineral Resources Earth Science Series, v. 6, p. 549 - 562.

Embley R.W., and D.S. Wilson. 1992. Morphology of the Blanco Transform Fault Zone -- NE Pacific: Implications for its Tectonic Evolution. *Mar. Geophys. Res.*,14:25-45 1992.

Epp, D. 1984. Possible Perturbations to Hotspot Traces and Implications for the Origin and Structure of the Line Islands. *J. Geophys. Res.*, 89:11273-11286.

Fisk, M.R., R.A. Duncan, C.G.Fox, and J.B. Witter. 1993. Emergence and Petrology of the Mendocino Ridge. *Mar. Geophys. Res.*, 15:283-296.

Fox, C.G., R.P. Dziak, H. Matsumoto, and A.E. Schreiner. 1994. Potential for Monitoring Low-level Seismicity on the Juan de Fuca Ridge Using Fixed Hydrophone Arrays. *Mar. Tech. Soc.*, 27:22-30.

Griggs, G.B. and L.D. Kulm. 1973. Origin and Development of Cascadia Deep-Sea Channel. *J. Geophys. Res.*, 9:6325-6339.

Hart, R., D. Pyle, and J. Robbins. 1990. Multistage Hydrothermal Systems in the Blanco Fracture Zone. In *Gorda Ridge, Seafloor Spreading Center in the United States' Exclusive Economic Zone*, ed G.R. McMurray, 51-76, New York: Springer-Verlag.

Hekinian, R., D. Bideau, M. Cannat, J. Francheteau, and R. Hebert. 1992. Volcanic Activity and Crust-Mantle Exposure in the Ultrafast Garret Transform Fault Near 1328'S in the Pacific. *Earth Planet Sci Lett.*, 108:259-275.

Honnorez, J. J. Mascle, C. Basile, P. Tricart, M. Villeneuve, and H. Bertrand. 1991. A Morphostructural Analysis of a Major Transform Fault of the Equitorial Atlantic Ocean. *Geology*, 19:795-798.

Ibach, D.H. 1986. The Structure and Tectonics of the Blanco Fracture Zone. M.S. Thesis, 60pp., Oregon State University, Corvallis, Oregon.

Ihmle, P.F. and T.H. Jordan. 1994. Teleseismic Search for Slow Precursors to Large Earthqaukes. *Science*, 266:1547-1551.

Kastens, K.A., W.B.F. Ryan, and P.J. Fox. 1986. Structural and Volcanic Expression of a Fast Slipping Ridge-Transform-Ridge Plate Boundary: Sea Marc I and Photographic Surveys at the Clipperton Transform Fault. *J. Geophys. Res.*, 91:3469-3488.

Koski, R.A., R.W. Embley, S.L. Ross, R.P. Dziak, R.G. Bohannon, V.K. Smith, J.A. Reid, L.B. Gray, and T.O. Tormanen. 1994. Tectonism and Lithologic Variation Along the Blanco Ridge, Eastern Blanco Fracture Zone, NE Pacific: Preliminary Results from the PACNORWEST III Cruise: *Eos*, Trans. Amer. Geophys. Un., 75:656.

Lonsdale, P. 1985. Non-Transform Offsets of the Pacific-Cocos Plate Boundary and Their Traces on the Rise Flank. *Geo. Soc. Amer. Bull.*, 96:313-329.

Mount, V.S. and J. Suppe. 1992. Present-day stress Orientations Adjacent to Active Strike-slip Faults: California and Sumatra. *J. Geophys. Res.*, 97:11995-12013.

Nabelek, J. and G.. Xia. 1995. Regional and Teleseismic Analysis of the 29 March, 1993. Scotts Mills, Oregon, Earthquake. *Geophys. Res. Lett.*, 22:13-16.

National Earthquake Information Center. 1992. *Preliminary Determination of Epicenters Catalog*, October.

Oppenheimer, D.H., P.A. Reasonberg, and R.W. Simpson. 1988. Fault Plane Solutions for the 1984 Morgan Hill, California Earthquake Sequence: Evidence for the State of Stress on the Calaveras Fault. *J. Geophys. Res.*, 92:421-439.

Pockalny, R.A., P.J. Fox, D.J. Fornari, K.C. Macdonald, and M.R. Perfit. 1997. Tectonic Reconstructions of the Clipperton and Siqueiros Fracture Zones: Evidence and Consequences of Plate Motion Change for the Last 3 Myr. *J. Geophys. Res.*, 102:3167-3181.

Riddihough, R.P. D.A. Seemann, and W.R. Price. 1982. Juan de Fuca Plate Map: *JFP-8 Gravity Anomaly*. Earth Physics Branch: Department of Energy, Mines, and Resources, Ottawa, Canada.

Riddihough, R.P. 1984. Juan de Fuca Plate Map: *JFP-11 Magnetic Anomaly, Open File 85-20*. Pacific Geoscience Centre, Earth Physics Branch, Department of Energy, Mines, and Resources, Sidney, B.C. Canada.

Sibson, R.H. 1986. Earthquakes and Rock Deformation in Crustal Fault Zones *Annual Review of Earth and Planetary Sciences*. 14:149-175.

Thompson, G. and W.G. Melson. 1972. The Petrology of Oceanic Crust Across Fracture Zones in the Atlantic Ocean: Evidence for a New Kind of Seafloor Spreading. *J. Geol.*, 80:526-538.

Tobin, D.G. and L.R. Sykes. 1968. Seismicity and Tectonics of the Norhteast Pacific Ocean. *J. Geophys. Res.*, 94:3076-3089.

Wilson, D.S., R.N. Hey, and C. Nishimura. 1984. Propagation as a Mechanism of Reorientation of the Juan de Fuca Ridge. *J. Geophys. Res.*, 89:9215-9225.

Wilson, D.S.. 1989. Deformation of the So-Called Gorda Plate. *J. Geophys. Res.*, 94:3065-3075.

Wilson, D.S. 1993. Confidence Intervals for Motion and Deformation of the Juan de Fuca Plate. *J. Geophys. Res.*, 98:16053-16071.

Yeats, R.S., K Sieh, and C.R. Allen. 1997. *The Geology of Earthquakes*, Oxford University Press, 503pp.

# Chapter 6

# Conclusions

The scientific purpose of this study was to use the SOSUS hydrophone array data to detect and locate earthquakes along the Blanco Transform Fault Zone and Gorda plate for insight into the current state of stress and mechanics of crustal deformation in these regions. The acoustic earthquake information combined with high-resolution bathymetry, camera-tow and submersible observations, earthquake source-parameter estimates, petrologic samples, and water-column chemistry provided an up to date view of the recent tectonics along the southern Juan de Fuca and Gorda plates. The main goal of this thesis was to establish the advantages of using the SOSUS hydrophone array time-series data to do regional monitoring and tectonic studies of oceanic earthquakes through the system's continuous recording capability, the ability to derive highly accurate locations for oceanic earthquakes compared to west coast regional seismic networks, and the hydrophone data's relative cost efficiency relative to Ocean Bottom Seismometer data. This study discusses the development of acoustic earthquake detection and location techniques, and is the first thorough use of these techniques to understand the recent tectonics of submarine plate boundaries.

The final problem considered here is a potential tectonic link between the deformation observed along the Blanco Transform Fault Zone (BTFZ) and mid-Gorda plate. To briefly summarize the deformation, the western half of the BTFZ is a leaky transform, dominated by an extensional environment and volcanic processes. In contrast the eastern BTFZ is a tectonic environment dominated by a right-lateral strike-slip fault

experiencing a small component of uplift, probably due to a serpentinite diapir. Internal deformation of the Gorda plate may be occurring as reverse faulting or possibly strike-slip faulting with a reverse component. Focal mechanisms of large Gorda intraplate earthquakes suggest the plate is deforming internally through left-lateral strike-slip faulting under N-S maximum compressive stress (Velasco et al., 1994). A finite-element stress model of the Gorda plate (Wang et al., 1997) found N-S horizontal maximum compressive stress throughout the plate largely controlled by strike-parallel subduction resistance at the Cascadia Subduction Zone. Furthermore, the stress models suggest that plastic yielding (permanent deformation) most likely occurs in a NW-SE direction through the plate, from the eastern BTFZ-northern Gorda Ridge to the MTJ.

This recent deformation observed along the BTFZ and mid-Gorda plate is likely a result of the re-orientation of the Juan de Fuca (JdF) plate (Wilson, 1993). The Juan de Fuca plate rotation is likely reflecting the re-orientation of the Pacific plate and the northward migration of the Mendocino Triple Junction (MTJ). The migration of the triple junction may result in the linking of the San Andreas Fault (SAF) to the eastern BTFZ, and an eventual shift of the triple junction to the BTFZ-Gorda Ridge intersection. It is speculated here that the eastern BTFZ and mid-Gorda plate deformation may be reflecting NW-SE transform style motion as the initiation of migration of the MTJ through this region and the linkage of the eastern BTFZ to the SAF. A similar model of recent deformation in the Explorer plate region has been proposed by Rohr and Furlong (1995) using earthquake slip vectors from along the Revere-Dellwood Transform, Explorer Ridge, and Sovanco Transform. Rohr and Furlong (1995) suggests that, on the basis of earthquake slip vectors

paralleling Pacific - North America plate motion, the Explorer Ridge is becoming extinct, the Explorer plate is presently a transform boundary, and the northern Juan de Fuca Ridge is the current triple junction location.

If transform-style deformation is occurring in the Gorda plate, then earthquake slip vector, aftershock distributions, and fault trends should all reflect Pacific - North America relative plate motion. Consequently, the orientations of the Nuvel-1 relative plate motion vectors (DeMets, 1990), earthquake slip vectors, plate boundary orientations, the Gorda plate T-wave seismicity trend, and mid-Gorda plate fault trends are summarized in Figure 6.1 to test this hypothesis. Earthquake slip vectors from the eastern BTFZ (Figure 5.7) generally parallel JdF - Pacific relative plate motion of N120°E. Slip vectors within the Gorda Depression (eastern BTFZ) diverge from this relative plate motion vector (Figure 5.7), but earthquake slip vectors along strike-slip fault segments (earthquake Ev11 along the fracture zone east of the transform) are close to the N120°E trend. Four of the five large (M>6) 1991-1992 Gorda intraplate events had their slip directions estimated (events Ev1, Ev4, Ev6 and Ev7, Figure 6.1; Velasco et al., 1994). The slip vector of Ev1 parallels JdF-Pac plate motion, while Ev4 does not follow any of the Nuvel-1 plate motion vectors, but does seem to parallel JdF-NA motion (N216°E) from Riddihough et al. (1984). Ev6 and Ev7, while trending close to JdF-Pac and JdF-NA motion, do not seem to follow closely any of the relative plate motion vectors. Ev1 and Ev4 (and Ev6 and Ev7) have nearly orthogonal slip vectors, and occurred close in space and time, which suggests the Gorda

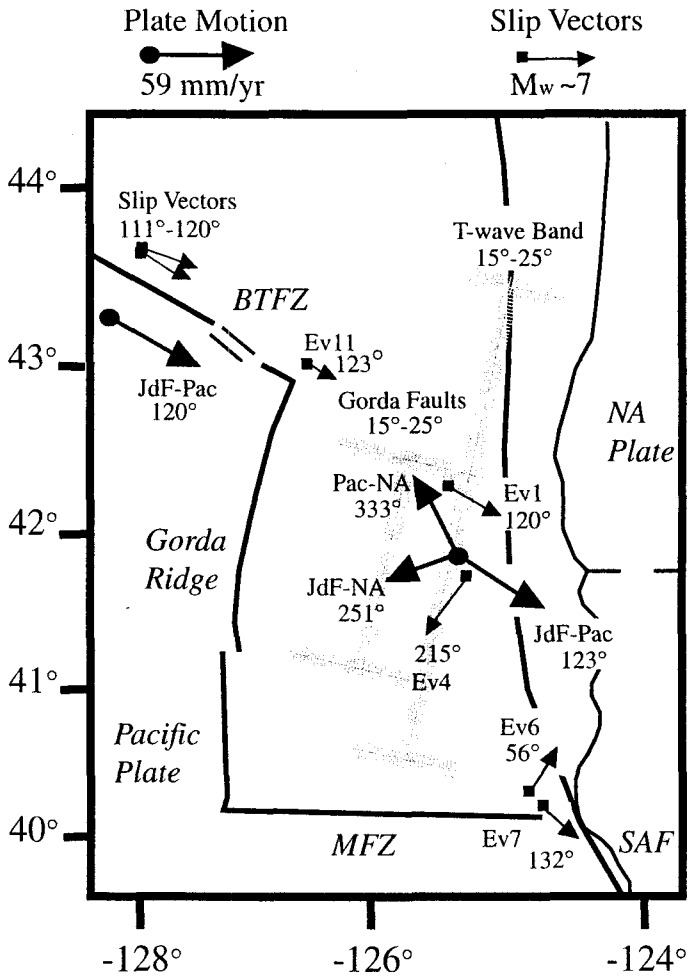


Figure 6.1 Location map of major plate boundaries, relative plate motion vectors, earthquake slip vectors, T-wave seismicity band, and fault trends along the southern Juan de Fuca plate boundaries. Scale for plate motion and slip vector size are shown at the top of the diagram. Degree value associated with each vector is the northeast azimuth. Preferred fault plane used to estimate slip vectors for Events 1, 4, 6, and 7 were determined by Velasco et al, (1994). T-wave seismicity band and Gorda plate fault zone represented by grey bars, line segments at the end denote approximate width of the mid-Gorda plate fault zone and seismicity band. Abbreviations are: Blanco Transform Fault Zone (BTFZ), Juan de Fuca (JdF), North America (NA), Pacific (Pac), Mendocino Fracture Zone (MFZ), San Andreas Fault (SAF).

plate is undergoing conjugate strike-slip faulting. Conjugate strike-slip faulting might be the deformation mode by which a through going transform fault is developed, but this is highly conjectural. Also Ev1 parallels JdF-Pac motion suggesting that Ev1 represents JdF plate motion. The other three events do not parallel any of the relative plate motion vectors in Figure 6.1, suggesting that they represent motion of the independent Gorda plate.

The trends of the T-wave seismicity band and mid-Gorda plate faults seem to parallel and overlap one another, so the T-wave earthquakes are probably occurring due to slip on the mid-plate faults. But the mid-plate faults and T-wave band are seemingly oblique to all the major plate motion trends. This might be expected since the faults are reactivated ridge spreading fabric, their strikes may not follow perfectly the faulting (stress) regime dictated by current plate motion. Thus the T-wave seismicity and mid-Gorda plate fault trends do not seem to support the transform model. Although as discussed in Chapter 4, there does appear to be a relationship between the T-wave seismicity - Gorda plate faults and deformation occurring at the MTJ. Indeed, perhaps deformation within the Gorda plate is reflecting northward MTJ migration, but because it is occurring along re-activated faults, the trend of deformation is not consistent with NW-SE transform motion. Lastly, the extension of the T-wave band across the Gorda JdF plate boundaries seems to suggest there is some degree of coupling across the Gorda and JdF plates and that deformation within the Gorda plate extends into the JdF plate.

It is apparent that more information must be obtained to clarify models of Gorda plate active faulting and internal deformation. In the fall of 1997, NOAA/PMEL plans a bathymetric survey (using Sea Beam 2112) of the entire Gorda deformation zone. This

multibeam survey will be augmented by the collection of gravity and magnetics along closely spaced tracklines, as well as continuous digital 3.5 kHz sub-bottom profiler. It is anticipated that these high-resolution bathymetric, seismic reflection, and potential field data sets could provide for development of a kinematic model of Gorda plate - eastern BTFZ deformation that is consistent with, and better accounts for, the basement deformation and seismicity data presented in this study.

# Bibliography

Aki, K. and P.G. Richards. 1980. *Quantitative Seismology, Theory and Methods.* New York: W.H. Freeman and Company.

Baker, E.T., G.J Massoth, and R.A. Feely. 1987. Cataclysmic Hydrothermal Venting on the Juan de Fuca Ridge. *Nature*, 329:149-151.

Baker, E.T., G.J. Massoth, R.A. Feely, R.W. Embley, R.E. Thomson, and B.J. Burd. 1985. Hydrothermal Event Plumes from the CoAxial Seafloor Eruption Site, Juan de Fuca Ridge. *Geophys. Res. Lett.*, 22:147-150.

Barany, I. And J.A. Karson. 1989. Basaltic Breccias of the Clipperton Fracture Zone (East Pacific): Sedimentation and Tectonics in a Fast-Slipping Oceanic Transform. *Geol. Soc. Amer. Bull.*, 101:204-220.

Batiza, R., and D. Vanko. 1983. Volcanic Development of Small Oceanic Central Volcanoes on the Flanks of the East Pacific Rise Inferred from Narrow Beam Echo Sounder Surveys. *Marine Geology*, 54:53-90.

Ben-Menahem, A. and M.N. Toksoz. 1963. Source-Mechanism from spectra of long-period seismic surface waves, 3: The Alaska earthquake of July 10, 1958. *Bull. Seism. Soc. Am.*, 53:905-919.

Bergman, E.A. and S.C. Solomon. 1988. Transform Fault Earthquakes in the North Atlantic: Source Mechanism and Depth of Faulting. *J. Geophys. Res.*, 93:9027-9057.

Bonatti, E., 1976. Serpentinite Intrusions in the Oceanic Crust. *Earth Plan. Sci. Letts.*, 32:107-113.

Bonatti, E., P.J. Guerstein-Honnorez, and J. Honnorez. 1976. Copper-iron Sulfide Mineralizations from the Equatorial Mid-Atlantic Ridge. *Econ. Geol.*, 71:1515-15125.

Braunmiller, J., B. Leitner, and J. Nabelek. 1994. Monitoring Seismic Activity along the Blanco Fracture Zone with Regional Broad-Band Data *Eos*, Trans. Amer. Geophys. Un., 75:476.

Brazee, R.J. 1965. A study of T-phases in the Aleutian earthquake series of March and April 1957. *Earthquake Notes*, 36:9-14.

Brocher, T.M. 1983. T-phases from an earthquake swarm on the Mid-Atlantic Ridge at 31.6°N. *Mar. Geophys. Res.*, 6:39-49.

Bulletin of the Global Volcanism Network. 1993. No. 1, 9-12, January 31.

Cansi, Y. and N. Bethoux. 1985. T-waves with long inland paths: Synthetic seismograms. *J. Geophys. Res,* 90:5459-5465.

Chandra, U. 1974. Seismicity, Earthquake Mechanisms, and Tectonics along the Western Coast of North America from 42°N to 61°N. *Bull. Seism. Soc. Amer.*, 64:1529-1549.

Chapple, W.M. and D.W. Forsyth. 1979. Earthquakes and Bending of Plates at Trenches. *J. Geophys. Res.*, 84:6729-6749.

Christensen, D.H. and L.J. Ruff. 1988. Seismic Coupling and Outer Rise Earthquakes. *J. Geophys. Res.*, v:93, 13421-13444.

Clague, D.A. and M.L. Holmes. 1987. Geology, Petrology, and Mineral Potential of the Gorda Ridge. In *Geology and Resource Potential of the Continental Margin of Western North America and Adjacent Ocean Basins - Beaufort Sea to Baja California*, D.W. Sholl, A. Grantz, and J.G. Vedder (eds.), Circum-Pacific Council for Energy and Mineral Resources Earth Science Series, 6:563 - 580.

Clarke, A.C. 1982. *2010: Odyssey 2*. New York, New York. Ballatine Books.

Clipperton Tectonic Team. 1992. Investigations of the Clipperton Transform: The Anatomy of a Shear Zone. *Mar. Geophys. Res.*, 14:200-214.

Craig, C.H., and D. MacKenzie. 1986. The Existence of a Thin, Low Viscosity Layer Beneath the Lithosphere. *Earth Planet Sci Lett.*, 78:420-426.

deCharon, A.V. 1988. Structure and Tectonics of the Cascadia Segment, Central Blanco Transform Fault Zone. M.S. Thesis, Oregon State University, Corvallis , Oregon.

DeMets, C., R.G. Gordon, D.F. Argus, and S. Stein. 1990. Current Plate Motions. *Geophys. J. Int.*, 101:425-478.

Dengler, L, G. Carver, and R. McPherson. 1992. Sources of North Coast Seismicity. *Calif. Geol*, 45:40-53.

Dziak, R.P., C.G. Fox, and R.W. Embley. 1991. Relationship Between the Seismicity and Geologic Structure of the Blanco Transform Fault Zone. *Mar. Geophys. Res.*, 13:203-208.

Dziak, R.P., C.G.Fox, A.E. Schreiner. 1995. The June-July 1993 Seismo-acoustic Event at CoAxial Segment, Juan de Fuca Ridge: Evidence for a Lateral Dike Injection. *Geophys. Res. Lett.*, 22:135-138.

Dziak, R.P., C.G. Fox, R.W. Embley, J.L. Lupton, G.C. Johnson, W.W. Chadwick, R.A. Koski. 1996. Detection of and Response to a Probable Volcanogenic T-wave

Event Swarm on the Western Blanco Transform Fault Zone, *Geophys. Res. Lett.*, 23:873-876.

Dziak, R.P., C.G. Fox, H. Matsumoto, A.E. Schreiner. 1997. The April 1992 Cape Mendocino Earthquake Sequence: Seismo-acoustic Analysis Utilizing Fixed Hydrophone Arrays. *Mar. Geophys. Res.*, in press.

Dziewonski, A.M., G. Ekstrom, and M.P. Salganik. 1992. Centroid-Moment Tensor Solutions for July- September 1991. *Phys. Earth Planet. Inter.*, 72:1-11.

Dziewonski, A.M., G. Ekstrom, and M.P. Salganik. 1993. Centroid-Moment Tensor Solutions for April-June 1992. *Phys. Earth Planet. Inter.*, 77:151-163.

Eaton, J.P.. 1977. Frequency response of the U.S.G.S. short period telemetered seismic system and its suitability for network studies of local earthquakes. *Geol. Surv. Open-File Rep.*, 77-844, 1-45.

Einarsson, P. 1991. Earthquakes and present-day tectonism in Iceland. *Tectonophys.*, 189:261-279.

Embley, R.W. 1985. A Locally Formed Deep-Ocean Canyon System Along the Blanco Transform. *Geo-Marine Letts.*, 5:99-104.

Embley, R.W., Kulm, L.D., Massoth, G., Abbott, D., Holmes, M. 1987. Morphology, Structure, and Resource Potential of the Blanco Transform Fault Zone. In *Geology and Resource Potential of the Continental Margin of Western North America and Adjacent Ocean Basins - Beaufort Sea to Baja, California*, 549-561, (ed. Scholl, D. W., Grantz, A., Yedder, J. G., Amer. Assoc. Petro. Geologists).

Embley, R.W., and D.S. Wilson. 1992. Morphology of the Blanco Transform Fault Zone-NE Pacific: Implications for its Tectonic Evolution. *Mar. Geophys. Res.*, 14, 25-45.

Embley, R.W., W.W. Chadwick, I.R. Jonasson, D.A. Butterfield, and E.T. Baker. 1995. Initial Results of the Rapid Response to the 1993 CoAxial Event: Relationships Between Hydrothermal and Volcanic Processes. *Geophys Res. Lett.*, 22, 143-146.

Epp, D. 1984. Possible Perturbations to Hotspot Traces and Implications for the Origin and Structure of the Line Islands. *J. Geophys. Res.*, 89:11273-11286.

Fagan, D., 1992. *I.G.Y. - The Night Fly*. Warner Brothers Records, Inc.

Fisk, M.R., R.A. Duncan, C.G.Fox, and J.B. Witter. 1993. Emergence and Petrology of the Mendocino Ridge. *Mar. Geophys. Res.*, 15:283-296.

Fox, C.G., R.P. Dziak, H. Matsumoto, and A.E. Schreiner. 1994. Potential for Monitoring Low-Level Seismicity on the Juan de Fuca Ridge using Fixed Hydrophone Arrays. *Mar. Tech. Soc.*, 27:22-30.

Fox, C.G., W.E. Radford, R.P. Dziak, T-K. Lau, H. Matsumoto, and A.E. Schreiner. 1995. Acoustic detection of a seafloor spreading Episode on the Juan de Fuca Ridge using military hydrophone arrays. *Geophys. Res. Lett.*, 22:131-134.

Fox, C.G. and H. Matsumoto. 1996. Monitoring northeast Pacific seismicity using autonomous hydrophone moorings. *EOS, Trans. Amer Geophys. Un.*, 76:412.

Gibowicz, S.J., J.H. Latter, and G.K. Sutton. 1974. Earthquake swarm associated with a volcanic eruption, Curacoa Reef area, northern Tonga, July 1973. *Ann. Geofis.*, 27:443-475.

Goldfinger, C., L.D. Kulm, R.S. Yeats, C. Mitchell, R. Weldon, II, C. Peterson, M. Darienzo, W. Grant, and G.R. Priest. 1992. Neotectonic Map of the Oregon Continental Margin and Adjacent Abyssal Plain. *Oregon Dep. Geol. Min. Ind. Open File Rep. 0-92-4.*

Griggs, G.B. and L.D. Kulm. 1973. Origin and Development of Cascadia Deep-Sea Channel. *J. Geophys. Res.*, 9:6325-6339.

Gupta, I.N. 1964. Discussion of "Source-mechanism from Spectsa of long-period seismic surface waves, 3: The Alaska earthquake of July 19, 1958", by A. Ben-Menahem and M.N. Toksoz. *Bull. Seism. Soc. Am.*, 54:2085-2086.

Hart, R., D. Pyle, and J. Robbins. 1990. Multistage Hydrothermal Systems in the Blanco Fracture Zone. In *Gorda Ridge, Seafloor Spreading Center in the United States' Exclusive Economic Zone*, ed G.R. McMurray, 51-76, New York: Springer-Verlag.

Hekinian, R., D. Bideau, M. Cannat, J. Francheteau, and R. Hebert. 1992. Volcanic Activity and Crust-Mantle Exposure in the Ultrafast Garret Transform Fault near 13R28'S in the Pacific. *Earth and Planet. Sci. Lett.*, 108:259-275.

Herzig, C.T. and W.A. Elders. 1988. Nature and Significance of Igneous Rocks Cored in the State 2-14 Research Borehole: Salton Sea Scientific Drilling Project, California. *J. Geophys. Res.*, 93:13069-13080, 1988.

Hiyoshi, Y., D.A. Walker, C.S. McCreery. 1992. T-phase data and regional tsunami-genesis in Japan. *Bull. Seism. Soc. Am.*, 82:2213-2223.

Holmes, E.S., E.C. Miller, and R.H. Stephens 1990. A PC-based acoustic model operating system. IEEE *Oceans '90*, 227-231.

Honnorez, J. J. Mascle, C. Basile, P. Tricart, M. Villeneuve, and H. Bertrand. 1991. A Morphostructural Analysis of a Major Transform Fault of the Equitorial Atlantic Ocean. *Geology*, 19:795-798.

Ibach, D.H. 1986. The Structure and Tectonics of the Blanco Fracture Zone. M.S. Thesis, 60pp., Oregon State University, Corvallis, Oregon.

Ihmle, P.F. and T.H. Jordan. 1994. Teleseismic Search for Slow Precursors to Large Earthquakes, *Science*, 266:1547-1551.

Koski, R.A., R.W. Embley, S.L. Ross, R.P. Dziak, R.G. Bohannon, V.K. Smith, J.A. Reid, L.B. Gray, and T.O. Tormanen. 1994. Tectonism and Lithologic Variation Along the Blanco Ridge, Eastern Blanco Fracture Zone, NE Pacific: Preliminary Results from the PACNORWEST III Cruise, 1994: *Eos*, Trans. Amer. Geophys. Un. 75:656.

Johnson, R.H., J. Northrop, and R. Eppley. 1963. Sources of Pacific T-phases. *J. Geophys. Res.*, 68:4251-4260.

Johnson R.H. and J. Northrop 1966. A comparison of earthquake magnitude with T-phase strength. *Bull. Seism. Soc. Am.*, 56:119-124.

Johnson, R.H. 1970. Estimating rupture length from T-waves. In Tsunamis in the Pacific Ocean, *Proc. of the International Symposium on Tsunamis and Tsunami Research*, ed. W.M. Adams, 253-259, East West Center Press, Honolulu, HI.

Kanamori, H.. 1977. Seismic and Aseismic Slip along Subduction Zones and their Tectonic Implications. In *Island Arcs, Deep Sea Trenches, and Back-Arc Basins*, Maurice Ewing Ser., v:1, ed M. Talwani and W.C. Pitman III, 163-174, AGU, Washington, D.C.

Kanamori, H, and M. Kikuchi. 1993. The 1992 Nicaragua earthquake: A Slow tsunami earthquake associated with Subducted Sediments. *Nature*. 361:714-716.

Kastens, K.A., W.B.F. Ryan, and P.J. Fox. 1986. Structural and Volcanic Expression of a Fast Slipping Ridge-Transform-Ridge-Plate Boundary: Sea Marc I and Photographic Surveys at the Clipperton Transform Fault. *J. Geophys. Res.*, 91:3469-3488.

Klein, F.W., R.Y. Koyanagi, J.S. Nakata, and W.R. Tanigawa. 1987. The seismicity of Kilauea's magma system. *U.S. Geol. Surv. Prof. Paper* 1350, 1019-1186.

Lay, T., J.W. Given, and H. Kanamori. 1982. Long-period Mechanism of the 8 November 1980 Eureka, California, Earthquake. *Bull.Seism. Soc. Am.*, 71:1-24.

Linehan, D. 1940. Earthquakes in the West Indian Region. *Trans. Am. Geophys. Union*, 229-232.

Lonsdale, P. 1985. Non-Transform Offsets of the Pacific-Cocos Plate Boundary and Their Traces on the Rise Flank. *Geo. Soc. Amer. Bull.*, 96:313-329.

Lupton, J.E., E.T. Baker, and G. Massoth. 1989. Variable $^{3}$He/heat Ratios in Submarine Hydrothermal Systems: Evidence from two Plumes over the Juan de Fuca Ridge. *Nature*, 337, 161-164, 1989.

Lupton, J.E., E.T. Baker, G.J. Massoth, R.E. Thomson, B.J. Burd, D.A. Butterfield, R.W. Embley, and G.A. Cannon. 1995. Variations in Water Column $^{3}$He/heat Ratios Associated with the 1993 CoAxial Event, Juan de Fuca Ridge. *Geophys. Res. Lett.*, 22:155-158.

Massoth, G.J., E.T. Baker, R.A. Feely, D.A. Butterfield, R.W. Embley, and G.A. Cannon. 1995. Variations of Manganese and Iron at the CoAxial Seafloor Eruption Site, Juan de Fuca Ridge. *Geophys. Res. Lett.*, 22:151-154.

McCaffrey, R., and C. Goldfinger. 1995. Forearc Deformation and Great Subduction Zone Earthquakes: Implications for Cascadia Offshore Earthquake Potential. *Science*, 267:856-859.

Mount, V.S. and J. Suppe. 1992. Present-day stress Orientations Adjacent to Active Strike-slip Faults: California and Sumatra. *J. Geophys. Res.*, 97:11995-12013.

Nabelek, J. and G.. Xia, Regional and Teleseismic Analysis of the 29 March, 1993, Scotts Mills, Oregon, Earthquake. 1995. *Geophys. Res. Lett.*, 22:13-16.

National Earthquake Information Center. 1992. *Preliminary Determination of Epicenters Catalog*, October.

Naval Oceanographic Office, System Integration Division. 1991. Software requirements and specifications for the Parabolic Equation model, OAML-SRS-22C, Stennis pace Center, Mississippi 39522-5001, March.

Newmark, R.L., P.W. Kasameyer, and L.W. Younker. 1988. Shallow Drilling in the Salton Sea Region: The Thermal Anomaly. *J. Geophys. Res.*, 93, 13005-13023.

Northrop, J., M. Blaik, and I. Tolstoy 1960. Spectrum analysis of T-phases from the Agadir earthquake, February 29, 1960, 23h 40m 12s GCT, 30°N, 9°W (USGCS). *J. Geophys. Res.*, 65:4223-4224.

Okal, E.A., and J. Talandier. 1986. T-wave duration, magnitudes, and seismic moment of an earthquake: Application to tsunami warning. *J. Phys. Earth*, 34:19-42.

Oppenheimer, D.H., P.A. Reasonberg, and R.W. Simpson. 1988. Fault Plane Solutions for the 1984 Morgan Hill, California, Earthquake Sequence: Evidence for the State of Stress on the Calaveras Fault. *J Geophys. Res.*, 92:421-439.

Oppenheimer, D., G. Beroza, G. Carver, L. Dengler, J. Eaton, L. Gee, F. Gonzalez, A. Jayko, W.H. Li, M. Lisowski, M. Magee, G. Marshall, M. Murray, R. McPherson, B. Romanowicz, K. Satake, R. Simpson, P. Somerville, R. Stein, D. Valentine. 1993. The Cape Mendocino, California Earthquake Sequence of April 1992: Subduction at the Triple Junction. *Science*, 261:433-438.

Perfit, M.R., D.J. Fornari, J.F. Casey, K.A. Kastens, W.I. Ridley, P.D. Kirk, M. Edwards, D. Desonie, J.R. Reynolds, R. Shuster, S. Paradis, C. Xia, D. Barlaz. 1993 Recent Volcanism in the Siqueiros Transform Fault: Eruption of Picritic and High-MgO Basalts and Implications for MORB Magma Genesis. *Earth and Planet. Sci. Lett.*, 109:4501-460.

Pockalny, R.A., P.J. Fox, D.J. Fornari, K.C. Macdonald, and M.R. Perfit. 1997. Tectonic Reconstructions of the Clipperton and Siqueiros Fracture Zones: Evidence and Consequences of Plate Motion Change for the Last 3 Myr. *J. Geophys. Res.*, 102:3167-3181.

Preliminary Determination of Epicenters. 1992. United States Geological Survey, National Earthquake Information Center, April.

Preliminary Determination of Epicenters. 1994. United States Geological Survey, National Earthquake Information Center, January.

Richter, C.F. 1949. *Seismicity and structure of the Pacific Region of North America.* Proc. 7th Pacific Sci. Congr., 2, pp 671.

Riddihough, R.P. D.A. Seemann, and W.R. Price. 1982. Juan de Fuca Plate Map: *JFP-8 Gravity Anomaly*. Earth Physics Branch: Department of Energy, Mines, and Resources, Ottawa, Canada.

Riddihough, R.P. 1984. Juan de Fuca Plate Map: *JFP-11 Magnetic Anomaly, Open File 85-20*. Pacific Geoscience Centre, Earth Physics Branch, Department of Energy, Mines, and Resources, Sidney, B.C. Canada.

Riddihough, R.P. 1984. Recent Plate Motions. *JFP-9, Open file 83-6*, Pacific Geoscience Centre, Earth Physics Branch, Sydney, B.C., Canada.

Riddihough, R. 1984. Recent movements of the Juan de Fuca plate system. *J. Geophys. Res.*, 89:6980-6994.

Rogers, G.C.. 1979. Earthquake Fault Plane Solutions Near Vancouver Island. *Can. J. Earth Sci.*, 16:523-531.

Sagan, C. 1995. Demon Haunted World: Science as a Candle in the Dark. New York, New York. Random House Publishers.

Schreiner, A.E., C.G. Fox, and R.P. Dziak. 1995. Spectra and Magnitudes of T-waves from the 1993 Earthquake Swarm on the Juan de Fuca Ridge. *Geophys. Res. Lett.*, 22:139-142.

Sibson, R.H. 1986. Earthquakes and Rock Deformation in Crustal Fault Zones *Annual Review of Earth and Planetary Sciences*, 14:149-175.

Silver, E.A. 1971. Tectonics of the Mendocino Triple Junction. *Geol. Soc. Am. Bull.*, 82:2965-2978.

Stoddard, P.R. 1987. A kinematic model for the evolution of the Gorda plate. *J. Geophys. Res.*, 92:11524-11532.

Talandier, J. and E.A. Okal. 1996. Monochromatic T-waves from Underwater Volcanoes in the Pacific Ocean: Ringing Witnesses to Degassing Processes? *Bull. Seism. Soc. Am.*, in press.

Tappert, F.D. and A.A. Hardin. 1977. The Parabolic Approximation Method. In *Wave Propagation and Underwater Acoustics*, J.B. Keller and J.S. Papadakis eds., Lecture Notes in Physics, Springer-Verlag, Heidelberg, 70, 224pp.

Thatcher, W., and T.C. Hanks. 1973. Source parameters of southern California earthquakes. *J. Geophys. Res.*, 78:8547-8576.

Thompson, G. and W.G. Melson. 1972. The Petrology of Oceanic Crust Across Fracture Zones in the Atlantic Ocean: Evidence for a New Kind of Seafloor Spreading. *J. Geol.*, 80:526-538.

Tobin, D.G. and L.R. Sykes. 1968. Seismicity and Tectonics of the Northeast Pacific Ocean. *J. Geophys. Res.*, 73:3821-3845.

Tolstoy, I., and M. Ewing (1950). The T-phase of shallow-focus earthquakes. *Bull. Seism. Soc. Am.*, 40:25-51.

Tréhú, A.M., I. Asudeh, T.M. Brocher, J. Luetgert, W.D. Mooney, J.L. Nabelek, and Y. Nakamura. 1994. Crustal Structure of the Cascadia Forearc. *Science*, 266:237-243.

Velasco, A.A., C.J. Ammon, T. Lay. 1994. Recent Large Earthquakes near Cape Mendocino and in the Gorda plate: Broadband Source Time Functions, Fault Orientations, and Rupture Complexities. *J. Geophys. Res.*, 99:711-728.

Wadati, K. and W. Inouye. 1953. On the T-phase of Seismic waves observed in Japan. *Proc. Japan Acad.*, 29, 47-54.

Walker, D.A., C.S. McCreery, and Y. Hiyoshi. 1992. T-phase Spectra, Seismic Moments, and Tsunamigenesis. *Bull. Seism. Soc. Am.*, 82:1275-1305.

Walter, S.R. 1986. Intermediate-Focus Earthquaks Associated with Gorda Plate Subduction in Northern California. *Bull Seism. Soc. Am.*, 76:583-588.

Wang, K., T. Mulder, G.C. Rogers, R.D. Hyndman. 1995. Case for Very Low Coupling Stress on the Cascadia Subduction Fault. *J. Geophys. Res.*, 100:12907-12918.

Wang, K., J. He, and E. E. Davis. 1997. Transform Push, Oblique Subduction Resistance, and Intraplate Stress of the Juan de Fuca Plate. *J. Geophys. Res.*, 102:661-674.

Wilde, P, T.E. Chase, M.L. Holmes, W.R. Normark, J.A. Thomas, D.S. McCulloch, and L.D. Kulm. 1978. Oceanographic Data off Northern California-Southern Oregon 40° to 43° North Including the Gorda Deep Sea Fan. Lawrence Berkeley Laboratory, Pub. 251, University of California, Berkeley.

Wilson, D.S., R.N. Hey, and C. Nishimura. 1984. Propagation as a Mechanism of Reorientation of the Juan de Fuca Ridge. *J. Geophys. Res.*, 89:9215-9225.

Wilson, D. 1986. A Kinematic Model for the Gorda Deformation Zone as a Diffuse Southern Boundary of the Juan De Fuca Plate. *J. Geophys. Res.*, 91:10259-10269.

Wilson, D. 1989. Deformation of the So-Called Gorda Plate. *J. Geophys. Res.*, 94:3065-3075.

Wilson, D.S. 1993. Confidence Intervals for Motion and Deformation of the Juan de Fuca Plate. *J. Geophys. Res.*, 98:16053-16071.

Yeats, R.S., K Sieh, and C.R. Allen. 1996. *The Geology of Earthquakes.* Oxford University Press, 503pp.